

IDENTIFIED PARTICLE CORRELATIONS AT
INTERMEDIATE TRANSVERSE MOMENTUM IN
RELATIVISTIC HEAVY ION COLLISIONS

By
Ying Guo

SUBMITTED IN PARTIAL FULFILLMENT OF THE
REQUIREMENTS FOR THE DEGREE OF
DOCTOR OF PHILOSOPHY
AT
WAYNE STATE UNIVERSITY
666 WEST HANCOCK DETROIT, 48201
MAY, 2005

© Copyright by Ying Guo , 2005

WAYNE STATE UNIVERSITY
DEPARTMENT OF
DEPARTMENT OF PHYSICS AND ASTRONOMY

The undersigned hereby certify that they have read and recommend to the Faculty of Graduate Student for acceptance a thesis entitled “**Identified particle correlations at intermediate transverse momentum in relativistic heavy ion collisions**” by **Ying Guo** in partial fulfillment of the requirements for the degree of **Doctor of Philosophy** .

Dated: May, 2005

Supervisor:

Prof. Rene Bellwied

Readers:

Prof. Sean Gavin

Prof. Claude Pruneau

Prof. Xiaoyan Han

WAYNE STATE UNIVERSITY

Date: **May, 2005**

Author: **Ying Guo**

Title: **Identified particle correlations at intermediate
transverse momentum in relativistic heavy ion
collisions**

Department: **Department of Physics and Astronomy**

Degree: **Ph.D** Convocation: **May** Year: **2005**

Permission is herewith granted to Wayne State University to circulate and to have copied for non-commercial purposes, at its discretion, the above title upon the request of individuals or institutions.

Signature of Author

THE AUTHOR RESERVES OTHER PUBLICATION RIGHTS, AND NEITHER THE THESIS NOR EXTENSIVE EXTRACTS FROM IT MAY BE PRINTED OR OTHERWISE REPRODUCED WITHOUT THE AUTHOR'S WRITTEN PERMISSION.

THE AUTHOR ATTESTS THAT PERMISSION HAS BEEN OBTAINED FOR THE USE OF ANY COPYRIGHTED MATERIAL APPEARING IN THIS THESIS (OTHER THAN BRIEF EXCERPTS REQUIRING ONLY PROPER ACKNOWLEDGEMENT IN SCHOLARLY WRITING) AND THAT ALL SUCH USE IS CLEARLY ACKNOWLEDGED.

To Dear Mom and Dad

Table of Contents

Table of Contents	v
Abstract	viii
Acknowledgements	x
1 Introduction	1
1.1 Atomic Hypothesis	1
1.2 QCD Phase Diagram and QGP	4
1.3 High-energy heavy-ion physics	6
1.4 Rapidity y and Pseudorapidity η	7
1.5 Nucleus-Nucleus Collision	8
1.5.1 Dynamics of nucleus-nucleus collisions	10
1.5.2 Impact parameter and Centrality	10
1.5.3 Bjoken picture	11
1.6 Jet processes as probe of QGP	13
1.6.1 What is a jet	13
1.6.2 Jet fragmentation and Hadronization	14
1.6.3 Jet quenching in the dense medium	15
1.6.4 Nuclear Modification Factor	17
1.7 High p_T particle azimuthal correlations	19
1.8 Identified Jet correlations: Motivation	22
2 The Experiment Set up	26
2.1 Introduction	26
2.2 RHIC	27
2.3 STAR Detector	30
2.4 Zero Degree Calorimeter (ZDC)	32
2.5 Central Trigger Barrel	34

2.6	Beam Beam Counter (BBC)	34
2.7	Time Projection Chamber (TPC)	37
3	Azimuthal Correlations: Introduction	42
3.1	Definition of the Azimuthal Correlations	42
3.2	Components of the azimuthal correlation function	46
3.2.1	pp collisions	46
3.2.2	AuAu collisions	47
3.3	Elliptic flow	47
3.4	Uncorrelated Background of Azimuthal correlations	50
3.5	Elliptic Flow v_2 in two particle azimuthal correlations	53
3.6	Analysis techniques overview	55
3.6.1	Reference Model	56
3.6.2	Conservation of Momentum	57
3.6.3	Difference function	58
4	Data Analysis	60
4.1	Data Set	60
4.1.1	Centrality	61
4.1.2	Statistics	63
4.2	Trigger and associated particle selections	64
4.2.1	Unidentified charged hadrons	64
4.2.2	V_0 reconstructed particles: Λ , $\bar{\Lambda}$, K_0^S	66
4.2.3	Background of misidentified V_0 s	70
4.3	Efficiency Correction	72
4.3.1	Tracking Efficiency	72
4.3.2	TPC sector efficiency correction	74
4.4	Sample of correlation function	75
5	Azimuthal correlations for identified trigger particles	80
5.1	Correlation functions with Λ , $\bar{\Lambda}$ and K_0^S as trigger particles	81
5.2	Associated particle yield for same side and back side	88
5.3	Asymmetry of the correlation – the Difference Function and discussions	94
5.4	$AuAu$ to pp ratio in central collisions	99
6	Back side correlations in central $AuAu$ collisions	107
6.1	Introduction	107
6.2	Back side fit for jet correlations based on momentum balance	108
6.3	Centrality dependence	113

6.4	Components of the back side correlation in central $Au + Au$ collisions.	113
6.5	Discussion	122
7	p_T dependence of correlation	124
7.1	Correlation production mechanism: Fragmentation or Recombination ?	124
7.2	Associate p_T distribution	126
7.3	Trigger p_T distribution	131
7.4	Studies on the systematic uncertainty	135
7.4.1	Uncorrelated background	135
7.4.2	Leading particle bias	136
7.4.3	Elliptic flow	136
7.4.4	Systematics in yield retrieval	138
7.5	Discussions	138
8	Summary	142
A	j_T and k_T related to jet correlation	145
B	Momentum conservation in azimuthal correlations	148
C	Correlation production from shower parton recombination model	151
	Bibliography	156

Abstract

High p_T particle correlations have been applied successfully in studying jet phenomena in nuclei-nuclei collisions at relativistic energy. They provide us information about not only the features of the fragmentation process itself but also its medium modification effects such as jet quenching, which is considered one of the signature of formation of a QGP¹. Identified particle high p_T correlations allow us to gain detailed flavor dependent information about the particle production mechanism and medium effects related to jets. Such information is essential for us to understand the basic principle of strong interaction and the properties of with partonic collecte matter.

In this work, we present correlations between strange baryons ($\Lambda, \bar{\Lambda}$) and mesons (K_0^s) and unidentified charged hadrons at intermediate p_T in $AuAu$ collisions at 200 GeV/c . We have studied the centrality dependence and the p_T dependence of the correlation for different trigger particle species. It has been found that for central Au+Au collisions, the large width of the back side correlations indicates a collapse of the jet structure. This is consistent with previous measurement of suppression of the back side correlation for unidentified charged hadrons at high p_T . However, the same side correlations show large AA/pp ratios in central $AuAu$ collisions. This effect together with the trigger p_T dependence of the correlation, can not be explained by a simple jet quenching picture. The correlation yield and its scaling clearly suggests additional hadron production mechanism at intermediate p_T . One explanation which has been proposed by Rudy Hwa and C.B. Yang et. al. is the shower parton recombination model. By allowing a shower parton to recombine with thermal partons the model

¹Quark Gluon Plasma

predicts the large AA/pp ratio in the intermediate p_T . The model calculation of the AA/pp ratio as a function of the associated particle p_T is general in agreement with our measurement in magnitude and its centralities dependence except in the high p_T range where the model calculation saturates higher values than our measurements. This deviation might indicate the decoupling of the jet fragmentation from the thermal source.

Our measurements also show finite dependence on trigger particle species. In central $AuAu$ collisions the trigger p_T dependence indicate different trends for different trigger particle species. Such effects are not seen in dAu . One of the possibility is that in central $AuAu$ collisions, the medium works as an amplifier for jet fragmentation. Subtle differences in fragmentation in dAu could be much larger in $AuAu$ due to such an amplification effect. Additional effects such as finite baryon densities, gluon quark jet differences and flavor dependence of the recombination effect could also make a contribution. To discriminate between these effects requires more statistics and theoretical guideline.

In addition to the results, we are also presenting analysis methods (some are new) for the jet-like correlation analysis. Hopefully they will be a as the reference for future related studies.

Acknowledgements

I would like to thank Rene Bellwied, my supervisor, for his many suggestions and constant support during this research. I am also thankful to Sergei Voloshin for his guidance through the early days of confusion.

Professor Sean Gavin and professor Claude Pruneau have always been patience with my unexpected questions and countless requirements for accessing the coffee machine.

I would also like to thank the heavy ion nuclear physics group and the STAR collaboration for allowing me to work on this project. It has been a wonderful experience for me.

Finally, I wish to thank the following: Houbei (for love and care); Hamede, Saugy and Sara (for friendship and discussions and supplies of cigarettes); Alexei Palivnov (for help on Pythia) and Alex Stopolsky and Eve (for help on Latex)

Detroit, Michigan
May, 1st , 2005

Ying Guo

Chapter 1

Introduction

1.1 Atomic Hypothesis

The ancient Chinese believed that the world is made of five basic elements: Metal, Wood, Water, Fire and Earth. The laws that govern them is the called "Yi-Jing" (500 B.C.)¹ which is the law of "Yin and Yang".

It is thought that combination of the elements and the interactions of "Yin" and "Yang" "describe" the whole world. Ancient Chinese people have already tried to classify the infinitely mysterious world by using a small group of elements and their interactions. There are a few underlying properties for these elements: such as uniqueness, completeness, no substructure. On the other side of the earth, about the same time, Greek philosopher Democritus (460-371 B.C.) formulated the atomic hypothesis: All matter consists of the smallest (indivisible) entities (atoms), separated by empty space. Combinations of the different kinds of atoms form all the things in

¹YI JING, also known as The Book of Changes, is one of the Five Classics of Confucianism. The book's influence on Chinese minds and its universal popularity are due to a system of cosmology that involves humans and nature in a single system. Yi Jing presents 64 symbolic hexagrams that, if all right understood and well interpreted, are said to contain profound meanings that humans may apply to daily life. The book is taken as a means of understanding, and adjusting and maybe reach control over future events.

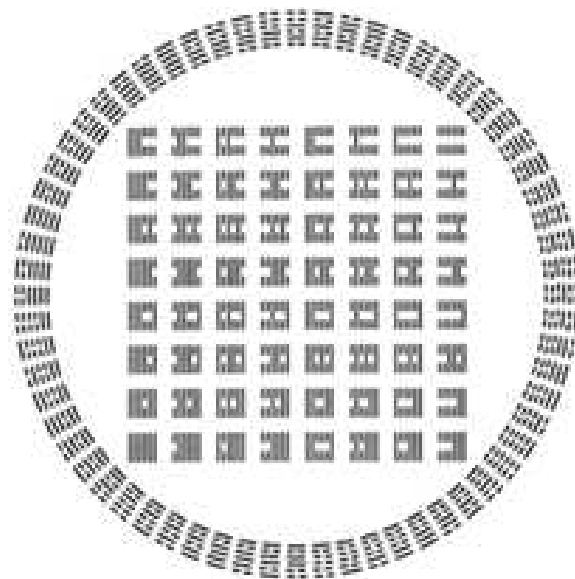
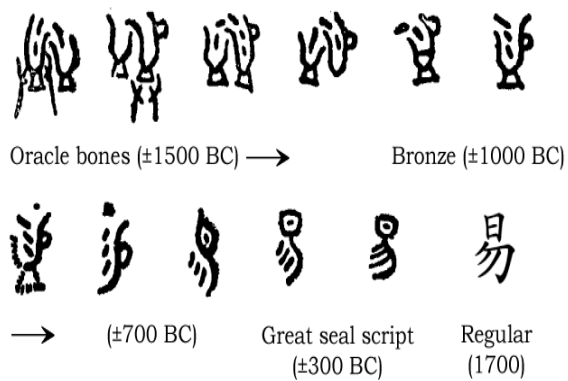


Figure 1.1: Diagram of combination of "Yin" and "Yang"



© Harmen Mesker

Figure 1.2: Evolution of the Chinese character "Yi" (means change.)

nature. It is interesting to know that the ancient Greek were more interested on the concept of the atom while the ancient Chinese also cared about the interaction.

The modern scientific approach originated in a surprisingly similar manner — it classifies the world by using the combination of elementary particles and their interaction. The Atomic Hypothesis was quoted by Feynman as one of the most important knowledge of physics in our time. The search of the ultimate "Atom" particles and their interactions has been the major goal of high energy and elementary particle physics. Many results from different experiments show that majority of the universe² visible is made of elementary particles called quarks (see Appendix A for general information about the Standard Model). The interactions between quarks (strong interaction) can be described by QCD³. Abundant results from variety of experiments have shown that QCD seems to be the "correct" theory for strong interaction. It gives us a theoretical handle to describe different kinds of states of matter even for extreme conditions. Among the many phenomena of the strong interaction the following two are the most striking or in some sense even bizarre:

Quark Confinement

Although the quark model describes the vast experimental results for thousands of hadrons, all attempts of isolating a single free quark have failed. The quarks are confined therefore can exist only as color neutral objects i.e. baryons or mesons. Apparently the color force does not drop off with distance like the other forces. It is postulated that it may actually increase with distance at the rate about 1 GeV/fm. A free quark is not observed because by the time the separation is on an observable

²Recent cosmology study shows that majority of the universe are made of dark energy and dark matter

³Quantum Chromo Dynamics.

scale, the energy is far above the pair production energy for quark-anti-quark pairs. One kind of the visualization of the confinement is called the "bag model". Quarks are contained in an elastic bag which allows them to move freely around within the bag. However as long as you try to pull a quark out, the bag stretches and resists.

Asymptotic Freedom

However, under the conditions of high energy experiment the behaviors of the quarks shows that they do not seem to interact at all, in other words they are almost free (parton model)⁴

QCD has successfully solved the apparent conflict of long range confinement and the short range asymptotic freedom. The later one is understood and can be described by the concept of pQCD⁵ in processes which have large momentum transfer. pQCD has been successful in explaining high energy experiment measurements with surprising accuracy. The confinement is within the non pQCD regime where analytical calculations are not practical. However, numeric method such as Lattice QCD can be applied to this regime.

1.2 QCD Phase Diagram and QGP

Lattice QCD calculations, considering of two or more quark flavors, predict a phase transition from a confined phase such as hadronic matter, to a deconfined partonic matter phase, such as the quark gluon plasma (QGP), at high energy density(1 GeV fm^{-3}) and high temperature (150 MeV)[1] [2]. Figure 1.3 shows the phase

⁴Parton model was first introduced by Feynman and Bjorken in late 60s to address the new data on deep inelastic scattering experiments between electrons and nucleons. It views nucleons as made up of point-like constituents and provides a framework for calculating scattering cross sections and nuclear structure function for nucleons.

⁵Perturbative Quantum Chromo Dynamics

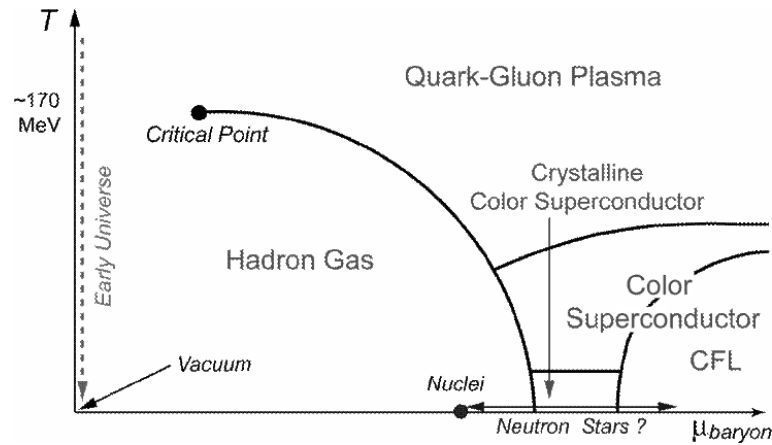


Figure 1.3: Phase Diagram of Quark Matter. The dashed line shows the path of the evolution of the Universe.

diagram of quark matter . As we can see at higher chemical potential (μ) or higher temperature, ordinary hadronic matter can transfer into defined partonic states such as QGP.

It is thought that at the very early stage of our universe, about 10^{-6} seconds after the Big Bang, our universe once existed in the form of QGP. It is also believed that the cores of the neutron stars exist also in the form of partonic matter due to their extremely high baryon densities. However, to create and measure QGP in the laboratory is extremely difficult since it requires both high energy density and high temperature which is Millions of times larger than the present day temperature. Such challenges have not stopped curious experimental physicists from trying. As I will show in the following section, scientists are trying to use collisions of heavy nuclei to create a sizable hot medium which could transition into a QGP.

1.3 High-energy heavy-ion physics

In order to create a QGP, lots of energy need to be deposited into a very small volume in a very short amount of time. This can be achieved by the relativistic heavy ion nuclear collisions. Because of the significant large inelastic nucleon cross section, a large portion of the initial energy can get deposited into the center-of-mass system within a short duration of time (before the energy can radiate out and escape the system). Collider accelerators such as RHIC ⁶ can accelerate particles up to 200 GeV/c per nucleon. So the total energy deposit into the system is on the order of tens of TeV . The energy density in the center of mass can reach GeV/fm^3 level. To create and measure the QGP has been one of the most important objective of high-energy heavy-ion experiment. On theoretical side, as emphasized by T.D.Lee and many other theoretical physicists, such experiments will help us understand the puzzle of the confined quarks, and how the Chiral symmetry is broken for hadrons and how to understand partonic interactions. Since this is a new field, methods and techniques are still under development, which makes it more difficult to determine the existence of a QGP even when it is created. Probes based on different models have been suggested to test the existence of a QGP. Jet quenching is among one of the signatures of the formation of QGP [3] [4] [5]. Energetic partons produce hadrons through jet fragmentation. Such processes have been studied extensively in high-energy elementary particle experiments. In the presence of a dense medium such as QGP where the gluon density will be higher, a jet is expected to suffer significant energy loss and therefore be quenched. Such a phenomenon can be used to prove the existence of the dense matter. Measurable quantities related to the suppression

⁶Relativistic Heavy Ion Collider

of the jet or high p_T particles including the nuclear modification factor R_{AA} (AA to pp), R_{CP} (central to peripheral), particle ratios, correlations etc. Before we describe the details, I will outline some basic terminologies of these field.

1.4 Rapidity y and Pseudorapidity η

One of the commonly used kinematic condition of a particle is the rapidity variable y . The rapidity of a particle is defined in terms of its energy-momentum components p_0 and p_z by

$$y = \frac{1}{2} \ln \left(\frac{p_0 + p_z}{p_0 - p_z} \right) \quad (1.4.1)$$

y is a dimensionless quantity related to the ratio of the forward light cone momentum to the backward light cone momentum. One can easily derived from the definition that for a particle traveling with velocity of β in positive z direction we have,

$$y_\beta = \frac{1}{2} \ln \left(\frac{1 + \beta}{1 - \beta} \right); \quad y_\beta = \beta + O(\beta^2) \quad (1.4.2)$$

Note that this is independent of the mass of the particle. Under *Lorentz transformation* from the laboratory frame F to a new coordinate frame F' moving with a velocity β in the z -direction, the rapidity y' of the particles in the new frame F' is related to the rapidity y in the old frame F by,

$$y' = y - y_\beta \quad \text{where :} \quad y_\beta = \frac{1}{2} \ln \left(\frac{1 + \beta}{1 - \beta} \right) \quad (1.4.3)$$

As we can see y is not perfectly Lorentz invariant but it rather shifts with a constant from frame to frame. To measure the rapidity of a particle, it is necessary to measure two quantities of the particle, such as energy and longitudinal momentum. In many experiments, it is only possible to measure the angle of the detected particle relative

to the beam axis. In that case, it is convenient to utilize this information by using the *pseudorapidity variable* η to characterize the detected particle. The definition of η is the following:

$$\eta = \frac{1}{2} \ln \left(\frac{|\mathbf{p}| + p_z}{|\mathbf{p}| - p_z} \right) \quad (1.4.4)$$

or,

$$\eta = -\ln [\tan(\theta/2)] \quad (1.4.5)$$

where θ is the angle between the particle momentum \mathbf{p} and the beam axis. We can express the rapidity y in terms of η or vice versa as following.

$$y = -\frac{1}{2} \ln \left[\frac{\sqrt{p_T^2 \cosh^2 \eta + m^2} + p_T \sinh \eta}{\sqrt{p_T^2 \cosh^2 \eta + m^2} - p_T \sinh \eta} \right] \quad (1.4.6)$$

$$\eta = -\frac{1}{2} \ln \left[\frac{\sqrt{m_T^2 \cosh^2 y - m^2} + m_T \sinh y}{\sqrt{m_T^2 \cosh^2 y - m^2} - m_T \sinh y} \right] \quad (1.4.7)$$

from which one can also obtain the relation between $dN/dydp_T$ and $dN/d\eta dp_T$ as

$$\frac{dN}{d\eta dp_T} = \sqrt{1 - \frac{m^2}{m_T^2 \cosh^2 y}} \frac{dN}{dy dp_T} \quad (1.4.8)$$

⁷ In experiments at high energies, dN/dy has a plateau shape around $y = 0$. The $dN/d\eta$ follows a similar shape with a small dip around $\eta \approx 0$.

1.5 Nucleus-Nucleus Collision

To describe the dynamics of the nucleus-nucleus collision process, it is useful to consider the collision at the baryon level. After an incident projectile nucleon suffers a collision, the resultant energetic baryon-like object can be treated loosely as the

⁷At higher enough transverse momentum, rapidity and pseudorapidity are roughly equal.

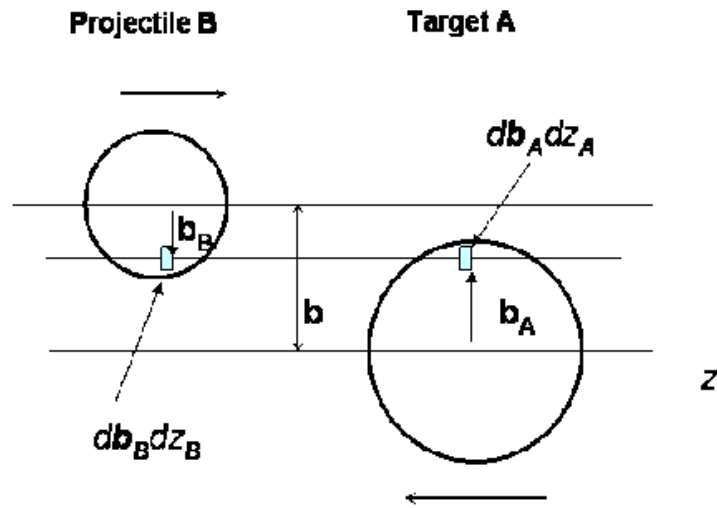


Figure 1.4: The collision of the projectile nucleus B with the target nucleus A at an impact parameter b

projectile object which continue to make further collisions along the direction of the projectile. The Glauber model [6] of multiple-collision processes provides a quantitative picture of the geometrical configuration of the nuclei when they collide. It is based on the concept of a mean-free path with the assumption of an elementary baryon-baryon cross section. The model is useful to describe the pure geometrical effects in a nucleus-nucleus collision due to the impact parameter b (see Figure 1.4). Such considerations are essential when measurements need to be compared to corresponding pp collisions.

1.5.1 Dynamics of nucleus-nucleus collisions

In nucleus-nucleus collisions, the nucleons that participate in the collision are called **participants** where all other nucleons are called **spectators**[6]. Simply from the geometry configuration one can estimate the number of participants for a given impact parameter. It is useful to introduce the thickness function $T_A(b_A)$ which is defined as:

$$T_A(b_A) = \int \rho_A(b_A, z_A) dz_A. \quad (1.5.1)$$

For nuclei A, ρ_A represents the density of the nucleons, which is a function of the transverse radius b_A and longitudinal coordinate z_A (see in Figure 1.4).

The probability of having n inelastic collisions at impact parameter \mathbf{b} can be described as :

$$P(n, \mathbf{b}) = \binom{AB}{n} [T(b)\sigma_{in}]^n [1 - T(b)\sigma_{in}]^{AB-n}, \quad (1.5.2)$$

where $T(b)$ is the convolution of the thickness function of the projectiles and the target with the inelastic baryon-baryon collision thickness function $t(b)$.

$$T(b) = \int d\mathbf{b}_A d\mathbf{b}_B T_A(\mathbf{b}_A) T_B(\mathbf{b}_B) t(\mathbf{b} - \mathbf{b}_A - \mathbf{b}_B) \quad (1.5.3)$$

1.5.2 Impact parameter and Centrality

From equation [1.5.2] one can derive the number of participants and number of collisions for a given impact parameter. However in nucleus-nucleus collisions, we can not directly measure the impact parameter. We know that the multiplicity of particles is related to the number of participants in the collision. The total cross section as function of the event multiplicity has a "horse back" shape distribution as shown in Figure. 1.5. Hence, we can define the centrality of the collision by the multiplicity of

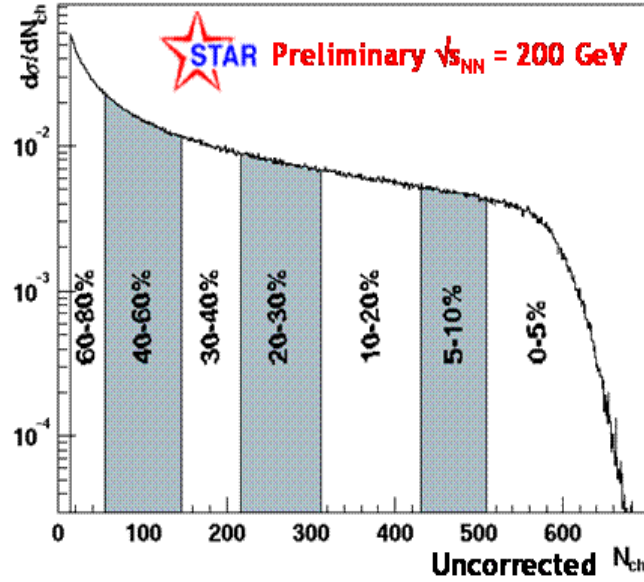


Figure 1.5: Centrality definition based on N_{ch} distribution in the central plateau

the event. As shown in the figure, the most central collisions are defined as the top 5 percent of the total cross section, i.e. thus have the largest event multiplicity. This method have been tested and agrees well with simulation [7].

1.5.3 Bjoken picture

After the nucleus-nucleus collision the system evolves as a function of proper time ⁸. Figure. 1.6 shows the space-time diagram according to the Bjoken model using the longitudinal coordinate z and the time coordinate t . The two incoming beams are shown as straight lines. The nuclei collide at $z = 0$ and $t = 0$. At a time interval around τ_0 the QGP is formed. After expansion and cooling the system will finally

⁸Proper time is the physical time in an inertial reference frame in which both events are simultaneous. The best thing about the proper time is that it is Lorentz invariant. In the space-time coordinates (t, x, y, z) it is often defined in a differential form as $:d\tau^2 = dt^2 - \frac{1}{c^2}(dx^2 + dy^2 + dz^2)$

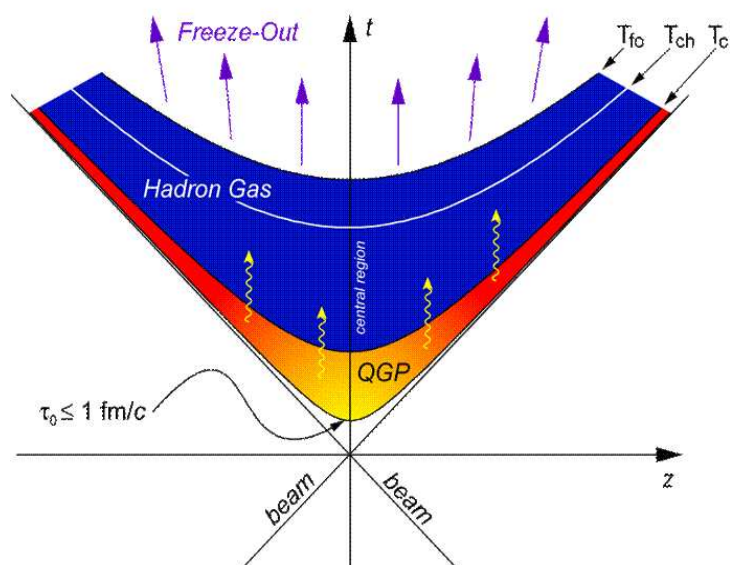


Figure 1.6: The evolution of the "fireball" of heavy ion collision. QGP is assumed to formed shortly after the collision roughly at time scale of $\tau_0 \sim 1 \text{ fm}/c$

freeze out into hadrons. Since we can only detect the final products of the collisions, namely the particles after the freeze out, most of the information about the early stage of the collision such as the QGP properties and hadronization has been washed out by final state interactions. Yet still we can carefully choose certain probes which retain the information about the early stage of the collision. In the next section we will discuss how to use jet processes as the probes to detect the properties of the medium.

1.6 Jet processes as probe of QGP

1.6.1 What is a jet

In deep inelastic scattering experiments, for certain events a cluster(cluster) of co-moving particles have been found emerging from the collision vertex. They are all traveling in roughly the same direction and carrying significant amount of energy. Physicists use jet(s) to represent these energetic hadron cluster(s). Hadrons within the jet form a jet cone. Since they are all produced by the fragments of the initial energetic parton they all share the same prefer direction (the jet axis). It has also been found that for each jet there is a leading particle which carries large fraction of the jet energy. When physicists discovered jet, they also found di-jets ⁹which representing back-to-back fragmentation of a $q\bar{q}$ (or $q\bar{q}$) pair. Hadronic jets are striking high energy phenomena which strongly support the constituent quark picture. The studies of the properties of jets can test our knowledge about strong interaction and also extracting new physics. Figure 1.7 represent the di-jet in pp collisions, where θ represents the

⁹Tri-jets were also found at about the same time which confirmed the existence of di-jets/jets by excluding the scenario of the conservation of momentum.

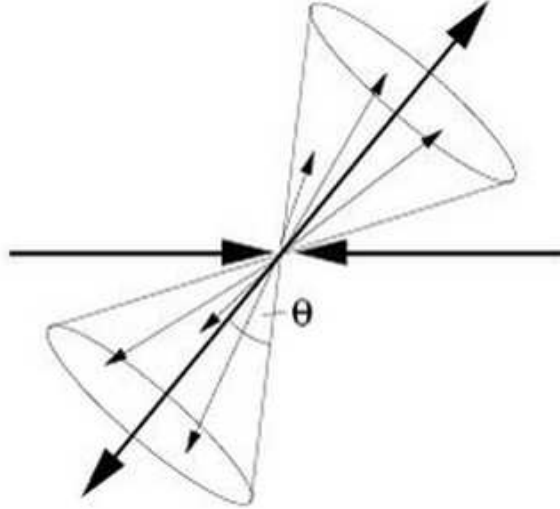


Figure 1.7: Di-jet in pp collisions. θ represents the angle of the jet cone

angular size of the jet cone.

1.6.2 Jet fragmentation and Hadronization

In QCD hard scattering processes $A + B \rightarrow C + D + X$ can generally be treated through factorization of the measured parton-parton cross section shown in Equation 1.6.1.

$$\frac{d\sigma}{dy} = \sum_{a,b} \int_0^1 \int_0^1 \int_0^1 f_{a/A}(x_a) f_{b/B}(x_b) \frac{D_{C/c}(z_c)}{z_c} \frac{d\sigma_{ab \rightarrow cd}}{dy} dx_a dx_b dz_c \quad (1.6.1)$$

In Equation 1.6.1 $f_{a/A}(x_a)$ and $f_{b/B}(x_b)$ represent the parton distribution functions (PDF), which are the probabilities of finding a parton with x ¹⁰ inside the initial hadron. $\frac{d\sigma_{ab \rightarrow cd}}{dy}$ gives the cross section of initial partons (a and b) to produce

¹⁰ $x_{Bjorken} \equiv \frac{p_{parton}}{p_{hadron}}$

outgoing partons (c and d) which fragments into jets of hadrons. $D_{C/c}(z_c)$ represents the fragmentation function. The fragmentation functions can not be calculated by using pQCD. However, from its s-dependence, it can be parameterized at one fixed scale s_0 and then predicted at other scales¹¹. Fragmentation function explains the momentum scaling of the hadrons at the final states. It does not explain the formation of hadrons, for which one must so far resort to models. Among which I will try to describe briefly the basic ideas of the cluster model [10] and the string model. **Cluster model**¹² This model starts by splitting gluons non-perturbatively into $q\bar{q}$ pairs after the parton shower. The color singlet $q\bar{q}$ are assumed to form clusters. Then these clusters will isotropic decay into pairs of hadrons according to the densities of states of the quantum number. **String model**¹³ This model is based on the dynamics of a relativistic string, which represents the color flux tube between the initial $q\bar{q}$ pair. The string breaks up into hadrons via the $q\bar{q}$ pairs productions in its intense color field. Figure 1.8 illustrates the difference between the cluster model and the string model.

1.6.3 Jet quenching in the dense medium

In the presence of dense medium, it is expected that both fragmentation and hadronization would be modified. Based on QCD calculations partons will lose energy through gluon radiation, very similar to *Bremsstrahlung* radiation for charged particles traveling through electromagnetic fields. The estimated energy loss is proportional to the gluon density of the medium show in equation 1.6.3.

¹¹Scaling of the fragmentation function is described by DGLAP equation. See references [8][9] for details

¹²used by Event Generator **HERWIG**

¹³used by Event Generator **JETSET**

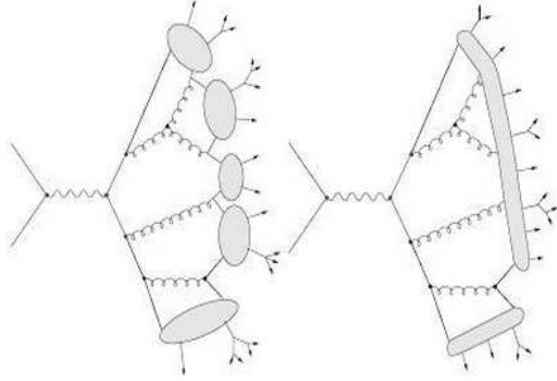


Figure 1.8: Cluster and String hadronization models

$$\Delta E \approx \frac{C_R \alpha_s}{4} \hat{q} \mathbf{L}^2 \quad (1.6.2)$$

$$\hat{q} = \frac{\langle k_T \rangle_{medium}}{\lambda} \sim \alpha_s \rho_{glue} \quad (1.6.3)$$

Another calculation based on the opacity expansion of the medium also shows strong dependence on the gluon density.

$$\Delta E = \pi C_A C_a \alpha_s^3 \int d\tau \rho_{glue}(\tau, r(\tau)) \tau \ln \left(\frac{2E_{jet}}{\mu L^2} \right) \quad (1.6.4)$$

In the presence of dense medium such as a QGP, partons will suffer several times the energy loss than in ordinary cold nuclear matter. Since the QGP only exists at the early stage of the collisions only high p_T jet particles created by hard scattering can experience such an effect. Therefore jet processes can be used as the probes to test the formation of a QGP. Jet quenching is one of the signature of the formation of QGP [11] [5]. In addition, jet properties and hadronization are also expected to be modified by the medium[12][13]. Studying the medium modification effects will

provide us additional information therefore help us gain more understanding about the fragmentation and hadronization processes.

1.6.4 Nuclear Modification Factor

In the presence of dense partonic medium, energetic parton will lose a significant amount of energy and therefore being quenched. One method to measure such an effect is to measure the Nuclear Modification Factor R_{AA} . 1.6.5 shows the definition of R_{AA} . It is the ratio of spectra measured in Au+Au collisions to pp collisions. T_{AA} is the scaling factor based on certain nucleus-nucleus collision model¹⁴. Figure. 1.9 shows the measurement of R_{AA} for unidentified charged hadrons in $AuAu$ collisions at STAR¹⁵. It is obvious that in the high p_T range of a large suppression of charged hadrons occurs in central $AuAu$ collisions [14]. Such an effect can be explained as the result of the jet quenching. It should be noted that the magnitude of R_{AA} also depends on the scaling factor T_{AA} which is only an approximation.

$$R_{AA} = \frac{d^2N/dp_T d\eta(AuAu)}{T_{AA} d^2\sigma/dp_T d\eta(pp)} \quad (1.6.5)$$

The significant difference in R_{AA} between the central and peripheral Au+Au collisions is understood as the medium effect, i.e. in central collisions high p_T particles are experienced significant energy loss inside the medium which leads to the suppression of R_{AA} at higher p_T . This was predicted [3][15] to be one of signature of the QGP formation. The peripheral R_{AA} is in agreement with the pp measurement which indicates that strong medium effects are only taking place in central collisions.

¹⁴Two common scaling are binary scaling and participant scaling, which are based on binary collisions model and wounded nuclear collision model, respectively

¹⁵the Solenoidal Tracker at RHIC

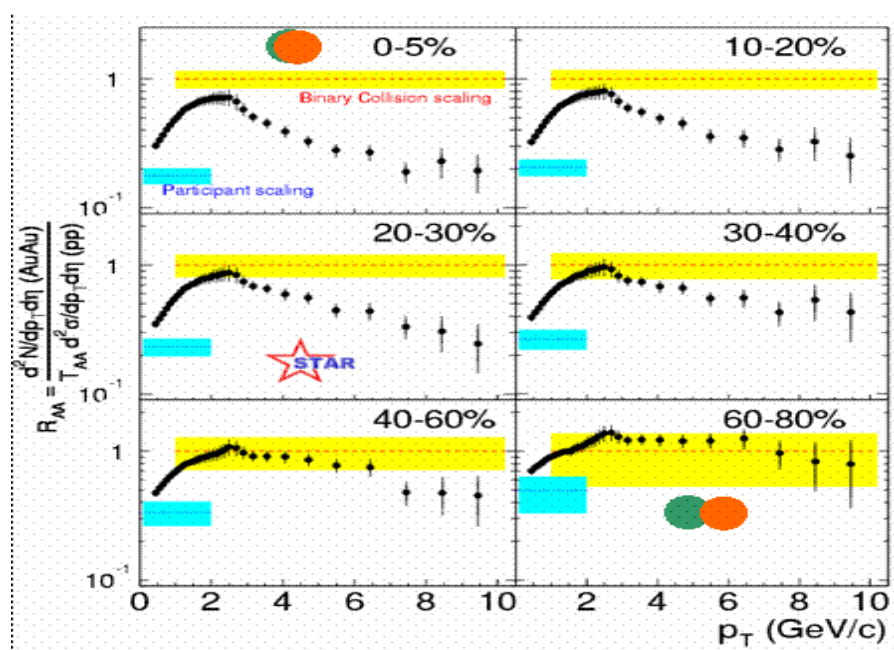


Figure 1.9: Centrality dependence of R_{AA} for charged hadrons in AuAu collisions.

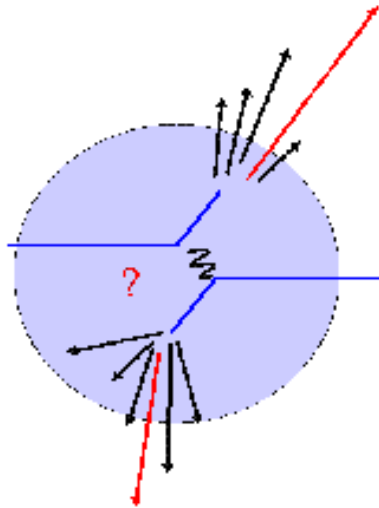


Figure 1.10: Jets produced from hard scattering

Measurements of R_{AA} of identified particles show similar quenching effects for central collisions [16]. Although the nature of the detailed structure of R_{AA} is not fully understood, it is generally accepted that the suppression is due to the result of Jet quenching. In the next section we will try to give an introduction about how to measure such effects by using azimuthal correlations of high p_T particles.

1.7 High p_T particle azimuthal correlations

Jets and di-Jets are created by hard scattering partons during the early stage of the collisions. Figure 1.10 shows a cartoon of a hard scattering process with the presence of a medium. The scattered partons will fragment into many co-moving hadrons via the processes of jet fragmentation. Ideally due to momentum conservation the total transverse momentum of all produced hadrons in the center of mass should be equal

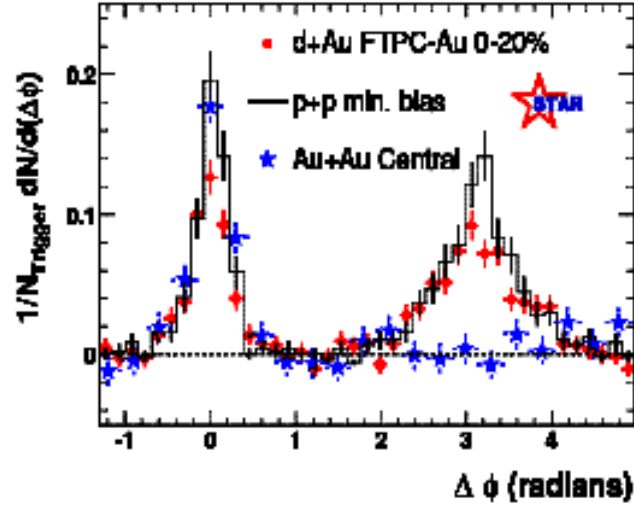


Figure 1.11: Jet azimuthal correlations in Au+Au, dAu and pp

to zero. If we formed a di-hadron correlation function in $\Delta\phi$ we expect a peak at zero which represents the same side correlations (correlations within the same jet cone) and another peak at π which represents the away side correlations (correlation between two different jet cones). Detail description about the azimuthal correlations will be covered in chapter 3.

In central Au+Au collisions, it has been found that the away side of the correlations have been totally quenched, [17][18].

as shown in Figure 1.11 and 1.12, where for d+Au and pp there exist large away side correlations. These measurements indicate that the medium created in central Au+Au collisions causes a strong suppression effect on the away side correlation. The suppression of away side correlations is simply due to the fact that particles emitted on the away sides always need to travel a longer distance through the medium compared to the same side particles. Such a geometry effect is confirmed by measuring

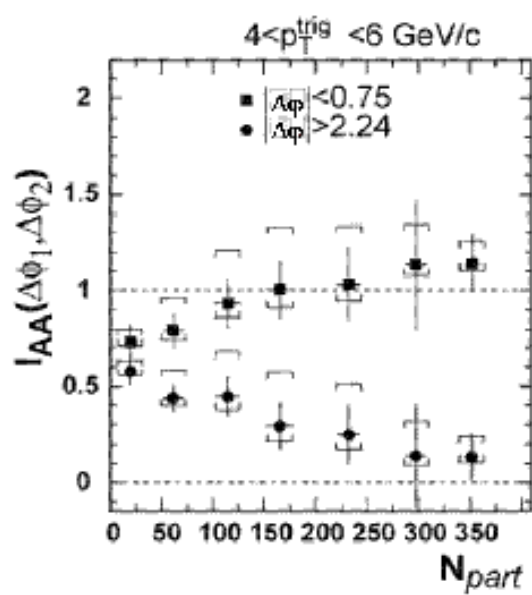


Figure 1.12: Centrality dependence of the Jet Correlations. I_{AA} is the ratio of the correlated associated particle yield between Au+Au and p+p.(See Equation)

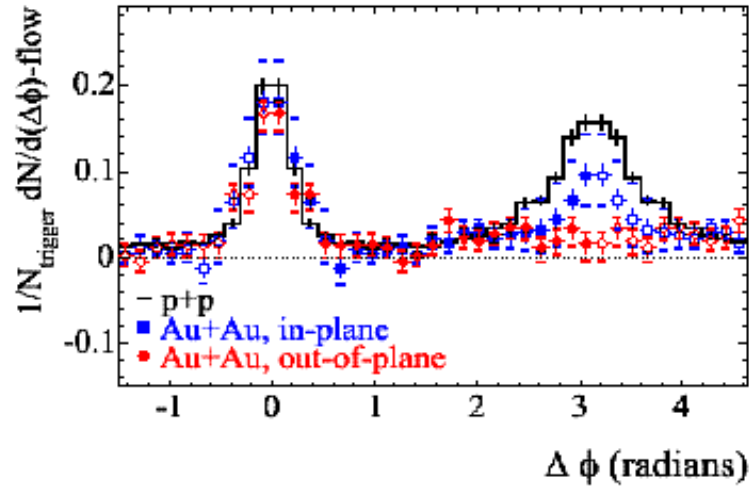


Figure 1.13: Jets correlations with respect to the reaction plane

the difference in suppression between particles close to the reaction plane (in plane) and perpendicular to the reaction plane[19] (out of plane). As shown in 1.13 due to the initial geometry of the system (almond shaped), particles traveling perpendicular to the reaction plane traverse a longer distance than particles closed to the reaction plane. Therefore they experience more suppression. All these measurements have shown that due to the strong quenching effects of the medium correlation measurements are very sensitive to the initial geometric conditions of the systems.

1.8 Identified Jet correlations: Motivation

Particle identified jet correlations can provide us additional information about the jet quenching ,the particle production mechanism and the fundamental properties of the strong interaction in the presence of the medium based on flavor dependence.

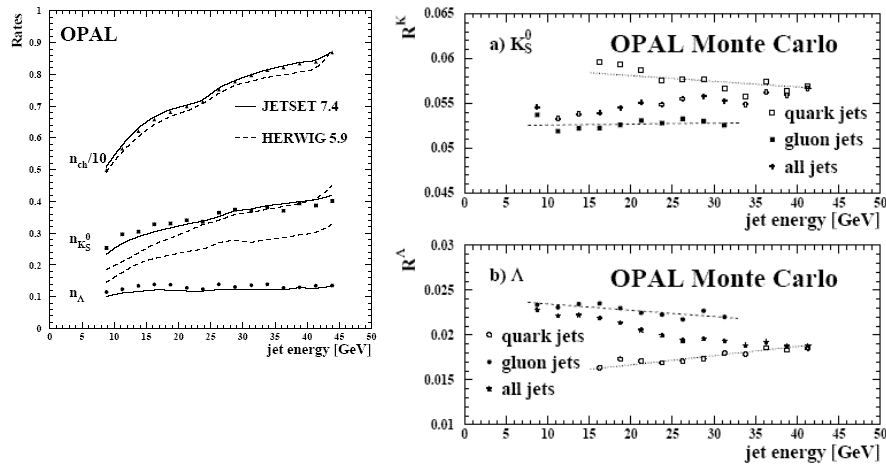


Figure 1.14: Jet Rate as function of jet energy for Λ and k_0^s from gluon jets and quark jets. Energy dependence can be very different for different final state hadrons.

For example, it has been suggested that for a particular final state hadron such as Λ , the contribution to the fragmentation function from different initial partons are very different[?]. Since medium modification can be very different for different type of partons (quark vs gluon, heavy quark vs light quark)[?]more), the final state jet correlations could be affected. Tagging the jet with different trigger particle species gives us the opportunity to study such differences.

Figure 1.14 shows the jet rate as a function of jet energy for Λ and k_0^s from OPAL¹⁶. The energy dependence of the jet rate is quite different for different particles in the final state[20] depending on the initial parton fragmentation. This allows us to use these particles as tags for gluon or quark jets. It has been found that gluon jets and quark jets have quite different fragmentation function. Figure 1.15 shows the measured n_{ch} distribution of quark and gluon jets as the function of \sqrt{s} . The behavior

¹⁶OPAL took its name from the detector description: an Omni-Purpose Apparatus at LEP(Large Electron-Positron collider)

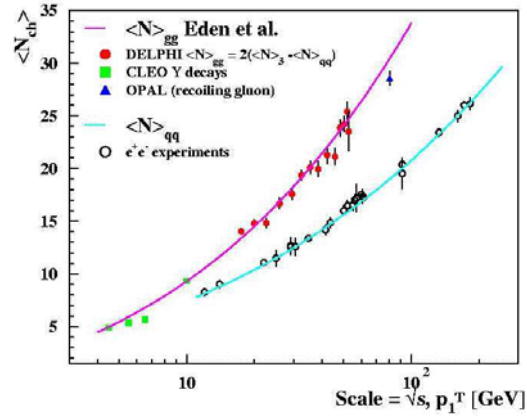


Figure 1.15: N_{ch} distribution of quark and gluon jets as the function of root S. The gluon jet are significantly softer than quark jet however with higher multiplicity.

of quark jet and gluon jet are very different¹⁷. It is believed that these difference are due to the probabilities of gluon splitting, where for gluon the rate is much higher in the soft regime. Identified particle correlation studies may provide a way to study these kinds of partonic level differences especially in the presence of a medium.

Hadronization is among one of the most profound processes whose basic properties is still unclear. Since it can not be described directly by pQCD, the usual treatment is to factorize the non pQCD contributions which are then to be determined by experiments. In a jet fragmentation process, quarks from gluon splitting recombine with each other to form hadrons and all the energy in the created hadron shower are coming from the initial energetic parton. In the presence of a medium, where the thermal parton density might be high, possible interaction between shower partons and thermal partons will significantly modify the final hadron production.

¹⁷The measured difference between quark and gluon fragmenting multiplicities is consistent with 9/4, the color formation factor ratio.

In this thesis, I am presenting correlation studies in the "high" or intermediate p_T range for different particle species including Λ , $\bar{\Lambda}$, k_0^S and charged hadrons. These different particle species will allow us to determine not only the baryon meson differences but also particle anti particle differences and strange particle and non-strange particle differences. Both related physics and analysis techniques will be discussed in details in the later chapters. It is hoped that not only the conclusion drawn from the measurement but also the analysis approach will provide solid bases for future related correlation studies.

After the introduction, the description of the experiment is given in chapter 2. In Chapters 3 and 4 I am explaining the chosen correlations and data analysis techniques. In Chapters 5,6,7 we present the correlation measurements for different trigger particle species. The Centrality dependence study, p_T (both trigger and associated particles) dependence studies will be presented in these chapters. The final chapter draw some conclusions and gives an outlook for future measurements.

Chapter 2

The Experiment Set up

In this chapter I will try to give an introduction to the experiment and the RHIC accelerator facility. I will cover the major detector components and their configuration especially the ones which are related to the data used in this thesis.

2.1 Introduction

The experiments were conducted at BNL ¹. BNL is a federally funded lab with a remarkable history, which includes four Nobel Prize awards in physics. The Relativistic Heavy Ion physics program at BNL was initiated in 1998. RHIC² is a multi-purpose colliding beam facility which can conduct experiments with both, ultra relativistic heavy ions and polarized protons. There are four dedicated detectors at

¹Brookhaven National Lab

²Relativistic Heavy Ion Collider

	AGS	AGS	SPS	SPS	SPS	RHIC	RHIC	LHC
Start Year	1986	1992	1986	1994	1999	2000	2001	2006
A_{max}	^{28}Si	^{197}Au	^{32}S	^{208}Pb	^{208}Pb	^{197}Au	^{197}Au	^{208}Pb
E^{max} (A GeV)	14.6	11	200	158	40	0.91e4	2.1e4	1.9e7
$\sqrt{S_{NN}}$ (GeV)	5.4	4.7	19.2	17.2	8.75	130	200	6000
$\sqrt{S_{AA}}$ (GeV)	151	934	614	3.6e3	1.8e3	2.6e4	4e4	1.2e6
$\Delta(y/2)$	1.72	1.58	2.96	2.91	2.22	4.94	5.37	8.77

Table 2.1: Parameters of RHIC and other existing and future facilities. A_{max} is the element with the max mass number. E_p^{max} is the max (equivalent) fixed-target beam energy per nucleon. S_{NN} represents the maximum center of mass energy per nucleon. S_{AA} is the total center of mass energy, and $\Delta y/2$ is the rapidity gap from the beam to the mid-rapidity.

RHIC: STAR[21], PHENIX[22]³, PHOBOS⁴[23] and BRAMS⁵ among which STAR and PHENIX detectors are large multi-purpose detectors. The data analyzed in this thesis are taken with STAR.

2.2 RHIC

As one of the most important colliding beam facilities in United States, the RHIC accelerator is designed to delivering the highest energy nucleus-nucleus (Au+Au) and polarized proton-proton (p+p) collisions in history. This allows a vigorous scientific program to explore many physics related to nuclear matter and strong interactions at

³PHENIX, the Pioneering High Energy Nuclear Interaction eXperiment, is an exploratory experiment for the investigation of high energy collisions of heavy ions and protons. PHENIX is designed specifically to measure direct probes of the collisions such as electrons, muons, and photons.

⁴The PHOBOS experiment is based on the premise that interesting collisions will be rare, but that when they do occur, new physics will be readily identified. Thus the PHOBOS detector is designed to examine and analyze a very large number of unselected gold ion collisions. For each collision, the detector gives a global picture of the consequences of the collision and detailed information about a small subset of the nuclear fragments ejected from the high energy-density region.

⁵Broad Range Hadron Magnetic Spectrometer

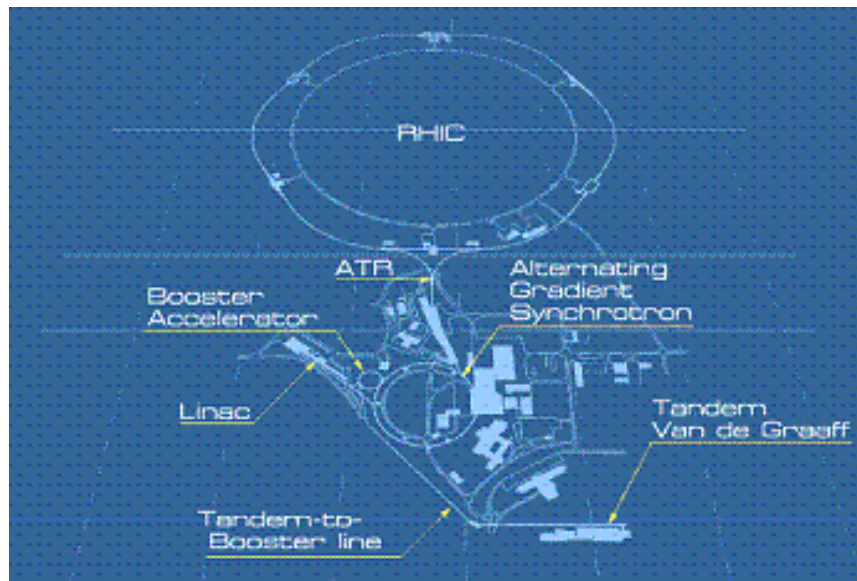


Figure 2.1: BNL RHIC accelerator complex. All four detector are located at different positions on the RHIC Ring

extreme energetic conditions. The center of mass energy can reach to about ten times the energy in a fixed target experiment. Table 2.1 gives the parameters of existing and future high energy facilities.

Fig. 2.1 shows the BNL accelerator complex including the main storage rings of RHIC and the pre-accelerators, which accelerate the particles up to the injection energy. RHIC consists of two main concentric storage rings with a diameter of 1.22km . Each of them is equipped with super-conducting magnets to guide and focus the colliding beams. For Au+Au experiments the two rings store counter-rotated Au ion beams at relativistic energy. At first the stripped gold nuclei (with charge $Q = -1e$) were accelerated upto $15\text{MeV}/u$ by the first Tandem Van de Graff accelerators. Then the ions are passing through a stripping foil (in between the Van de Graff accelerators)

Top Au+Au $\sqrt{S_{NN}}$	200GeV
Avg. luminosity \mathbf{L} (10 hour storage)	$2 \times 10^{26} cm^{-2} s^{-1}$
Bundles per ring	60
Gold ions per bunch	10^9
Crossing points	6
Beam lifetime (storage length)	10 hours
RHIC circumference	3833.845 m

Table 2.2: Nominal RHIC parameters for Au+Au collisions

and obtain a charge state of $Q = +12e$ (the most probable state) and an additional $1MeV$ per nucleon. On exiting the Tandem, the ions pass through a second stripping foil bringing their most probable charge to $Q = +32e$. They are then injected into the Booster synchrotron and accelerated to $95MeV/u$. A stripping foil in the transfer line between the booster and the Alternating Gradient synchrotron(AGS) increases their charge state to $Q = +77e$. In the AGS the ions are accelerated to $10.8GeV/u$. They are extracted from the AGS and passed through one final stripper foil where the remaining K-shell electrons are knocked off ($Q = +79e$). Finally, they are injected into RHIC where they are accelerated to the top energy and can be stored up to 10 hours. Table 2.2 lists important parameters for RHIC.

Up to date, RHIC has generated collisions between gold nuclei at 22, 56, 63, 130 and 200 GeV, between protons at 200 GeV and between gold and deuterium nuclei at 200 GeV. The data used in this thesis are taken in 2001 with STAR. During that year high statistics samples were taken for Au+Au and p+p collisions

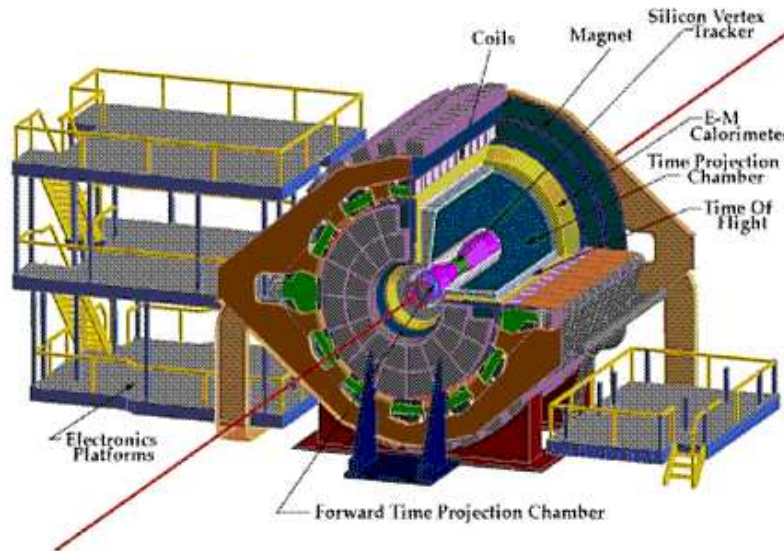


Figure 2.2: Overview of STAR Detector

2.3 STAR Detector

The STAR detector is the largest detecting systems at RHIC. As shown in Fig. 2.2 and 2.3, STAR is built around a large acceptance ($0 \leq \phi \leq 2\pi, -1.4 \leq \eta \leq 1.4$) TPC⁶ that provides high precision tracking of charged particles. Closed to the beam pipe, the TPC is augmented by a silicon inner tracking system called SVT⁷ which consists of four radial layers of silicon detectors for high precision space resolution. They improve the vertex resolution of the detector and allow the secondary vertex reconstruction of short lifetime particles. Outside the TPC the highly segmented BEMC⁸ is located which provides measurements of

⁶Time Projection Chamber

⁷Silicon Vertex Tracker

⁸Barrel Electromagnetic Calorimeter

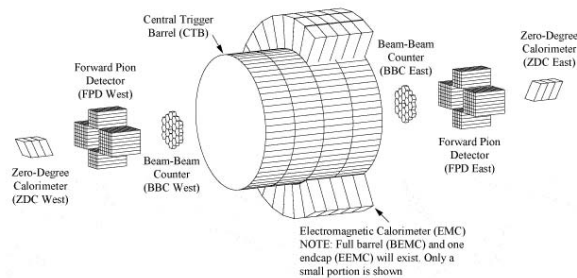


Figure 2.3: STAR Detector trigger components

photons and electrons. The $2.8 \leq |\eta| \leq 3.8$ is instrumented with FTPCs⁹ which also perform tracking for charged particles. All the detectors are housed in a room temperature and 0.5 T solenoidal magnet with a field parallel to the beam line, providing ability to perform momentum measurements of charged particles. Additionally, several detector subsystems are used for event selection purposes such as the ZDC¹⁰, the BBC¹¹ and CTB¹²(see Figure 2.3). I will try to give a brief introduction to some of these detectors and more detail on the TPC in the following sections.

⁹Forward Time Projection Chamber

¹⁰Zero Degree Calorimeter

¹¹Beam Beam Counter

¹²the Central Trigger Barrel

2.4 Zero Degree Calorimeter (ZDC)

High Energy collisions of nuclei usually lead to the emission of evaporation neutrons from both “beam” and “target” nuclei. At the RHIC heavy ion collider with 100GeV per nucleon beam energy, evaporation neutrons diverge by less than 2 milliradians from the beam axis whereas charged fragments are deflected more. In this ‘zero degree’ region produced particles and other secondary particles deposit negligible energy when compared with that of beam fragmentation neutrons. The purpose of the RHIC zero degree calorimeters (ZDC’s) is to detect neutrons emitted within this cone along both beam directions and measure their total energy (from which we calculate multiplicity). A ZDC signal coincidence from the two beam directions is a minimal bias selection of heavy ion collisions. This makes it useful as an event trigger and a luminosity monitor and for this reason all four experiments at RHIC are using identical ZDC detectors. The neutron multiplicity is also known to be correlated with event geometry and will be used to measure collision centrality.

The two Zero Degree Calorimeters are located at the first bending magnets in the collider line (about 18 meters from the interaction vertex). Each is split into 3 modules, and each module consists of layers of lead and scintillator fibers going to a PMT¹³ and ADCs¹⁴. These devices determine the number of spectator neutrons, and act as an intra-RHIC normalizing detector.

¹³Photon Multiply tube

¹⁴Analog Digital Converter

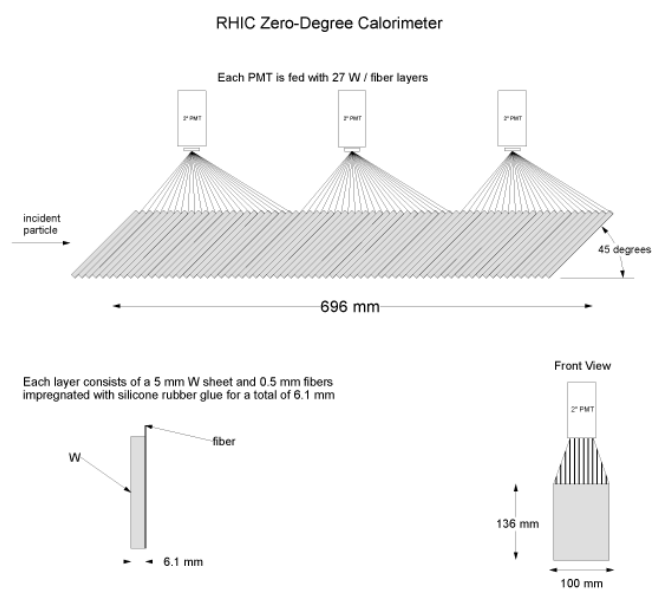


Figure 2.4: Zero Degree Calorimeters

2.5 Central Trigger Barrel

As shown in Figure. 2.3, the CTB is located around the radial exterior of the TPC. The CTB is made of a collection of scintillating tiles arranged in a cylindrical fashion. As charged particles travel through the tiles the generated scintillation photons are collected by PMTs and digitized and converted into electric signals. The amplitude of the signal is proportional to the multiplicity of the charged particles. The response time of the CTB is fast (260 ns) therefore in combination with the ZDC signal, it can provide a powerful charged particle multiplicity trigger. The whole CTB system consists of 240 slats of plastic scintillator which cover $0 \leq \phi \leq 2\pi$ and $-1 \leq \eta \leq 1$. Fig.2.5 shows a segment with two slats which are mounted in aluminum trays, two slats per tray. The CTB calibration yields an average 5 ADC counts for one minimum ionizing charged particles. For central Au+Au collisions the average occupancy per CTB tile is about 10 hits per slat, however in p+p collisions is about 0.05 per event.

2.6 Beam Beam Counter (BBC)

The ZDC and CTB are specifically designed for triggering in Au+Au collisions. The multiplicity of p+p collisions is much less and therefore requires a different trigger subsystem. The BBC is implemented to mainly work as the trigger subsystem for p+p collisions.

The BBC consists of two disk shaped scintillating detectors, with one placed at each end cap of the TPC(3.5 m from the interaction point). 2.6 shows a schematic drawing of one of the two BBC detectors. Each BBC disk is composed of scintillating tiles that are arranged in a hexagonal packing. For the first p+p run, only the small

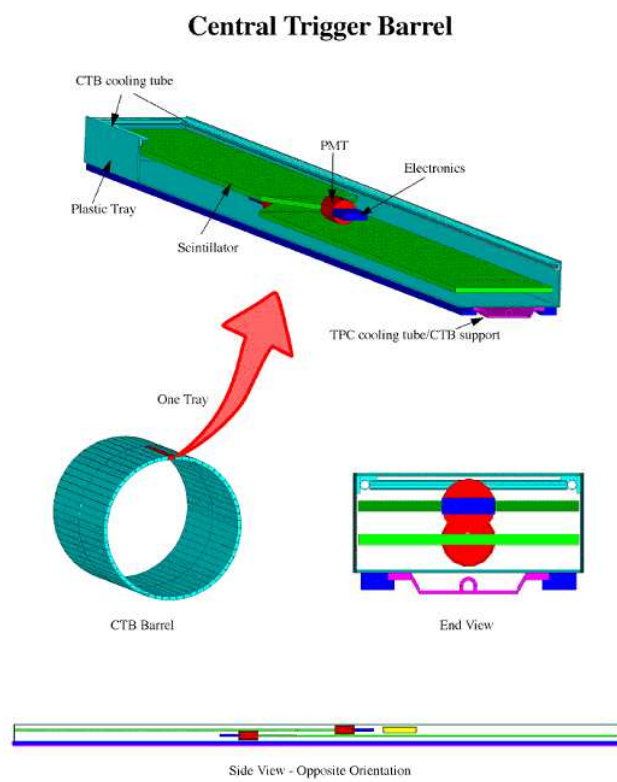


Figure 2.5: The Central Trigger Barrel at STAR

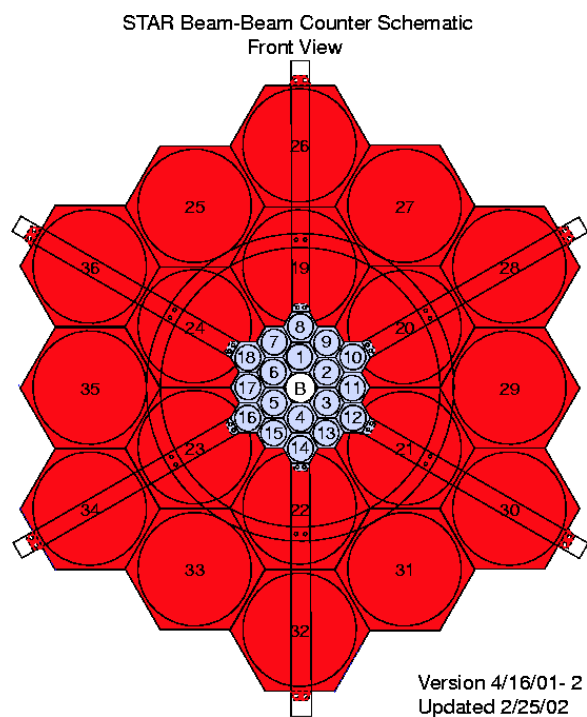


Figure 2.6: A beam's eye view of BBC. The beam is perpendicular to the page and intersects the BBC in the non-instrumented region labeled "B". For scale, the inner region(1-18) lie within an approximate circle of radius 10 cm

tiles in the inner region were instrumented with read out electronics, yield an active region of $3.3 \leq |\eta| \leq 5.5$. The RHIC beam passes through the center of the BBC (see Fig. 2.6) with 1 cm annular clearance. Eight PMTs were used for the 18 inner tiles. Each tile has a circular groove inscribed around the perimeter, into which a wave length shifting optical fiber is embedded. The scintillation light is collected in the fiber, sent to a PMT and digitized via an Analog to Digital converter (ADC). The tiles are grouped to allow for radial and azimuthal segmentation of the readout. The grouping is: 1, 2-3, 4, 5-6, 7-9, 10-12, 13-15, and 16-18. The full segmentation of the BBC was not used in the p+p trigger logic. The trigger summed the output of all tiles on the BBC, and a coincidence of both BBC's firing above noise threshold was required within a time window of 17 ns, which is determined by the time resolution of the detector. For future runs the BBC is being fully instrumented with electronics to maximize the potential acceptance and granularity.

2.7 Time Projection Chamber (TPC)

The main tracking device for STAR is the Time Projection Chamber. The large volume and acceptance of the TPC provides STAR with a great ability to reconstruct 3-D tracks of charged particles.

The TPC is a gas chamber. The large volume of gas is contained in a homogeneous electric field. Electrons, knocked off by the charged particles from the gas atoms will drift in the electric field to the detecting device at the end cap of the detector. Two coordinates in XY plane are determined by the location where the electrons are collected. The third coordinate (z) is reconstructed by using the time taken for the electrons to drift to the detector end cap and the drifting velocity of the electron

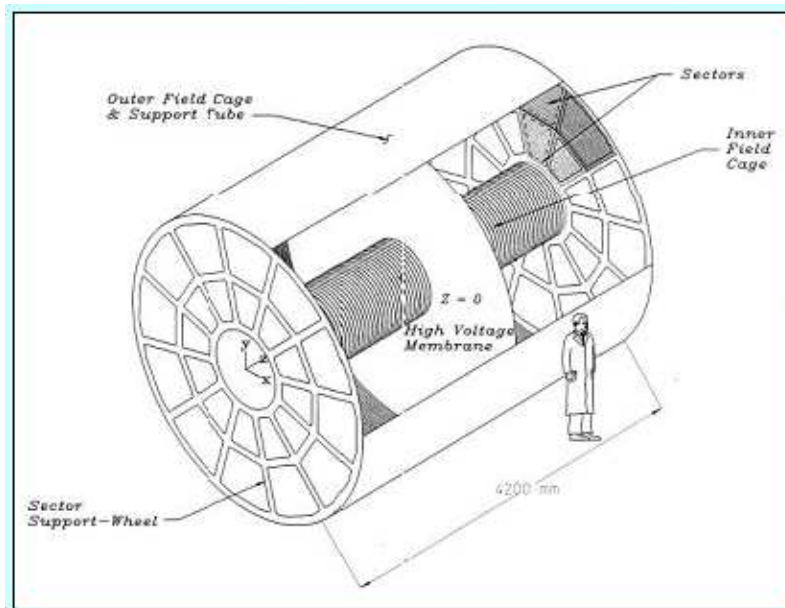


Figure 2.7: Side view of STAR-TPC

(v_{drift}) .

The TPC at STAR has a large acceptance and good momentum resolution. The 4.2 m long cylinder with a 4 m diameter is the largest single TPC in the world (see Fig 2.7). The cylinder is concentric with the beam line, and the inner and outer radii of the active volume are 0.5 and 2.0 m, respectively, which allows measurement of particle with $p_T > .15 \text{ GeV}/c$. The TPC has full azimuthal coverage ($0 < \phi < 2\pi$) and covers a pseudo-rapidity interval that ranges from $-2 < \eta < 2$ for the inner radius and $-1 < \eta < 1$ for the outer radius. To achieve sufficient p_T resolution a general requirement of 15 hits on each track will limit the pseudo-rapidity coverage to $-1.4 < \eta < 1.4$. The TPC volume is filled with P10 gas ($Ar, 10\% CH_4$) at 2 mbar above atmospheric pressure. A particle with charge z traversing a gas of charge

number Z and mass number A loses energy by ionizing the gas. The energy loss per distance traveled is given by the Bethe-Bloch formula.

$$\frac{dE}{dx} \approx K z^2 \frac{Z}{A} \frac{1}{\beta^2} \left(\frac{1}{2} \ln \frac{2m_e c^2 \beta^2 \gamma^2 T_{max}}{I^2} - \beta^2 \right) \quad (2.7.1)$$

Where $K \sim 0.31 MeV cm^2$, and β and γ are the usual relativistic variables. T_{max} is the maximum kinetic energy imparted to a free electron in a single collision, and I is the mean excitation energy. This formula has been implemented in the STAR analysis in order to determine the particle identification of low transverse momentum particles at STAR.

The secondary electrons are drifting in the electric field to two detection planes, one on each end of the chamber. A large diaphragm, made of carbon coated kapton with a thickness of $70\mu m$ is stretched between the inner and outer field cages at the center of the TPC. The central membrane is maintained at a high voltage ($35kV$) with respect to the detection planes. The mean drift time constitutes a measurement of the electrons ionization point along the z axis, yielding the third dimension. The TPC consists of 12 sectors in the ϕ plane. Each of the 12 sectors is subdivided into inner and outer subsectors characterized by a change in the readout padrow geometry. The pad design consists of straight rows of pads in each subsector and is shown in Figure 2.8. The design of the sub sectors was intended to enhance the event reconstruction in two important ways. The inner sector, where the track/hit density is highest, uses a smaller size pad, 2.85 by $11mm^2$, in 13 rows to improve the hit resolution. This will improve tracking by reducing the occurrence of split tracks which can be essential to many analyses including weak decay particle reconstruction and HBT etc. In the outer sector, where the hit occupancy is relatively low, the pad geometry is optimized for particle identification. Thus the pad size is increased to

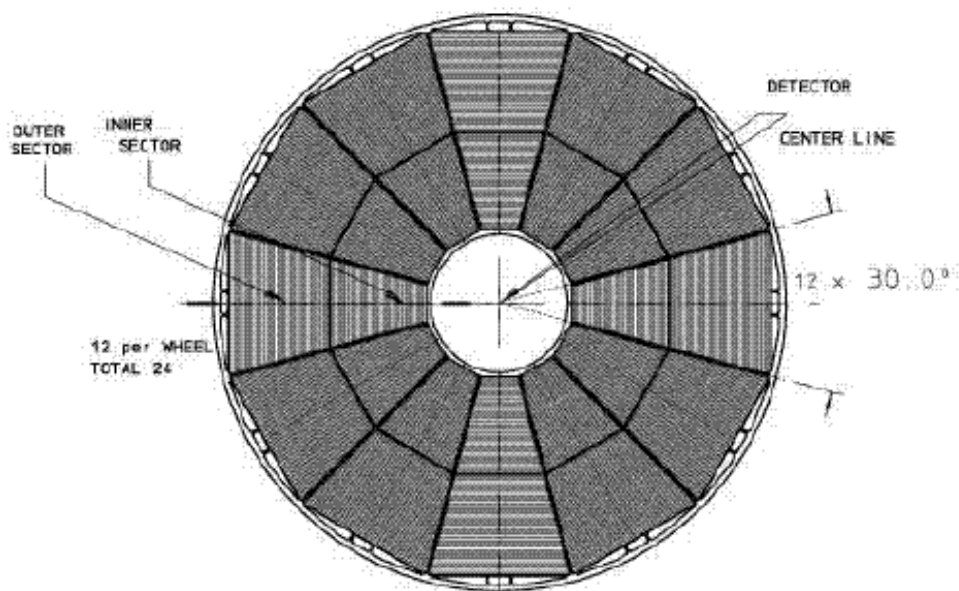


Figure 2.8: Sectors of the STAR-TPC

improve the measurements of the gas ionization. The outer sector consist of 32 rows of pads of 6.2 by 19.5 mm^2 . The TPC gas chamber is surrounded by both an inner and outer field cage which controls the voltage drop and subsequent electric field between the high voltage central membrane and the multi-wire proportional chamber (MWPC) and gating grids located just above the pad array for the two sections of each sector at the TPC endcap. The electrons produced from particles ionizing the gas as they traverse the detector drift towards the end of TPC and are amplified as an avalanche of electrons by the MWPC. These charges are imaged onto the pads and read out with a sampling rate of $100MHz$, binned into 512 time buckets. The electrode geometry of the MWPC is shown in Figure 2.8 and again shows a change in design elements between the inner and outer sub sectors. The choice of drift gas was

based on several features necessary for optimal TPC performance. Among them were the constraints that the gas be under atmosphere pressure, and that the gas must have a drift velocity $v_{drift} > 2cm/\mu s$ in an electric field $E < 300V/cm$. A mixture of 90% argon to 10% methane (P10) was selected. The drift speed of P10 at 130 V/cm is $5.5cm/\mu s$. Also of importance is the signal broadening introduced to the hit reconstruction by diffusion of the drift electrons in the gas chamber. The diffusion coefficients for P10 in the beam direction are $320 \mu m/\sqrt{cm}$ and in the transverse direction is about $540 \mu m/\sqrt{cm}$ which correspond to signal widths of 0.3 cm and 0.8 cm ,respectively.

Data used in this thesis is taken through the TPC tracking only.

Chapter 3

Azimuthal Correlations: Introduction

In this chapter I am going to give general introduction to the azimuthal correlations of particles with high transverse momentum (p_T). I will try to discuss in detail the components of azimuthal correlations as well as the different analysis techniques for different collision systems ($AuAu$, pp etc).

3.1 Definition of the Azimuthal Correlations

Generally we can define the two particle azimuthal correlation function for an integrated rapidity region $\eta \in [\eta_1, \eta_2]$ as follows:

$$C(\Delta\phi) = \frac{1}{N_{trigger}} \iint \frac{dN_{pair}(p^{trig}, p^{asso})}{\epsilon_a(p^{asso})} d^3p^{trig} d^3p^{asso} \delta(\phi^{asso} - \phi^{trig} - \Delta\phi) \quad (3.1.1)$$

$$\Delta\phi = \phi_{trigger} - \phi_{associate} \quad \Delta\phi \in [\phi_0, 2\pi - \phi_0]$$

The trigger particles are selected to be the particles with the higher transverse momentum. For each associated particle, $\Delta\phi$ is calculated by simply taking the difference of the azimuthal angle between the trigger particle and associated particle. A

weighted entry is then put into the correlation function as the function of $\Delta\phi$. The weight is equal to $1/\epsilon$, where ϵ is the detector efficiency of the associated particle. $C(\Delta\phi)$ should have dependencies on the transverse momentum of both the trigger and the associated particles. It should also have dependencies on the impact parameter of the collision. For a jet fragmentation process, the fragmented particles within the jet cone are correlated in momentum space. In the center of mass frame, the angle between the fragments of jet and the jet axis is small, therefore the azimuthal correlation of such a process always has a peak around zero. At the same time, due to the momentum conservation of the original hard scattering, the correlations between the jet and the particles created on the opposite side form a peak around π in the azimuthal correlation function. For uncorrelated sources, since the angle between the trigger and associated particle is random, the azimuthal correlation should be flat or in other words uniformly distributed over $\Delta\phi$. In most cases the contribution to the correlation from the random source can be calculated quite accurately by using statistics method. I will address this in detail later in this chapter. In Figure 3.1, I illustrate how the hard scattering contributes to the azimuthal correlation, which is usually sufficient to describe a pp collision. However for a more complex system such as a Au+Au collision, more considerations need to be taken into account, such as collision centrality and elliptic flow. Figure 3.2 and 3.3 show the sample correlations for p+p and Au+Au collisions. It is quite obvious that in central AuAu collisions the uncorrelated background is much higher than it pp. They all show jet-like structures (same side and back side). The details comparison will be covered later. One might ask the question, why do we analyze azimuthal correlations? In general, correlations from jet processes should be correlated in 3D momentum space not only in

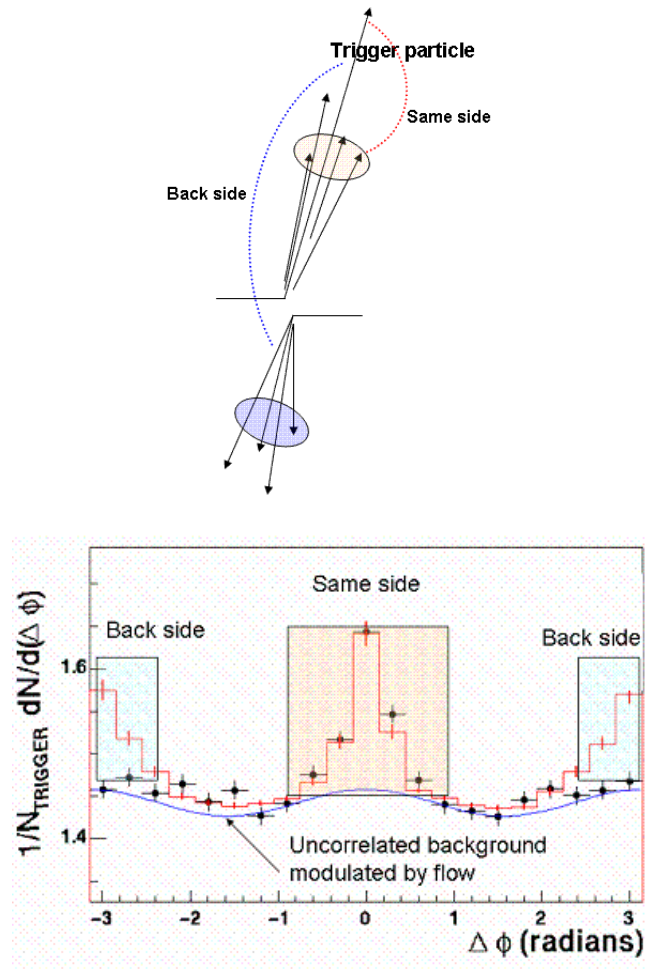


Figure 3.1: Azimuthal correlation function from hard scattering.

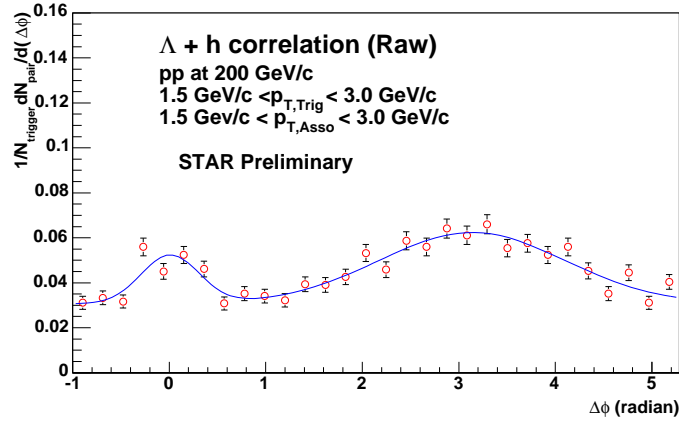


Figure 3.2: Sample of the correlation function. Blue dash line shows the fit of two Gaussian and a flat background.

$2D$. The answer to the question is that only in the center of mass of the coordinate system, the angular correlations of jets have a well defined shape. In the longitudinal direction, because of large initial longitudinal energy, a small difference in the longitudinal momentum will shift the center of mass away from lab frame and therefore twist the correlation function. Other effects such as acceptance and efficiency can also increase the difficulty of measuring the 3D angular correlation. Secondly, the correlations that have been studied are very p_T dependent which causes systematic errors which need to be studied carefully. Finally, the symmetry of azimuthal correlations sometimes allow auto-cancellation of the background, which could be useful especially when statistics is limited.

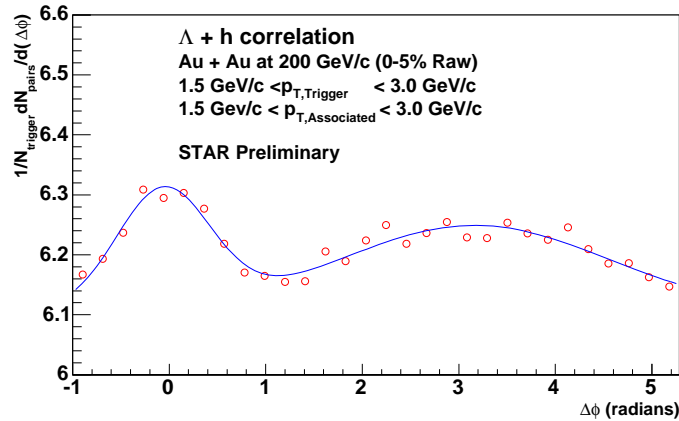


Figure 3.3: Sample of the correlation function Au+Au, a more complicated system. The fitting curve includes a Gaussian and a flat background and back side cosine term.

3.2 Components of the azimuthal correlation function

In this section, I am trying to illustrate different components of the azimuthal correlation for pp collisions and Au+Au collisions.

3.2.1 pp collisions

As shown in Figure 3.2, for the pp system, the correlation has same side peak and back side peak over a flat background. The same side and back side peak are presumedly the jet related signal. However we need to make sure we understand the physical meaning of such measurements. The amplitude of the normalized correlation for each $\Delta\phi$ basically tell us the number of associated particle per trigger in that direction. In

pp systems both same side and back side are coming from the fragmentation processes (Figure 3.1). A natural treatment to the data would be to assume that both peaks have Gaussian shapes. For the same side, the width of the Gaussian provides us with the size of jet cone which is related to the j_T of the jet fragmentation process. For the back side, width of the peak is affected by both j_T and k_T (see Appendix A). The integrated yield provides us with information about the multiplicity in the jet. As mentioned in the introduction, such method have been used in the previous studies on jet quenching effects from the hot dense medium [17][18].

3.2.2 AuAu collisions

AuAu collisions are more complicated than pp. From Figure 3.3 we can see a much larger flat background. Further more, the background in AuAUs includes a harmonic shape distribution called elliptic flow [24]. In the following I am giving a brief introduction to elliptic flow, and then we will discuss how it will affect the correlation function.

3.3 Elliptic flow

Fig 3.4 shows the beam's-eye view of a non-central Au+Au collision. The collisions of non-zero impact parameter creates a colliding zone shaped like an almond. Such asymmetries in the position space of the initial state cause an anisotropy in the momentum space in the final state. In a simple picture, the initial geometry of the collision creates a pressure gradient so that particle moving in different directions get a different push. Such effect will cause an asymmetry in the momentum space with

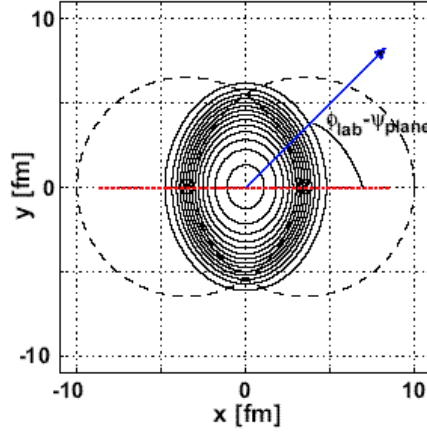


Figure 3.4: The asymmetric overlap region in a non-central ($b > 0$) heavy ion collision. The projection of the reaction plane onto the $X - Y$ plane is represented by the red line at $y = 0$. Blue line indicates the trajectory of the hadrons.

respect to the reaction plane. The geometrical asymmetry can be characterized by the eccentricity ϵ which is defined as:

$$\epsilon = \frac{\langle y^2 - x^2 \rangle}{\langle y^2 + x^2 \rangle} \quad (3.3.1)$$

ϵ can not be directly measured. But as I mentioned earlier, by using a certain model, we can get information about the collision centrality from the final particle production multiplicity at mid-rapidity and furthermore deduced the impact parameter and other initial conditions. Although such modeling is only statistical, we can still learn the general trends from peripheral to central collisions.

Fig 3.5 (left) shows that the azimuthal angle of produced hadrons has a harmonic shape with respect to the reaction plane. The distribution can be expanded in a Fourier series as follows:

$$\frac{d^3 N}{p_T dp_T dy d\phi} = \frac{d^2 N}{p_T dp_T dy} \left(1 + 2 \sum_n v_n \cos n[\phi - \Phi_{reactionplane}] \right) \quad (3.3.2)$$

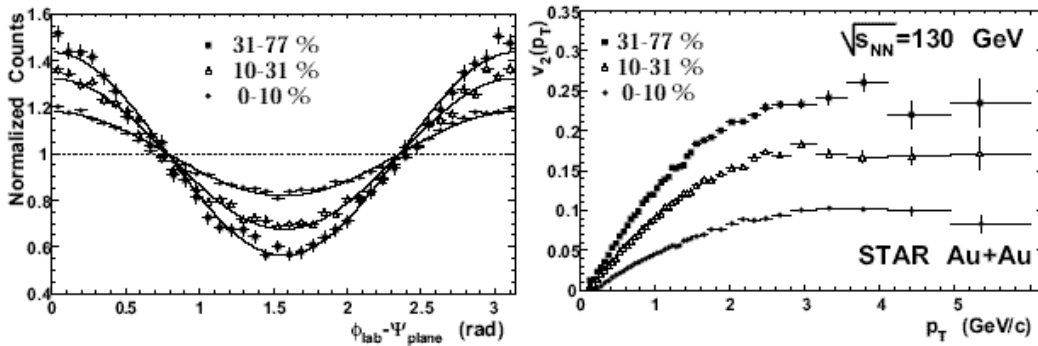


Figure 3.5: Left: Azimuthal correlation of charged hadrons respect to the reaction plane at p_T range $2.0 \text{ GeV}/c < p_{\perp} < 6.0 \text{ GeV}/c$ for AuAu collisions at $\sqrt{s_{NN}} = 130 \text{ A GeV}$. 0 – 10%, 10 – 31% and 31 – 77% represent different event classes with different collision centrality. Right: parameter v_2 as functions of p_T for different centrality classes

Fig. 3.5 (right) shows extracted the second order fourier component v_2 as a function of transverse momentum. By assuming the azimuthal distribution is due to the initial geometry condition, directly from the symmetry of "the almond shape" we can tell that all the odd components of the Fourier expansion should be zero at mid-rapidity. The non-trivial leading term v_2 corresponds to asymmetry of "in-plane" and "out-of-plane". Obviously v_2 should peak at peripheral collisions and fade out in most central collisions. These predictions have been confirmed by the experiment[24]. v_2 results have provoked many interesting discussions on many physics topics from collision dynamics to hadron production mechanisms. It is believed to be one of the most important measurements in high energy physics. In the later sections I will focus on how flow will affect two particle azimuthal correlations and jet correlation in general.

3.4 Uncorrelated Background of Azimuthal correlations

For two particle correlations, the uncorrelated background density should follow,

$$n_{bg}^{pair}(p_T^t, y^t, \phi^t, p_T^a, y^a, \phi^a) = n^a(p_T^a, y^a, \phi^a) n^t(p_T^t, y^t, \phi^t) \quad (3.4.1)$$

$$n_{bg}^{pair}(\Delta y, \Delta\phi) = \oint dy^a d\phi^a dy^t d\phi^t n^a(p_T^a, y^a, \phi^a) n^t(p_T^t, y^t, \phi^t) \delta(y^t - y^a - \Delta y) \delta(\phi^t - \phi^a - \Delta\phi) \quad (3.4.2)$$

Here we assume the trigger and the associated particles are uncorrelated. The random pair density should equal the product of the single particle densities. If integrated over the central plateau in $\eta \in [-1.0, 1.0]$ and $\Delta\eta \in [-2.0, 2.0]$ and certain p_T ranges for both trigger particle and associated particles equation 3.4.2 becomes

$$bg(\Delta\phi) = \int_{p_T^t} \int_{p_T^a} \int_{\Delta y} n_{bg}^{pair} dp_T^t dp_T^a d(\Delta y) \quad (3.4.3)$$

By assuming the background distribution is flat as a function of $\Delta\phi$, i.e. $\frac{dbg(\Delta\phi)}{d(\Delta\phi)} = 0$, it is easy to derive the following:

$$bg = bg(\Delta\phi) = \frac{1}{2\pi} \int_0^{2\pi} bg(\Delta\phi) d(\Delta\phi) \quad (3.4.4)$$

Using Equation 3.4.2, 3.4.3 and 3.4.4 we yields

$$bg(\Delta\phi) = \frac{1}{2\pi} \left[\int_{p_T^t, y^t, \phi^t} \frac{d^3 N^{trigger}}{dy^t dp_T^t d\phi^t} dy^t dp_T^t d\phi^t \right] \left[\int_{p_T^a, y^a, \phi^a} \frac{d^3 N^{associated}}{dy^a dp_T^a d\phi^a} dy^a dp_T^a d\phi^a \right] \quad (3.4.5)$$

The benefit of Equation. 3.4.5 is that the right hand side are two separated integral which can be calculated independently. For mid-rapidity region $\eta \in [-1, 1]$ or $\eta \in [-0.5, 0.5]$, the single particle integral over η and ϕ becomes simply the inclusive p_T

spectrum. Notice that the uncorrelated background is determined completely by the inclusive p_T spectra of trigger and associated particles. That is.

$$bg(\Delta\phi) = \frac{1}{2\pi} \int_{p_T^t} \int_{p_T^a} dp_T^t dp_T^a \frac{dN^{trigger}}{dp_T} \frac{dN^{associate}}{dp_T} \quad (3.4.6)$$

where

$$\frac{dN}{dp_T} = \int_y \int_\phi \frac{d^3N}{dy dp_T d\phi} dy d\phi \quad (3.4.7)$$

Usually $\frac{dN}{dp_T}$ can be easily measured. If the associated particle spectrum is not related to trigger, i.e. the cuts applied to obtain associated particles are irrelevant to obtain trigger particles, the background for the normalized correlation function depends only on the associated particle alone. If some cuts are related, such as $p_T^{associated} < p_T^{trigger}$, the background can still be calculated using Equation 3.4.6. For a normalized correlation the background can be expressed as,

$$BG = \frac{1}{2\pi} \frac{\int_{p_T^t} \int_{p_T^a < p_T^t} \frac{dN^{trigger}}{dp_T} \frac{dN^{associate}}{dp_T} dp_T^t dp_T^a}{\int_{p_T^t} \frac{dN^{trigger}}{dp_T}} dp_T^t \quad (3.4.8)$$

As we can see from Equation 3.4.8 the denominator equals the total number of trigger particles selected for the correlation function.

In practice, this method needs to be applied independently for different centrality classes. It should only be applied to rare correlation condition, i.e. the total yield of correlations should be small compared to the uncorrelated background. Therefore correlated hadron production contribution to the inclusive single particle spectra is negligible. For jet like correlations this condition generally holds. In the data analysis chapter I will discuss the calculated background compared to the correlation function. As we will see, this method works surprisingly well in all the centralities and pp.

In order to improve statistics we need to sometimes combine different centrality classes to obtain the correlation function. The correlation function (Equation 3.1.1)

can be rewritten as:

$$C_{combine}(\Delta\phi) = \frac{1}{N_{total}} \sum_i (N_i^{trig} \cdot C_i(\Delta\phi)) \quad (3.4.9)$$

$$N_{total} = \sum_i N_i^{trig} \quad (3.4.10)$$

where $C_i(\Delta\phi)$ is the correlation function for each class. We can also construct the background in a similar way.

$$BG_{combine}(\Delta\phi) = \frac{1}{N_{total}} \sum_i N_i^{trig} \cdot BG_i(\Delta\phi) \quad (3.4.11)$$

where $BG_i(\Delta\phi)$ represents the background for each individual class. The statistical error for the background calculation can be expressed from the statistical error from the single particle spectra. This method relies on a uniform $\Delta\phi$ distribution of the background. Generally, as long as the $\Delta\phi$ distribution can be modulated (numerically or analytically), these methods are still applicable. The shape of the background in $\Delta\phi$ is determined by the detector acceptance and efficiency. In STAR, due to the full azimuthal acceptance of the detector, the shape is flat. This reduces many of the systematics in the measurements. However uncorrelated background in the jet correlation has a harmonic shape which caused by elliptic flow. In the next section I will discuss about how to estimate the flow contribution to the correlation function.

3.5 Elliptic Flow v_2 in two particle azimuthal correlations

For simplicities, I assume that the single particle azimuthal distribution depends only on ϕ and v_2 . Hence both trigger and associated particle distribution follow:

$$\begin{aligned}\frac{d^3 N_{associated}}{dp_T dy d(\Delta\phi)} &= \frac{d^2 N}{dp_T dy} (1 + 2v_2^{associated}(p_T) \cos 2\phi_{associated}) \\ \frac{d^3 N_{trigger}}{dp_T dy d(\Delta\phi)} &= \frac{d^2 N}{dp_T dy} (1 + 2v_2^{trigger}(p_T) \cos 2\phi_{trigger})\end{aligned}\quad (3.5.1)$$

Where v_2 represents the second order harmonics. For uncorrelated background from Equation 3.4.2, we have

$$n^{pairs}(p_T^t, p_T^a, \phi^t, \phi^a, y^t, y^a) = \frac{d^2 N_t}{dp_T dy} \frac{d^2 N_a}{dp_T dy} (1 + 2v_2^a(p_T^a) \cos 2\phi_a)(1 + 2v_2^t(p_T^t) \cos 2\phi_t) \quad (3.5.2)$$

after rapidity integration we get,

$$bg^{pair}(\phi^t, \phi^a, p_T^t, p_T^a) = bg(p_T^t, p_T^a)(1 + 2v_2^a \cos 2\phi_a + 2v_2^t \cos 2\phi_t + 4v_2^a v_2^t \cos 2\phi_a \cos 2\phi_t) \quad (3.5.3)$$

$$\begin{aligned}bg^{pair}(\phi^t, \phi^a) &= bg(p_T^t, p_T^a)(1 + 2v_2^a \cos 2\phi_a + 2v_2^t \cos 2\phi_t \\ &\quad + 4v_2^a v_2^t [\frac{1}{2} \cos 2(\phi^t + \phi^a) + \frac{1}{2} \cos 2(\phi^t - \phi^a)])\end{aligned}\quad (3.5.4)$$

In order to find distribution as the function of $\Delta\phi$, we need to integrate over ϕ , Let's define transformation,

$$\begin{aligned}\Delta\phi &= \phi^t - \phi^a; \\ \phi^a &= \phi^t - \Delta\phi; \\ \phi^t + \phi^a &= 2\phi^t - \Delta\phi;\end{aligned}$$

$$\begin{aligned}
bg(\Delta\phi, p_T^t, p_T^a) &= \int_{\phi^t} n^{pairs}(\phi^t, \phi^a) d\phi^t d\phi^a \delta(\phi^t - \phi^a - \Delta\phi) \\
&= bg(p_T^t, p_T^a) \int_0^{2\pi} d\phi^t (1 + \\
&\quad 2v_2^a \cos 2(\phi_t - \Delta\phi) + \quad (A) \\
&\quad 2v_2^t \cos 2\phi_t + \quad (B) \\
&\quad 2v_2^a v_2^t \cos 2(2\phi^t - \Delta\phi) + \quad (C) \\
&\quad 2v_2^a v_2^t \cos 2\Delta\phi) \\
&= \frac{1}{2\pi} bg(p_T^t, p_T^a) (1 + 2v_2^a v_2^t \cos 2\Delta\phi) \\
&= \frac{1}{2\pi} bg(p_T^t, p_T^a) (1 + 2v_2^{effective} \cos 2\Delta\phi)
\end{aligned} \tag{3.5.5}$$

We find out that when integrating over ϕ^t terms, (A),(B) and (C) leave the only the unity term and the $\cos 2\Delta\phi$ term with the coefficient proportional to the product of v_2 s of the trigger and the associate particles. Thus, the effect of the ecliptic flow modulates the uncorrelated background of the correlation function into a new second order harmonic in $\Delta\phi$ with coefficient $v_2^{effective} = v_2^t \cdot v_2^a$. The flow correction can be very important for jet correlations studies since the flow peaks at 0 and π , the same location where the same side and back side jet correlations peak. Fortunately many independent v_2 measurements are available. As we know, v_2 has a strong p_T dependence. For the chosen p_T ranges of trigger and associated particles, we can calculate the effective v_2^{effect} by using the convolution of the single particle spectra of triggers and associates. For example ,the conditions $p_T^t \in [P_0, P_1]$ and $p_T^a \in [p_0, p_T^t]$, the $v_2^{effective}$ can be calculated as:

$$v_2^{effective} = \frac{\int_{P_0}^{P_1} dp_T^t \int_{p_0}^{p_T^t} dp_T^a bg(p_T^a, p_T^t) v_2^t(p_T^t) v_2^a(p_T^a)}{\int_{P_0}^{P_1} dp_T^t \int_{p_0}^{p_T^t} dp_T^a bg(p_T^a, p_T^t)} \tag{3.5.6}$$

For the analysis, the effective flow contribution to the correlation function has been calculated using the convolution of independently measured v_2 s as a function of p_T for trigger and associated particles. Every calculation has been done within the same centrality classes. For combined centrality classes, an effective flow v_2 has been calculated using.

$$v_2^{combine} = \frac{1}{BG_{total}} \sum_i BG_i v_{2,i}^{effective} \quad (3.5.7)$$

where BG_i is the background for each event class and $BG_{total} = \sum_i BG_i$. In particular for charged hadrons, v_2 from different analysis methods such as reaction plane method and 4-particle cumulant method, are used and compared. The correlation $v_2^{effective}$ is proportional to v_2^2 , therefore in central Au+Au collisions the magnitude of $v_2^{effective}$ is on the order of a few tenths of percent. It will not affect the correlation function much. However for mid-central and peripheral collisions, the flow effects can be rather large.

3.6 Analysis techniques overview

For azimuthal correlation studies, depending on the physics topic one is interested in, different analysis techniques can be applied. This thesis is focusing on jet correlations [25][26][27]. Measurement of jet correlation yields and widths for same and back side jets are believed to related to jet fragmentation processes and medium modification effects. Elliptic flow is usually treated as background. In the following, I discuss different models for jet correlation analysis.

3.6.1 Reference Model

The basic idea of the reference model is to assume that jet correlations in $Au + Au$ collisions should be identical to pp .

$$\begin{aligned}
 C_{pp} &= BG + Jet_{pp} \\
 C_{AA} &= BG(1 + v_2^{effective} \cos(2\Delta\phi)) + Jet_{AA} \\
 Jet_{AA} &\Leftrightarrow Jet_{pp}
 \end{aligned} \tag{3.6.1}$$

For pp collisions, jet correlations for both, same side and back side, can be fitted with Gaussian functions. The whole correlation function can then be fitted with the following function.

$$f^{pp}(\Delta\phi) = BG + c_1 e^{-\frac{(\Delta\phi - \phi_0)^2}{2\sigma_{same}^2}} + c_2 e^{-\frac{(\Delta\phi - \phi_1)^2}{2\sigma_{back}^2}} \tag{3.6.2}$$

where σ_{same} and σ_{back} representing the width of same side and back side, respectively. The finite width in pp collisions are related to the j_T and k_T effects related to in jet/di-jet fragmentation. (See Appendix A for details). The integrated area can be calculated by using the parameters of the function. Based on the definition 3.1.1 the yield under the peak on the same and back side can be understood as the number of associated particles per trigger particle. It is quantitatively equivalent to the multiplicity of hadrons within the jet cone in the chosen associated p_T bin.

For $AuAu$, based on the reference model, we can applied the following function as:

$$f^{AA}(\Delta\phi) = BG(1 + 2v_2^{effective} \cos 2\Delta\phi) + c_1 e^{-\frac{(\Delta\phi - \phi_0)^2}{2\sigma_{same}^2}} + c_2 e^{-\frac{(\Delta\phi - \phi_1)^2}{2\sigma_{back}^2}} \tag{3.6.3}$$

An alternative method to retrieve the same side and back side signal is the bin counting method. This method does not require knowledge of the shape of the signal

but only the shape of the background. This is quite useful in central $AuAu$ collisions where the exact shape of the back side jet is not well defined.

3.6.2 Conservation of Momentum

Although the interactions of many particles in central Au+Au collisions can be complicated, the basic principles such as conservation of momentum still hold. The effect of conservation of momentum in correlation studies was first calculated by Borgini et al [28]. In general, conservation of momentum creates a negative $\cos \Delta\phi$ term on the back side. The magnitude of conservation is as follows:

$$f(\Delta\phi) = -\frac{2 \langle p_T^t \rangle \langle p_T^a \rangle \cos(\Delta\phi)}{N_{mom} \langle p_T^2 \rangle} \quad (3.6.4)$$

In Appendix B. we will show how to obtain this formulism from first principles. In Equation 3.6.4, the correlation is proportional to the mean transverse momentum of trigger and associated particle. In the denominator, N_{mom} represents the number of particles that participate in conserving the momentum. $\langle p_T^2 \rangle$ represents the mean of the square of the transverse momentum for all these particles. The multiplicity and kinematics of the particles that conserve the momentum can give us information about the interaction scale of system. For $AuAu$ collisions, the momentum conservation term is very important when calculating the back side yield. In central $AuAu$ collisions, the back side correlations are broadened to a degree that it yields similar shape as the cosine function. However one needs to disentangle the background and real jet signal. In general we can apply the cosine fit on the back side as follows:

$$\begin{aligned}
f(\Delta\phi) &= BG(1 + 2v_2^{effective} \cos 2\Delta\phi + C_{MC} \cos \Delta\phi) + c_1 e^{-\frac{(\Delta\phi - \phi_0)^2}{2\sigma_{same}^2}} \\
C_{MC} &= -\frac{2 \langle p_T^t \rangle \langle p_T^a \rangle}{N_{mom} \langle p_T^2 \rangle}
\end{aligned} \tag{3.6.5}$$

Such a fit can be quite handy in central collisions, where the extremely broadened back side can not be fitted with a reasonable Gaussian function. Hence it is interesting to study the condition when the jet structure disappears.

3.6.3 Difference function

In particle identified correlation studies the data are usually limited by statistics. This prevents us from doing a direct correction for background and flow. An alternative method can be used to study the quenching factor, called the Difference Function:

$$\begin{aligned}
C_{diff} &= \frac{1}{N_{trigger}} (N_{same} - N_{back}) \quad (|\Delta\phi| < \phi_0) \\
&= \int_{-\phi_0}^{\phi_0} C(\Delta\phi) d(\Delta\phi) - \int_{\pi-\phi_0}^{\pi+\phi_0} C(\Delta\phi) d(\Delta\phi)
\end{aligned} \tag{3.6.6}$$

Due to the symmetry of the system, background and flow contributions automatically cancel out. In the cases when the flow parameters v_2 are not reliable or background subtraction can have a large influence on the jet signal, C_{diff} can be useful to studying the quenching effects without knowing the flow parameter. Furthermore one also can define the Differential Difference function as:

$$C_{fold}(\Delta\phi)_{(\Delta\phi \in [-\frac{\pi}{2}, \frac{\pi}{2}])} = C(\Delta\phi) - C(\pi - \Delta\phi) \tag{3.6.7}$$

C_{fold} has no flow and background components. The fitting function contains a positive same side and a negative back side. For a Gaussian back side,

$$f(\Delta\phi) = c_1 e^{-\frac{(\Delta\phi-\phi_0)^2}{2\sigma_{same}^2}} - c_2 e^{-\frac{(\Delta\phi-\phi_1)^2}{2\sigma_{back}^2}} \quad (3.6.8)$$

or for a momentum balance back side,

$$f(\Delta\phi) = c_1 e^{-\frac{(\Delta\phi-\phi_0)^2}{2\sigma_{same}^2}} - C \cos(\Delta\phi) \quad (3.6.9)$$

Such methods require an asymmetry in the jet correlation and these are more sensitive when the same side and back side have a significantly different shape. The benefits of this method are that it does not depend on the background and flow. The shortcoming is that the correlation results rely on the function we choose to fit. When the correlation does not have a well known form it will be hard to disentangle same side and back side.

In this chapter, we have discussed different methods related to jet correlation analysis. They all have their own pros and cons. We are using the fitting method most of the times. We sometimes use bin counting method for systematics studies. In some cases we also use the Difference Function when the data is limited by statistics.

Chapter 4

Data Analysis

In this chapter I will discuss about my data analysis procedure.

4.1 Data Set

This thesis is based on YEAR-2¹ data taken by STAR for *AuAu* and *pp* at $\sqrt{S_{NN}} = 200 \text{AGeV}$. For *AuAu* collisions, data of both MinBias and Central triggered events are combined to improve the overall statistics. Primary tracks² are determined from hit points in the main TPC and the momentum is calculated from the helix fit[29]. Figure. 4.1 and 4.2 shows a typical AuAu event for central collisions front view and side view. For central collisions, thousands of tracks make individual tracking seem impossible. But the actual occupancy in the TPC is still manageable because the large volume and the good spatial resolution of the detector. The production data used in this thesis are stored in *MuDst* and *StrangeMuDst* root files³ which contain

¹RHIC run in year 2001.

²Tracks from the primary collision vertex. Selections of primary tracks relies on reconstruction of primary vertex and the distance closest approach(DCA) to the primary vertex. In practices, certain geometry cuts are applied for the track selection.

³Root is an object-oriented data analysis framework developed by CERN. It provides extendable features which are convenient for a variety of jobs such as data analysis, simulation,online data monitoring and storage.

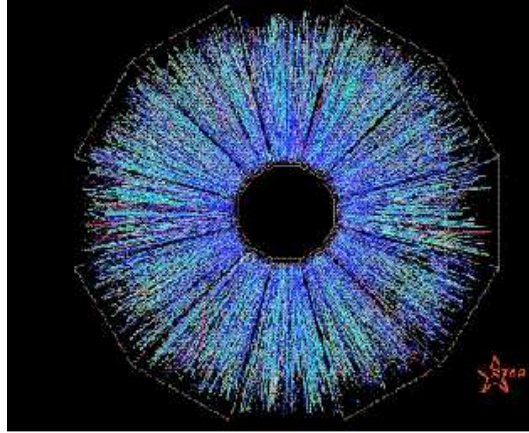


Figure 4.1: Front View of the TPC for Central *AuAu* Event at STAR

kinematic information about primary tracks, secondary tracks, and reconstructed particles. These files have been first pre-filtered into subsets which contain high p_T tracks only. In my analysis, in order to ensure quality of the tracks and correct momentum resolutions. I only use events with $|z_{vertex}| < 25$ cm where z_{vertex} is the distance of actual vertex in the beam direction to the geometry center. I also require tracks within the pseudo rapidity $[-1.0, 1.0]$ to ensure reliable tracking efficiency. In the next section I will discuss the definition of centrality.

4.1.1 Centrality

In Chapter one I have given an introduction about the Glauber model and centrality definition for AuAu collisions. The standard centrality definition in STAR is shown in Fig. 1.5. For MinBias Events, the number of event are plotted as a function of multiplicity in the central plateau ($\eta \in -0.5, 0.5$). By assuming the total cross section

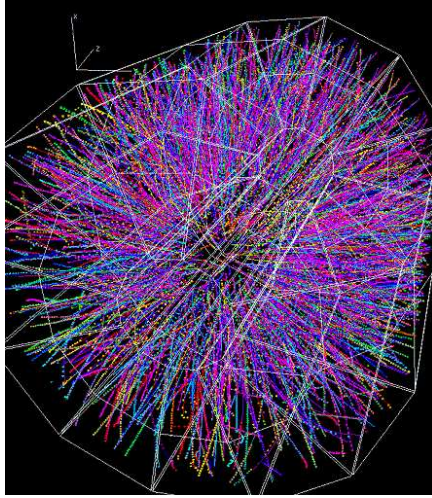


Figure 4.2: Side View of the TPC for Central $AuAu$ Event at STAR

is unity, we can get the percentage cross section as a function of multiplicity, as:

$$\sigma_{y \in [-0.5, 0.5]}(N_{low}, N_{up}) = \frac{N_{event}(N_{low} < N < N_{up})}{N_{event}(all)} \quad (4.1.1)$$

Table 4.1 lists the number of primary charged tracks for mid rapidity for different percentage of the total cross section.

In the table we can see that high multiplicity corresponds to central collisions which have small impact parameter and large number of participants. Low multiplicity corresponds to large impact parameter and a larger number of spectators. Based on the Glauber model, the number of participants for Au nuclei can be calculated. Table 4.2 lists the Glauber calculation for $AuAu$ collisions at STAR[17].

<i>centrality</i> (%)	$(\frac{dN}{dy})_{low}$	$(\frac{dN}{dy})_{up}$
0 – 5	510	/
5 – 10	431	510
10 – 20	312	431
20 – 30	217	312
30 – 40	146	217
40 – 50	94	146
50 – 60	56	94
60 – 70	30	56
70 – 80	14	30

Table 4.1: Centrality (percentage of total cross section) related to the mid-rapidity charged hadron multiplicity.

<i>Centrality</i> (%)	60 – 80	40 – 60	30 – 40	20 – 30	10 – 20	5 – 10	0 – 5
N_{part}	20 ± 6	61 ± 10	114 ± 13	165 ± 13	232 ± 11	298 ± 10	352 ± 7

Table 4.2: Glauber calculation of the number of participants in *AuAu* collisions

4.1.2 Statistics

For Year-2 data, after quality cuts, we are left with 2.7 million *AuAu* events, combining events of Central and MinBias Trigger and Full-Field and Reversed Full-Field magnetic field setting. 14 Million *pp* events have been scanned. Table 4.3 lists the statistics of high- p_T filtered events for different centralities in AuAu.

From the introduction we have learned that the single particle density determines the uncorrelated background in the correlation function. The jet correlations in *AuAu* collisions are generally small compared to the uncorrelated background. However the magnitude changes as a function of associated and trigger p_T .

centrality (%)	Statistics	h^\pm	Λ	$\bar{\Lambda}$	K_0^s
0 – 10	1.65M	11.08	0.1163	0.0913	0.0884
20 – 40	301k	3.03	0.0934	0.02656	0.0307
60 – 80	301k	0.516	0.006	0.00332	0.00503

Table 4.3: Single Particle ($p_T > 2.0 \text{ GeV}/c$) densities compared to uncorrelated backgrounds and correlation signals

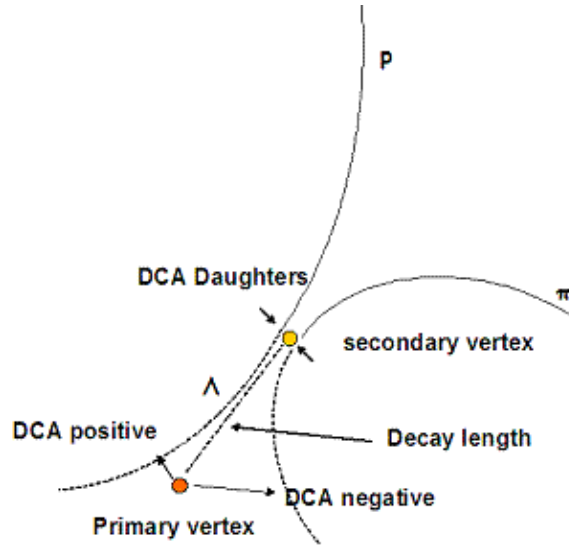
4.2 Trigger and associated particle selections

For jet correlation studies, trigger particles are usually chosen to be the highest p_T particles in an event. Different p_T ranges have been chosen for the associated particles for different purposes. For higher p_T ranges, the background is smaller. However, the analysis will be statistics limited. For lower p_T ranges, the statistics is better but the background is larger. In this thesis, the p_T of the trigger particle is chosen to be from 1.5 to 6.0 GeV/c for different particle species. The associated particle p_T is chosen to be above 1.0 GeV/c. I am always using unidentified charged hadrons as associated particles not only for statistics reasons but also to maintain a reliable tracking efficiency for the associated particles. As for trigger particles, we have studied several different particle species including unidentified charged hadrons, strange baryons ($\Lambda, \bar{\Lambda}$) and meson (K_0^s). From our definition of the correlation function, effects of the efficiencies of trigger particle are normalized out by definition, which makes all results directly comparable.

4.2.1 Unidentified charged hadrons

Unidentified charged hadrons are the charged particles detected by TPC without particle identification, because the $\frac{dE}{dx}$ information from TPC can hardly separate particles with transverse momentum above 1.0 GeV/c [30]. At lower energy the

V0 species	Λ	$\bar{\Lambda}$	K_0^S
Quark Content	uds	$\bar{u}\bar{d}\bar{s}$	$u\bar{s} + \bar{u}s$
Mass	1.1156 GeV/c^2	1.1156 GeV/c^2	0.4976 GeV/c^2
Γ_i/Γ	$p\pi^-$ (63.9%)	$\bar{p}\pi^+$ (63.9%)	$\pi^+\pi^-$ (68.9%)
Lifetime $\tau(\times 10^{-10}s)$ ($c\tau$)	2.632(7.89cm)	2.632(7.89cm)	0.895(2.684cm)

Table 4.4: Properties for V0 particles (Λ $\bar{\Lambda}$ and k_0^S)Figure 4.3: Reconstruction of the V0 particle Λ from its decayed daughters a proton p and a pion π

charged hadrons should be dominated by pion. They should also contain a significant amount of kaons($\sim 20\%$) and protons. At different p_T range, the particle ratio can be very different[31][32][33]. For example the p/π ratio is approaching 1.0 at higher p_T . Since we are only interested in the tracks coming from the primary vertex, in addition to the basic quality cuts we required $|DCA| < 1.0cm$ where DCA ⁴ is the distance from the primary vertex to the helix of track.

⁴Distance closest approach

4.2.2 V_0 reconstructed particles: Λ , $\bar{\Lambda}$, K_0^s

V_0 particles are neutral weakly decaying strange baryons and meson. Since they decay into positive and negative particles which can be detected, the shape formed by the daughter tracks (as shown in Fig 4.3 notice that neutral particle is invisible in the detector) in the magnetic field resembling a "V". Figure. 4.3 shows a Λ decaying into a proton and pion from which the Λ can be reconstructed. Table. 4.4 shows the basic properties of the V_0 particles including Λ , $\bar{\Lambda}$ and K_0^s and their main reconstruction channel. Since they decay weakly, the lifetimes of these particles allow them to escape from the collision vertex and decay at the secondary vertex. This makes it possible to reconstruct them from their decay daughters topologically, without knowing the exactly identity of their daughters. The basic mechanism is quite straight forward. For example, let us consider $\Lambda \rightarrow p\pi$. From the charged tracks detected by TPC, we can assume the positive track has the mass of p and the negative track has the mass of π^- , by requiring these tracks are coming from a secondary vertex (which should be different from the primary vertex) we can reconstruct the invariant mass at the decay vertex⁵. If the two tracks are actual daughters of the Λ , the reconstructed invariant mass should agree with the mass of the Λ . If not, the reconstructed mass should be part of a rather flat background distribution determined only by the kinematics of the daughters. The different shape of the background and the signal makes it possible to optimize geometrical cuts to improve the signal to background ratio. In Table4.5,4.6 and 4.7 I have listed the cuts we used to reconstruct our V_0 particles – Λ , $\bar{\Lambda}$ and K_0^s . The cut variables (see Figure 4.3) including: Event Vertex Z^6 ,DCA daughters

$${}^5m_{inv} = \sqrt{m_p^2 + p_p^2 + m_\pi^2 + p_\pi^2 - p_{V_0}^2}$$

⁶Primary vertex

Event Vertex Z	$ Z_{Vertex} < 65$ cm
DCA daughters	< 0.5 cm
Decayed length	> 6.0 cm
Fit points of daughters	> 15
DCA of positive daughter	> 1.05 cm
DCA of negative daughter	> 2.05 cm
Mass Λ ¹³	$(1.108 \text{ MeV}/c^2 < m_{\Lambda} < 1.122 \text{ MeV}/c^2)$

Table 4.5: Cuts Λ for $AuAu$ collisions @ 200 A GeV

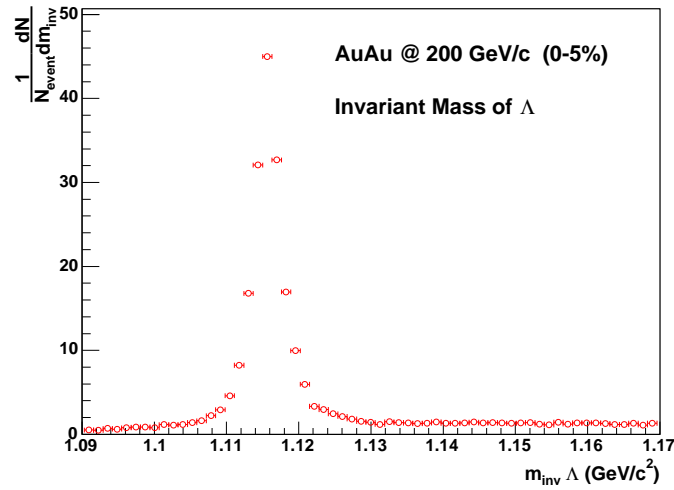
Event Vertex	$ Z_{Vertex} < 65$ cm
DCA daughters	< 0.5 cm
Decayed length	> 6.0 cm
Fit points of daughters	> 15
DCA of positive daughter	> 2.05 cm
DCA of negative daughter	> 1.05 cm
Mass $\bar{\Lambda}$	$(1.108 \text{ MeV}/c^2 < m_{\bar{\Lambda}} < 1.122 \text{ MeV}/c^2)$

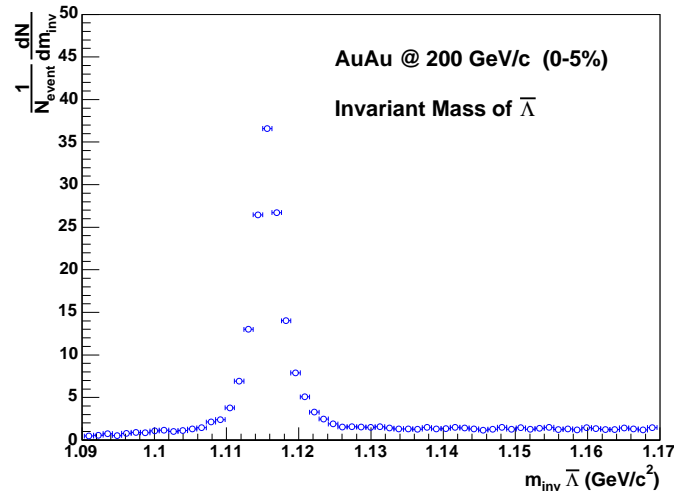
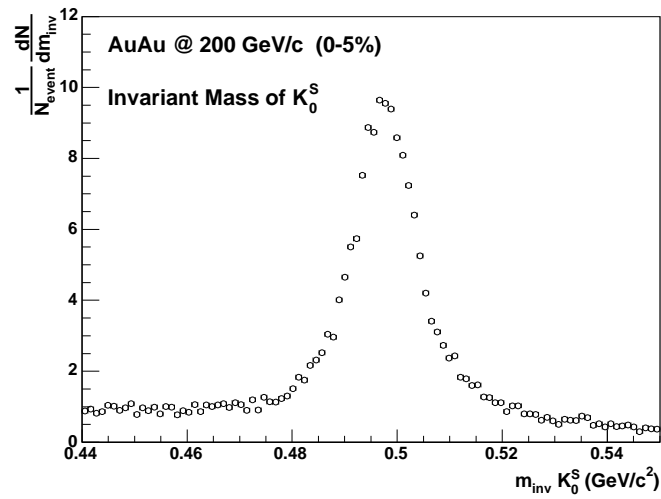
Table 4.6: Cuts $\bar{\Lambda}$ for $AuAu$ collisions @ 200 A GeV

⁷,Decayed length ⁸,Fit points of daughters ⁹DCA of positive daughter ¹⁰,DCA of negative daughter ¹¹ and Mass Λ ¹².

Figures 4.4 4.5 4.6 show the invariant mass peak for Λ $\bar{\Lambda}$, and k_0^S in central collisions, respectively. The high S/B ratio shows the good quality of reconstruction method. Notice that this method does not necessary have any kind of p_T limits for the V0s. One can reach as far as as the statistics allows. Therefore the V0s are good trigger particle candidates for identified jet correlation studies.

Event Vertex	$ Z_{Vertex} < 65$ cm
DCA daughters	< 0.5 cm
Decayed length	> 6.0 cm
Fit points of daughters	> 15
DCA of positive daughter	> 1.5 cm
DCA of negative daughter	> 1.5 cm
Mass $\bar{\Lambda}$	$(0.385 \text{ MeV}/c^2 < m_{\bar{\Lambda}} < 0.405 \text{ MeV}/c^2)$

Table 4.7: Cuts K_0^S for $AuAu$ collisions @ 200 A GeVFigure 4.4: Invariant Mass spectrum for Λ

Figure 4.5: Invariant Mass spectrum for $\bar{\Lambda}$ Figure 4.6: Invariant Mass spectrum for K_0^S

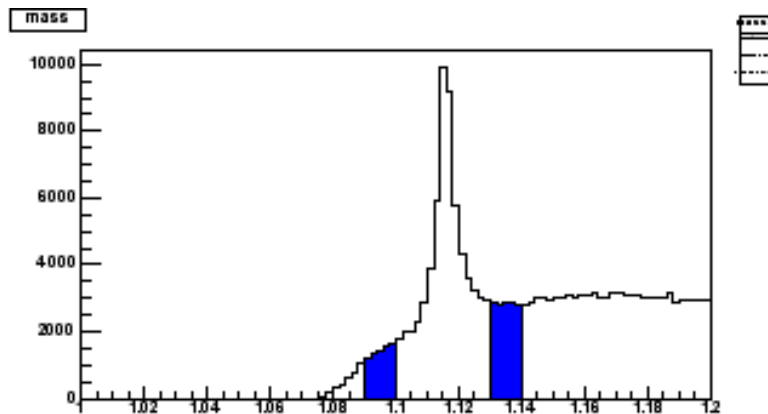


Figure 4.7: misidentified Λ from the side-bin selection

4.2.3 Background of misidentified V0s

The cuts we chose are quite tight requiring $\frac{S}{N} > 14$. In principle, cuts can be optimized to improve the number of V0s by simultaneously increasing some of the background. In jet correlation studies this can be risky, since misidentified V0s can have correlations with the associated particles themselves. By using side-bin candidates (shown in Figure 4.7) from the invariant mass plot, the correlation between associated particles and misidentified Λ can be tested. It has a jet like structure (See Figure 4.8 while for misidentified K_0^s it is rather flat (Figure 4.9). This is caused by the different properties of their decay daughters. Because the mass difference between proton and pion, the proton daughter carries most of the momentum of Λ . Thus the momentum of the reconstructed Λ is mostly determined by its proton "daughter".

⁷Distance between decay daughters at decay vertex.

⁸Distance between primary vertex and decay vertex.

⁹Fit points used for TPC tracking

¹⁰DCA of positive daughter to primary vertex

¹¹DCA of negative daughter to primary vertex

¹²Invariant mass of reconstructed V0

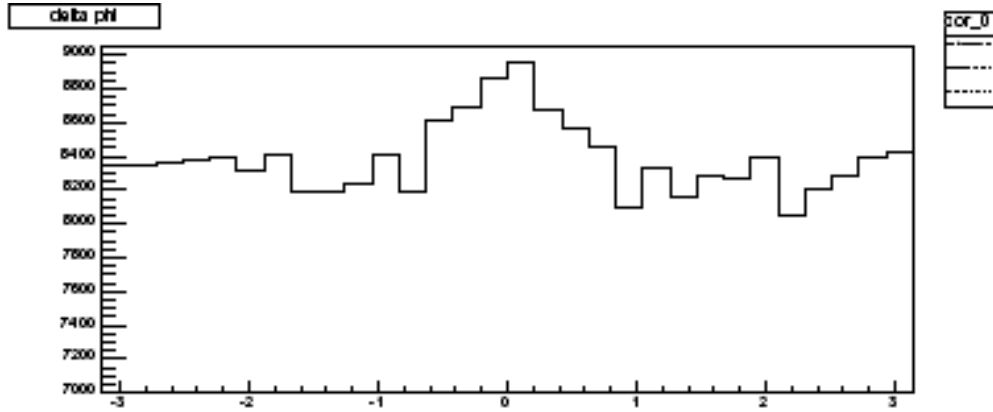


Figure 4.8: Correlation background for misidentified Λ

Primary protons track have their own correlations. Such correlations get passed into the V0 correlations when a proton and a pion forms the misidentified Λ s. For K_0^S the daughters have identical mass therefore the momentum is evenly distributed. Any correlation effect is then diminished because of the large opening angle between the two daughters. In principle, a correction can to be made to the correlation functions for misidentified V0s by using the signal to background ratio and the side-bin correlation. The general relation between the correlation and the background is shown in the following, where S, B represents the real number of V0s and the misidentified V0s.

$$C_{corrected}(\Delta\phi) = \frac{B+S}{S} \left(C_{all}(\Delta\phi) - \frac{B}{B+S} C_{bg}(\Delta\phi) \right)$$

In general this correction need to be done independently for each centrality and p_T bins because their different S/B ratio. Such corrections will also affect the calculation of the inclusive background and flow. To avoid such complexity I have chosen clean V0 samples based on tight cuts. The effects caused by the misidentified V0s are

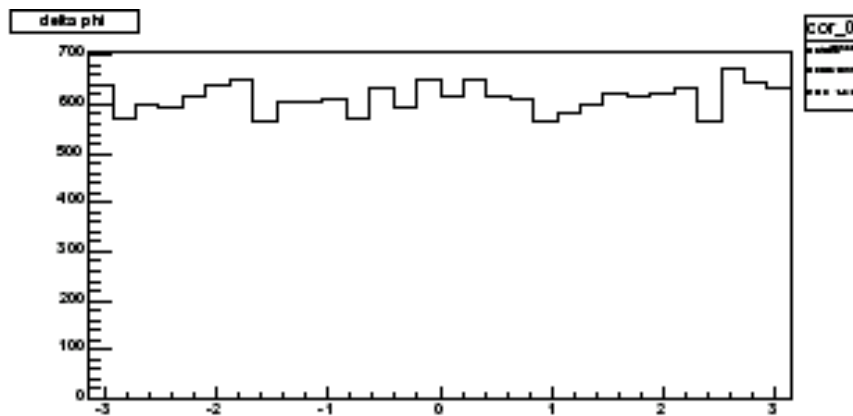


Figure 4.9: Correlation background for misidentified K_0^S

negligible when the S/N exceeds 10.

4.3 Efficiency Correction

Efficiency correction in STAR is complicated because each detector and each piece of the detector requires its own hardware efficiency correction. In addition there are corrections due to the tracking software and the geometric limitation of the detectors. Generally, efficiency is a function of kinematics, centrality, particle species, etc., which make it even more challenging. In the following I will discuss efficiency corrections used by STAR and corrections for this analysis.

4.3.1 Tracking Efficiency

Tracking Efficiency is the probability of reconstructing the track. As we know it can depend on many different things. In STAR a method called "Embedding" has been

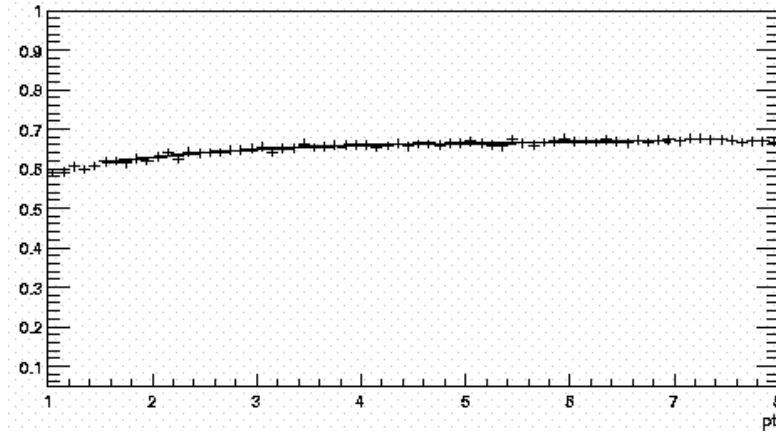


Figure 4.10: Tracking Efficiency as a function of p_T for charged hadrons

adapted to resolve this issue. The idea of this method is to add a simulated signal to the real event. This can easily be achieved software-wise. We can analyze the new event with the added simulated track to see if the track has been correctly reconstructed. The probability of the reconstruction gives us the tracking efficiency. This method combines the Monte Carlo simulation with the real data environment, thus matching exactly the kinematics of the actual event. Fig. 4.10 shows a sample of tracking efficiency as function p_T for central(0–5%) $AuAu$ collisions calculated by using the embedding method. In our data analysis, we are dealing with tracks with high p_T in the mid-rapidity region ($\eta \in (-1.0, 1.0)$) in different centralities. Fortunately the tracking efficiencies from embedding show that for high p_T tracks the efficiency stays almost constant and only slightly drops off when the multiplicity changes or pseudo rapidity changes. The efficiency correction for the correlation studies in this thesis is only applied to the associated particles, which are chosen to always be primary tracks. We are using the code developed by F. Wang[25] which incorporates

embedding efficiency corrections for η , p_T and event multiplicity (centrality). For the trigger particle, since I normalize the correlation function by the number of trigger particles, the efficiency of the trigger particle cancel out. For correlation studies, we also need to consider pair production efficiencies. The efficiency correction of particle pair production can be treated the same as efficiency correction for two single particles. In our case, the efficiency does not change or only change moderately. But there are some geometric effects which need to be treated with care such as the TPC sector boundaries.

4.3.2 TPC sector efficiency correction

Detector TPC has full azimuthal coverage. However it is divided into 12 sectors. There are "dead areas" on the boundary of each sector, which are active in tracking. Such a geometric acceptance limitation will cause the tracking efficiency to drop near the boundary of each sector. Fig. 4.11 (up-left) shows the single particle azimuthal angle distribution. The 12 dips in the ϕ spectrum indicate the positions of dead areas in TPC. Since it will affect both trigger particles and associated particles, the effect on the correlation can be calculated by using a convolution of the single particle distributions. Fig. 4.11 (up-right) shows the convolution result of two single particle $\Delta\phi$ distribution. Apparently the TPC sector pattern also exists in the convoluted spectra. Such pattern are found in the real correlation measurement as shown in Fig. 4.11 (bottom-left). In order to correct I am using the convoluted spectrum, for each bin, an efficiency is calculated by using the convolution value over the average value. After correction, the resultant correlation is rather smooth as shown in Figure. 4.11 (bottom-right). Such corrections need to be done separately for different centrality

bins and different cuts. Presumably, this correction will not change the yield or integrated value of the correlation. In this thesis the correction is applied only for the central collisions, where such effects are large and influential. The TPC sector effects can also be resolved by wisely choosing the $\Delta\phi$ to average out the sector patterns.

4.4 Sample of correlation function

Figures 4.12 and 4.13 show azimuthal correlation functions for unidentified charged hadrons for pp and $AuAu$ collisions. I have chosen a p_T range of $1.5 \text{ GeV}/C < p_T < 3.0 \text{ GeV}/c$ for both trigger and associated particles. For $AuAu$ collisions the centrality bin are chosen to be 0 – 5%, 5 – 10%, 10 – 30%, 30 – 50% and 50 – 70% (from left to right, top to bottom). As one can see, a clear jet-like structure appears on the same side ($\Delta\phi = 0$) for both pp and $AuAu$ collisions. We have fitted the pp correlation with Equation. 3.6.2 and $AuAu$ data with 3.6.5. These figures give us a general impression about the shape of the correlation function and quality of the data and their centrality dependencies. I will come back to the details on the physics discussions in chapter 5. Fig. 4.14 shows a summary plot for the correlation functions as a function of centrality. Again the correlations are fitted with equation 3.6.5. From the quality of these correlation functions, one can certainly conclude that we have the ability to measure the azimuthal correlation function using the STAR detector. The full azimuthal coverage (2π) of the TPC make the detector a very powerful tool to perform such measurements. This ability enable us to study many new interesting physics which might not be detected using single particle spectra.

In the following chapters, I will present our measurement of correlation functions for different identified trigger particle species. Both centrality dependence and p_T

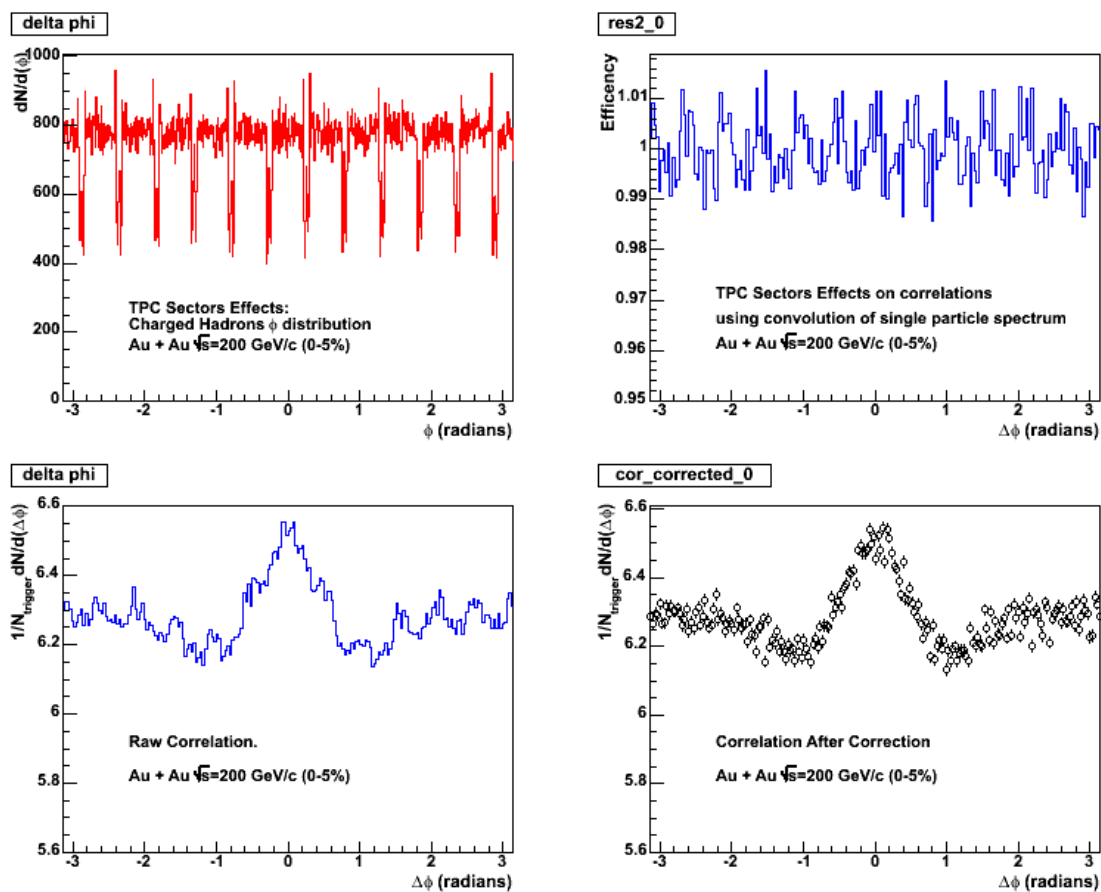
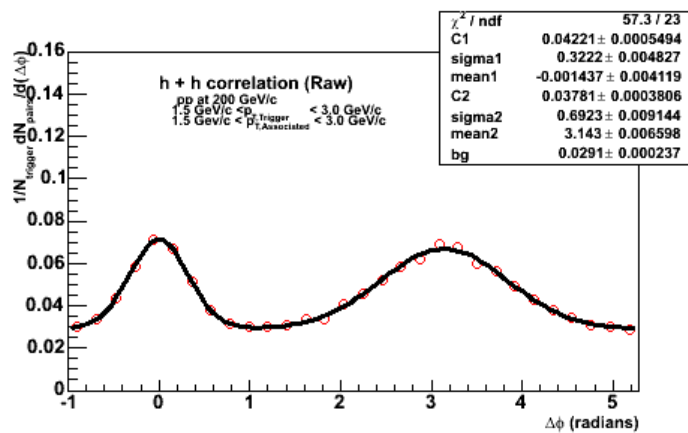
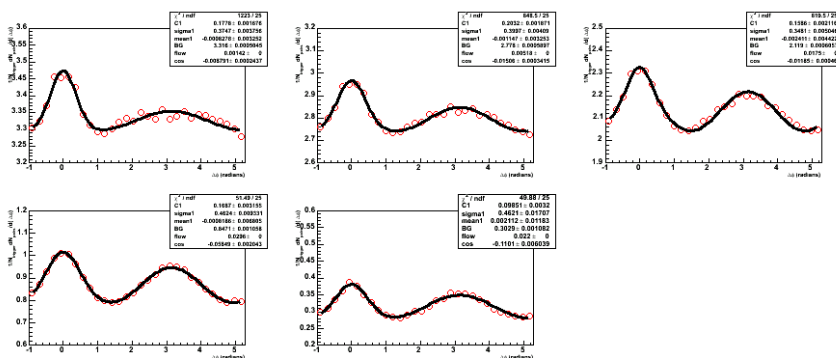


Figure 4.11: Efficiency corrections for TPC sectors

Figure 4.12: Azimuthal correlation for pp collisionsFigure 4.13: Azimuthal correlation for $AuAu$ collisions for different centralities

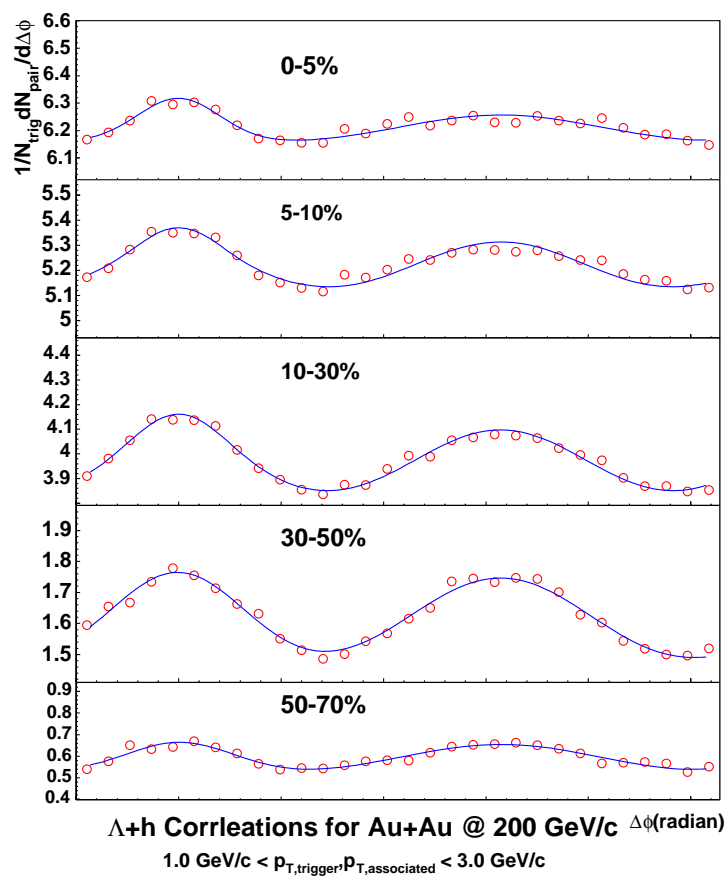


Figure 4.14: Azimuthal correlation for $AuAu$ with Λ as the trigger particle

dependence are presented.

Chapter 5

Azimuthal correlations for identified trigger particles

High p_T correlations of unidentified charged hadrons have been applied to study to jet quenching in central $AuAu$ collisions [25][27][17]. By using this method we are able to retrieve information about medium effects without the full reconstruction of the jet. It has been found that for unidentified charged hadrons in the p_T ranges $4 \text{ GeV}/c < p_T^{trig} < 6 \text{ GeV}/c$ and $2 \text{ GeV}/c < p_T^{asso} < 4 \text{ GeV}/c$ the back side jet correlations are suppressed in central $AuAu$ collisions [27]. Further studies have shown that such suppression leads the transfer of associated particles from a higher p_T state to a lower p_T state [25]. There seems to be a strong medium modification effect: the jet suffers a significant energy loss in the medium. Such an energy loss is in agreement with partonic energy loss inside a medium with high gluon density, such as QGP, according to Wang et al.[34][35]. However there are more questions to be asked regarding medium effects. Does the fragmentation get modified inside the medium? How does the energy of the back side jet get redistributed? Is there another hadron production mechanism that contributes to the jet-like correlation? Are there flavor dependent effects? In order to answer these questions, additional information such as identified

particle correlations is needed. Measurements of the nuclear modification factors R_{AA} and R_{CP} for different particle species have shown that the suppression at high p_T has a very different p_T dependence for meson and baryons [36] [37]. While the mesons are suppressed at relatively intermediate p_T range (1.5-2.0 GeV/c), the baryons extend further into the higher p_T range (3 - 4 GeV/c) without experiencing strong suppression. This led to the theory of possible different hadron production mechanisms, such as parton recombination [38] [13] [39] instead of jet fragmentation in the intermediate p_T range. In this chapter I will go to present two particle correlations with strange baryons ($\Lambda, \bar{\Lambda}$) and meson (K_0^S) as trigger particles and unidentified charge hadrons as associated particles in $AuAu$ collisions. The correlations are studied as a function of centrality and trigger particle species using different p_T cut sets. In comparison, unidentified charged hadron correlations are also presented.

5.1 Correlation functions with Λ , $\bar{\Lambda}$ and K_0^S as trigger particles

Figure 5.1 and 5.2 show the azimuthal correlation functions with a Λ trigger particle in $AuAu$ collisions as a function of centrality. I have chosen the p_T ranges for trigger and associated particle to be between 1.5 GeV/c and 3.0 GeV/c. I have fitted the correlation function with different methods described by Equations 3.6.2 and as shown in 3.6.3 shown in Figures 5.1 and 5.2 respectively. As we can see from the plots, both methods fit the curve equally well. For reference, we have also measured the correlation in pp using the same cuts. (see Figure 5.3).

Parameters are retrieved from these fits for comparison. The same side and back side

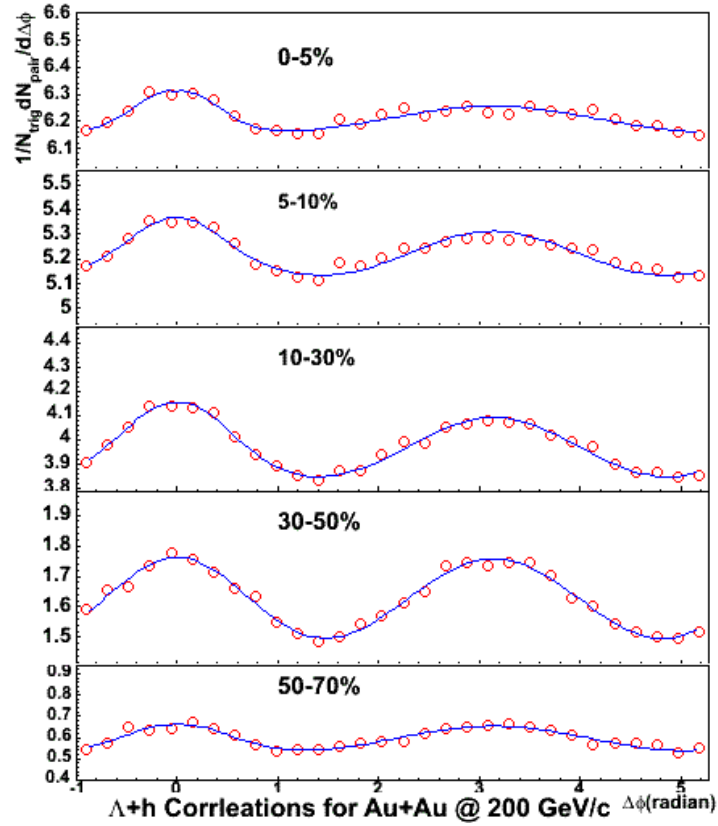


Figure 5.1: Azimuthal correlation for $AuAu$ for different collision centrality with Λ as the trigger particle and unidentified charged hadrons as the associated particles. A Gaussian like back side are chosen to fit the back side

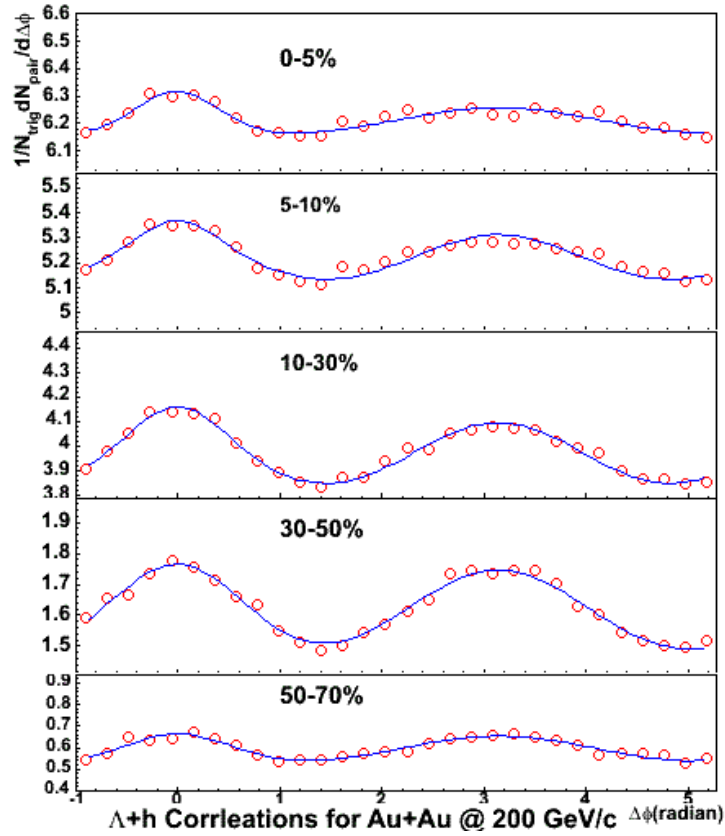


Figure 5.2: Azimuthal correlation for $AuAu$ for different collision centrality with Λ as the trigger particle and unidentified charged hadrons as the associated particles. A cosine term was chosen to fit the back side.

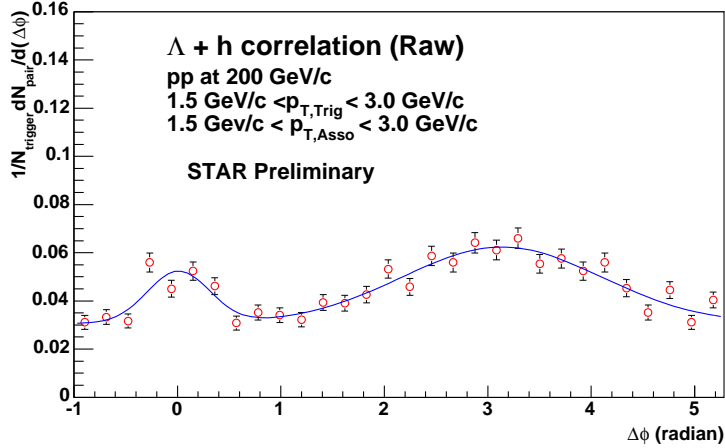


Figure 5.3: Azimuthal correlation for pp . We choose trigger particle to be Λ and associated particle to be unidentified charged hadrons.

associated particle yields per trigger are calculated by using the retrieved parameters. For $AuAu$ collisions five different centrality classes have been analyzed (0 – 5%, 5 – 10%, 10 – 30%, 30 – 50% and 50 – 70%). The elliptic flow parameters were extracted from the published data for charged hadrons and strange particles [40][19][41].¹ The magnitude of the uncorrelated background are calculated by using the convolution of the inclusive single particle spectra of the trigger and associated particles described in the chapter 3. The centralities are scaled to the number of participants for nucleus-nucleus collisions based on the Glauber model calculation [40].

Table 5.1 lists the calculated uncorrelated background and effective elliptic flow

¹ v_2 The effective v_2 is calculated by using the convolution of v_2 of trigger and associated particle within their p_T range using the method described in chapter 3. Numeric values are extracted from fitting of the published data.

<i>centrality</i> (%)	N_{part}	$BG_{calculated}$	v_2^{eff}	BG_{fit}
0 – 5	352(5)	6.177	0.00134	6.193(0.001)
5 – 10	298(10)	5.192	0.00696	5.209(0.001)
10 – 30	210(16)	3.927	0.0122	3.950(0.0034)
30 – 50	105(16)	1.575	0.0232	1.579(0.004)
50 – 70	35(11)	0.554	0.0202	0.574(0.005)

Table 5.1: Uncorrelated background for Λ + charge hadron correlations at 1.5 GeV/c < p_T^{trig}, p_T^{asso} < 3.0 GeV/c.

component v_2^{eff} (defined in 3.5.6 and 3.5.7) for the correlation function. These values are then compared to the background value extrapolated from the fits. There are in good agreement (see Figure 5.4). Although the difference between the fitted background and the background from calculation is small, it could cause a significant effect on retrieving the jet correlation because the magnitude of the jet correlation is also small compared to the uncorrelated background.

From the parameters retrieved from the fits, we can calculate the area of the Gaussian to obtain the same side and back side associated particle yields. In Figure 5.5 and 5.6 I show the widths of same side (open circle) and back side (open cross) as a function of participants for two different p_T cut sets. For the same side correlations, the width shows a weak increase from peripheral collisions to central collisions. Generally the magnitude is comparable to the width measured in p+p system. For the back side correlation, the width increases dramatically especially for the most central collisions where the back side width exceeds $\pi/2$. This clearly shows the collapse of the jet structure, a simple Gaussian fit with the simple picture of k_T broadening, is suitable to explain the back side correlation in central collisions. This is in agreement with previous unidentified charged hadron measurements which show the strong

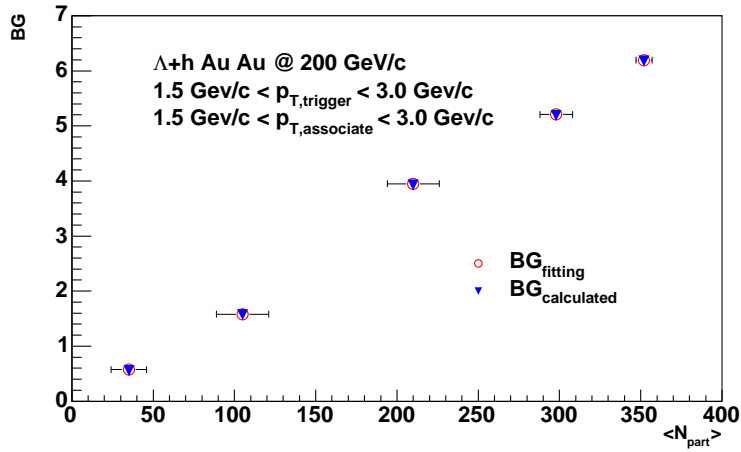


Figure 5.4: Background parameter from fitting and calculation from the inclusive spectrum convolution.

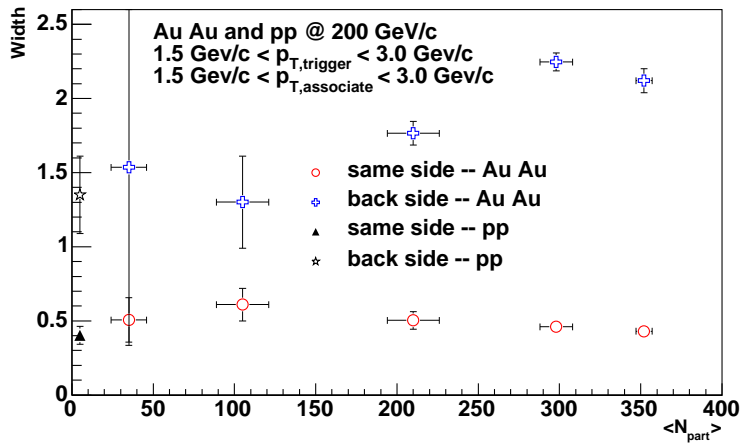


Figure 5.5: Width of the same side and the back side as the function of participants with $1.5 \text{ GeV}/c < p_T^{trig}, p_T^{asso} < 3.0 \text{ GeV}/c$

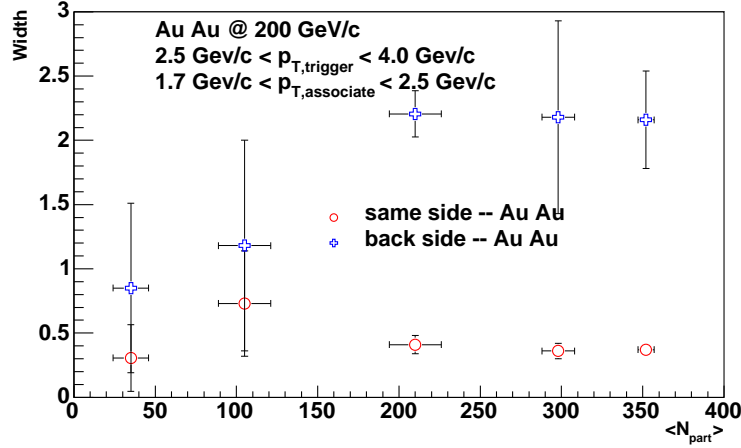


Figure 5.6: Width of the same side and the back side as the function of participants with $2.5 \text{ GeV}/c < p_T^{\text{trig}} < 4.0 \text{ GeV}/c$ $1.7 \text{ GeV}/c < p_T^{\text{asso}} < 2.5 \text{ GeV}/c$

suppression of the back side jet structure in the central $AuAu$ collisions for high p_T particles[17]. Due to the conservation of the transverse momentum of the quenched parton, a statistical cosine term can be applied to fit the back side correlations in central collisions as an alternative to the simple Gaussian fit (Equation 3.6.2 3.6.3), Such a term can be further analyzed to retrieve the total number of the particles that carry part of the momentum . Thus we can gain additional information about the redistribution of the transverse energy of the quenched parton inside the medium. I will come back to the discussion of the momentum balance cosine term in the chapter 6. In Figures 5.7 5.8 and 5.9 I show the raw correlation function measured for different particle species. For central $AuAu$ collisions they all show the same feature on the back side, a very broadened distribution which is in agreement with a wide cosine distribution. This shows that the collapse of the back side correlation in central

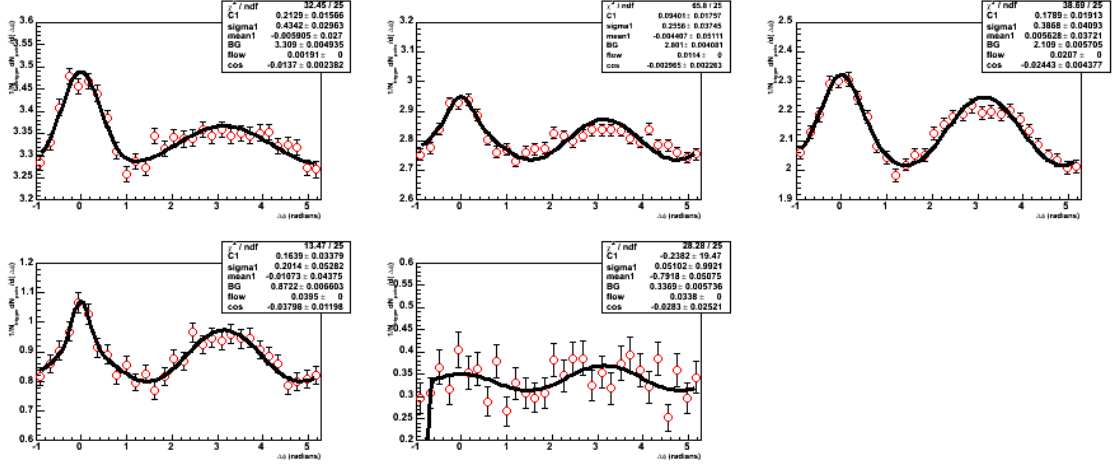


Figure 5.7: $\bar{\Lambda} + h$ correlation functions for different centralities. $2.5 \text{ GeV}/c < p_T^{\text{trig}} < 4.0 \text{ GeV}/c$ $1.7 \text{ GeV}/c < p_T^{\text{asso}} < 2.5 \text{ GeV}/c$

collisions is independent of the trigger particle species. The medium effects on the back correlations are strong and the jet structure is "destroyed".

5.2 Associated particle yield for same side and back side

Figure 5.10 and 5.11 show the same side and back side associated particle yields retrieved for different particle species as the function of the centrality in $Au + Au$

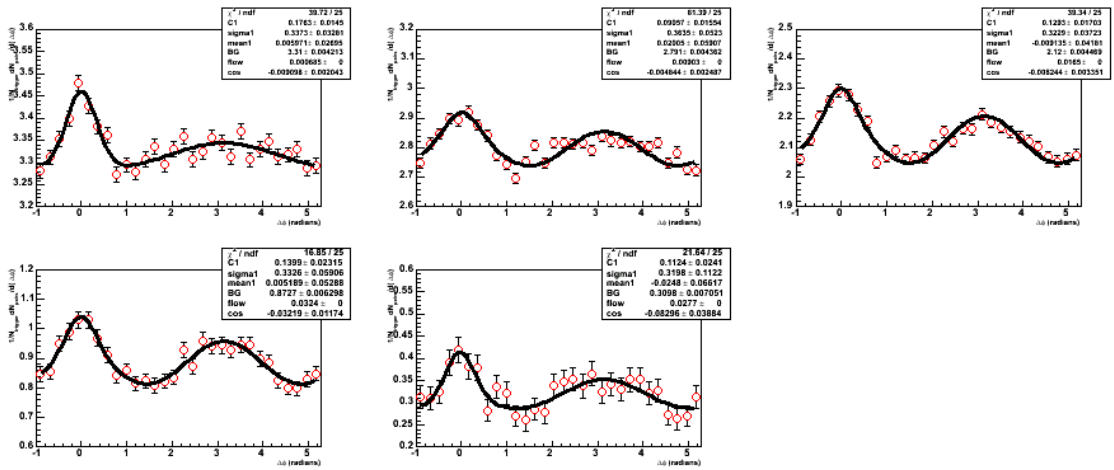


Figure 5.8: $K_0^S + h$ correlation functions for different centralities. $2.5 \text{ GeV}/c < p_T^{\text{trig}} < 4.0 \text{ GeV}/c$, $1.7 \text{ GeV}/c < p_T^{\text{asso}} < 2.5 \text{ GeV}/c$

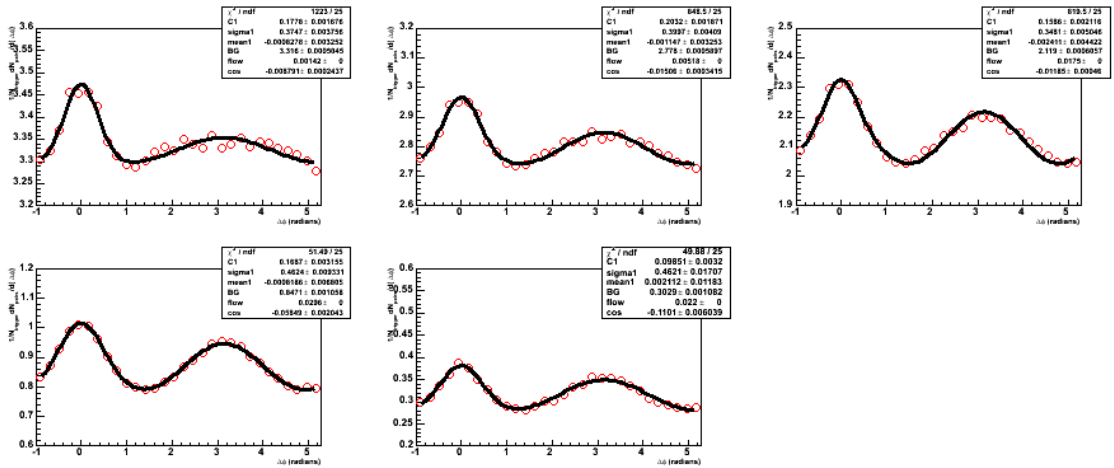


Figure 5.9: h + h correlation functions for different centralities. $2.5 \text{ GeV}/c < p_T^{\text{trig}} < 4.0 \text{ GeV}/c$ $1.7 \text{ GeV}/c < p_T^{\text{asso}} < 2.5 \text{ GeV}/c$

collisions ². All different trigger particle species show a similar trends, i.e. a rising from central to mid central collisions and a drop towards peripheral collisions. Yields for different particle species are slightly different. We notice that the away side trends are very different from what have seen for I_{AA} at higher p_T [41] . Is it because of the different p_T range or something else? If our measurements are correct than we need to answer the question, why would a different p_T range change the results so much. Let's keep that question in mind and look at some of the other facts we can learn from the correlation function. By looking at the raw correlations for $AuAu$ and pp we instantly notice that the magnitude is very different. Correlations in $AuAu$ have much larger magnitude than pp . If we form the $AuAu$ to pp ratio for the same side yield, the number is much larger (6.0) than unity. To try to understand this result we need to revisit our definition of the correlation function in equation 3.1.1. The same side yield of the correlation should be proportional to the di-hadron production in a jet divided by the trigger-hadron production. The back side yield of the correlation should be proportional to single-hadron production in a jet divided by the trigger-hadron production.

$$\begin{aligned}
N_{same}(p_T^{trig}) &= \varepsilon_{same} \frac{P_2(p_T^{asso}, p_T^{trig})}{P_1(p_T^{trig})} \\
N_{back}(p_T^{trig}) &= \varepsilon_{back} \frac{P_1(p_T^{asso})}{P_1(p_T^{trig})} \\
\frac{N_{back}}{N_{same}} &= \varepsilon \frac{P_2(p_T^{asso}, p_T^{trig})}{P_1(p_T^{trig})}; \quad \varepsilon = \frac{\varepsilon_{back}}{\varepsilon_{same}}
\end{aligned} \tag{5.2.1}$$

²Yields are calculated by integrating the fitted Gaussian.

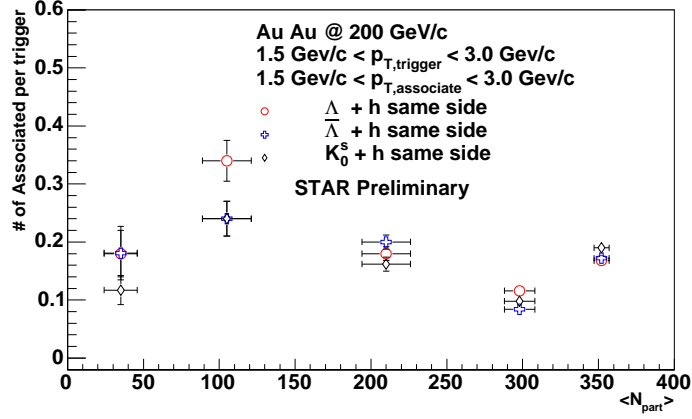


Figure 5.10: Same side yields of associated particles for different trigger species as a functions of participants for $1.5 \text{ GeV}/c < p_T^{trig} < 3.0 \text{ GeV}/c$ $1.5 \text{ GeV}/c < p_T^{asso} < 3.0 \text{ GeV}/c$

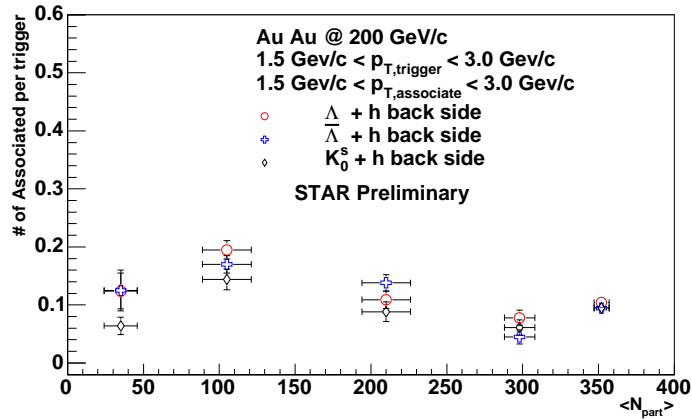


Figure 5.11: Back side yields of associated particles for different trigger species as a functions of participants for $1.5 \text{ GeV}/c < p_T^{trig} < 3.0 \text{ GeV}/c$ $1.5 \text{ GeV}/c < p_T^{asso} < 3.0 \text{ GeV}/c$

In Equation 5.2.1 we represent the same side and back side yields of the jet correlation by N_{same} and N_{back} respectively. We are using $P_1(p_T)$ to represent the single-hadron probability in the jet and $P_2(p_{T,1}, p_{T,2})$ to represent the di-hadron production of the jet. Generally, because the probability of having a jet correlation when there is a trigger particle is less than 1, we are using ε_{same} to represent the probability of having a same side jet in the presence of the trigger particle and ε_{back} to represent the probability to have a back side jet. It is easy to deduce that the back side to same side ratio is proportional to ε . For pp collisions, when $\varepsilon \sim 1.0$, this ratio is a function of trigger particle p_T and associated particle p_T , and is generally greater than 1.0. This is consistent with our observation of Λ -charged hadron correlations for p+p collisions. For the central Au+Au collisions, the medium effect causes a decrease of ε , and therefore leads to the suppression of back side jet correlations. In general, when we compare the same side correlation for $AuAu$ and pp , the increase should not be due to the enhancement of the thermal background, but rather to the increase of the jet-like di-hadron production per jet, which could be either the medium modification of the jet fragmentation such as the "trigger-bias" effect (see details in chapter 7) or another correlated particle production mechanism, even on the same side [42][43]. On the other hand the lack of strong differences in the correlations for different trigger particle species shows that in this p_T range, ε_{same} and ε_{back} are not very sensitive to the particle species. In the framework of a simple thermalized parton recombination model [38][12] one would expect a decrease of ε from collisions to central collisions since hadrons created by thermal partons should not be correlated. This should cause a weakening of the correlation function as a function of centrality, in particular for baryons which seem to be enhanced in the intermediate p_T range due to the parton

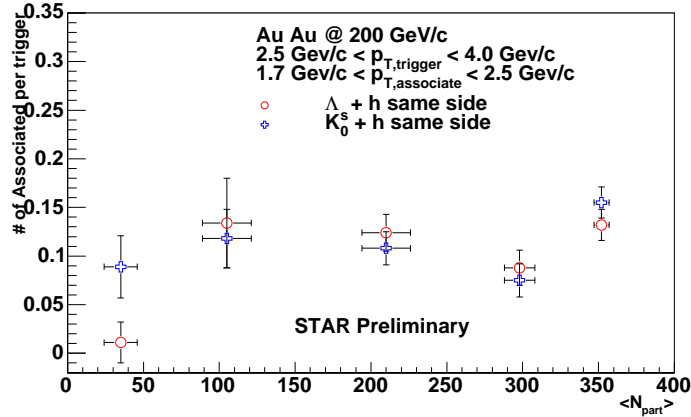


Figure 5.12: Same side yields of associated particles with Λ and K_0^S as trigger particles. $2.5 \text{ GeV}/c < p_T^{trig} < 4.0 \text{ GeV}/c$ $1.7 \text{ GeV}/c < p_T^{asso} < 2.5 \text{ GeV}/c$

coalescence[27]. We have not seen such effects in our correlation measurements.

Figure ?? and ?? show the same side and back side associated particle yield for a different cut on the transverse momentum of the trigger and associated particle. ($2.5 \text{ GeV}/c < p_T^{trig} < 4.0 \text{ GeV}/c$ $1.7 \text{ GeV}/c < p_T^{asso} < 2.5 \text{ GeV}/c$) Our results are comparable to similar measurements by PHENIX using baryons and meson as leading particles[27]. There is no significant difference between baryon trigger and meson trigger as a function of centrality except perhaps for the most central bin.

5.3 Asymmetry of the correlation – the Difference Function and discussions

In chapter 3 we have given a definition (Equation 3.6.6) of the difference function. It can measure the asymmetry of the correlation function without requiring a good

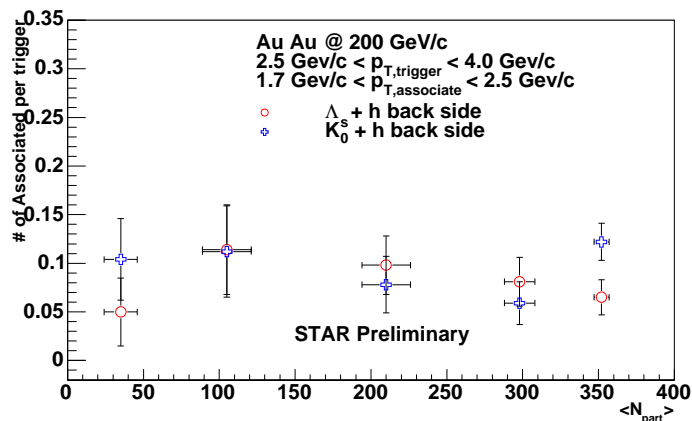


Figure 5.13: Back side yields of associated particles with Λ and K_0^S as trigger particles. $2.5 \text{ GeV}/c < p_T^{\text{trig}} < 4.0 \text{ GeV}/c$ $1.7 \text{ GeV}/c < p_T^{\text{asso}} < 2.5 \text{ GeV}/c$

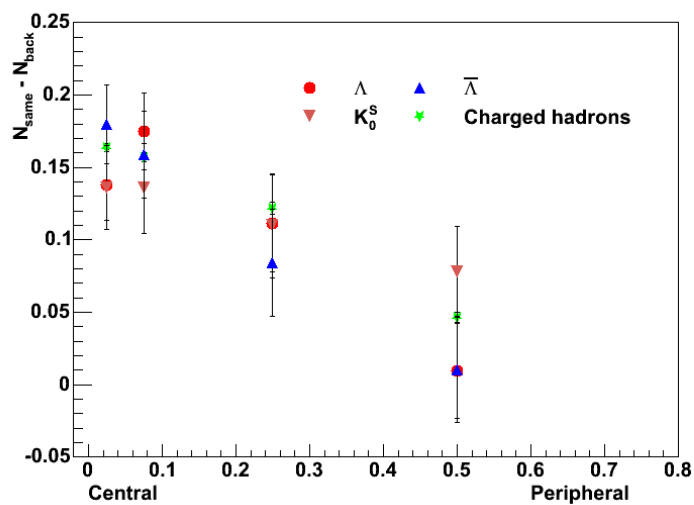


Figure 5.14: Difference function for different trigger species as function of centrality. $2.5 \text{ GeV}/c < p_T^{\text{asso}} < p_T^{\text{trig}} < 10.0 \text{ GeV}/c$

knowledge of background and flow. Due to the quenching of the back side, the difference function should reach largest the largest value in most central collision and decrease towards peripheral collisions. Figure 5.14 shows the difference function as a function of centrality for different trigger particle species. Both trigger and associated particle are above $2.5 \text{ GeV}/c$ with $p_T^{trig} > p_T^{asso}$. The centrality dependence of the difference function is in agreement with the jet quenching scenario for all different trigger particle species. However we can only deduce the relative asymmetry of the same side and back side peaks in the central collisions. In order to learn the behavior of the correlation on each side, I introduced the Differential Difference Function (Equation 3.6.7). In Figure 5.15 I show the correlation same side (open circle) and back side (open diamond) for different centralities. The DDF (Differential Difference Function) is nothing else but the difference of same side and back side as a function of $\Delta\phi$. As we have pointed out in chapter 3, the DDF generally preserves the information of the shape of the same side and back side together with their amplitude. Figure 5.16 shows the DDF for $h + h$ correlations in the intermediate p_T range.

In Figure 5.16, the dips to values less than zero represent the regions where back side correlations exceed the same side. I fit the curves with Equation 3.6.9. The yields we retrieve are in agreement with direct background subtraction methods within error bar. However, the fits seem to depend on the shape of the back side. The fits are very sensitive to the dips close to the boundary ($\Delta\phi = \pi/2$). Although further studies are required to make the fits more stable, we can still deduce some general information. Figure 5.16 indicates a decreasing trend in the amplitude to asymmetry of correlation functions in this p_T range. There are two possibilities to create this effect. First, it is possible that we have a decreasing trend from central to peripheral

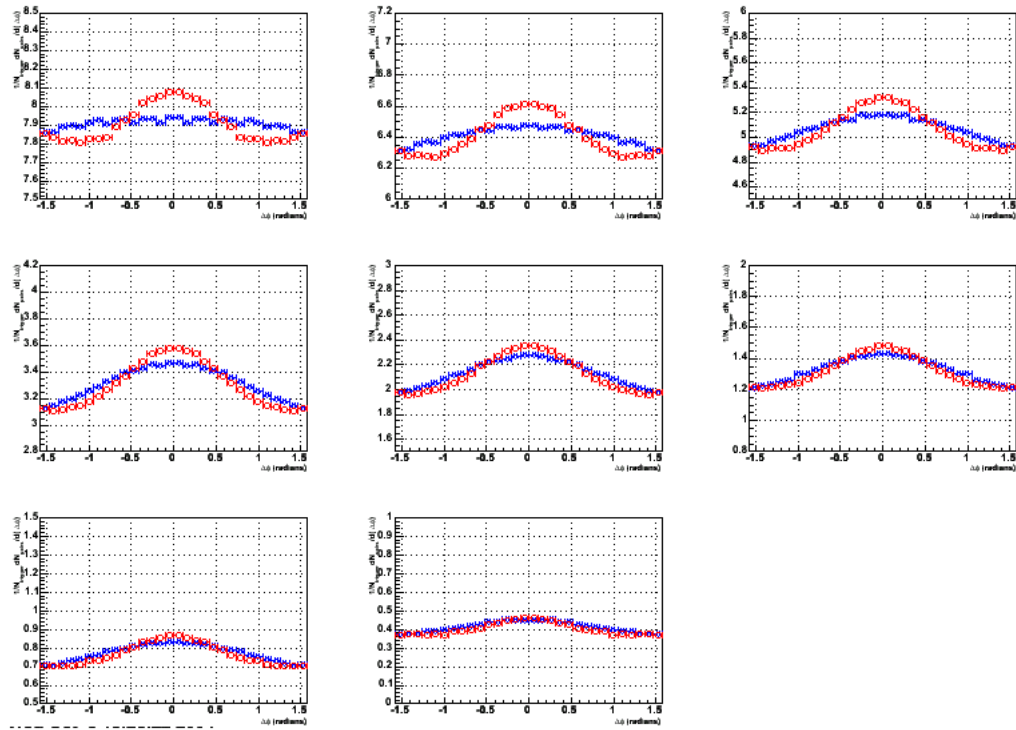


Figure 5.15: Same side (red open circle) and back side of azimuthal correlations for $h + h$ correlation for different centralities. $1.5 \text{ GeV}/c < p_T^{asso}, p_T^{trig} < 3.0 \text{ GeV}/c$

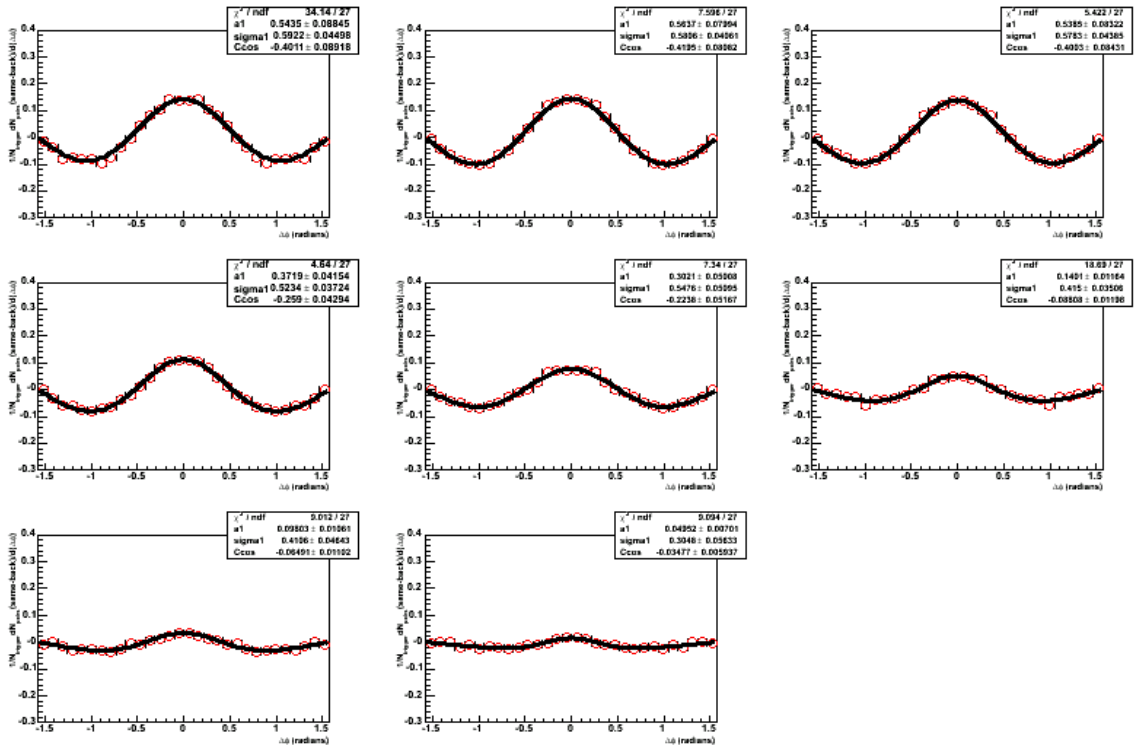


Figure 5.16: DDF (Differential Difference Function) for unidentified charged hadrons with $1.5 \text{ GeV}/c < p_T^{asso}, p_T^{trig} < 3.0 \text{ GeV}/c$ Centrality dependence indicate non-jet like contributions.

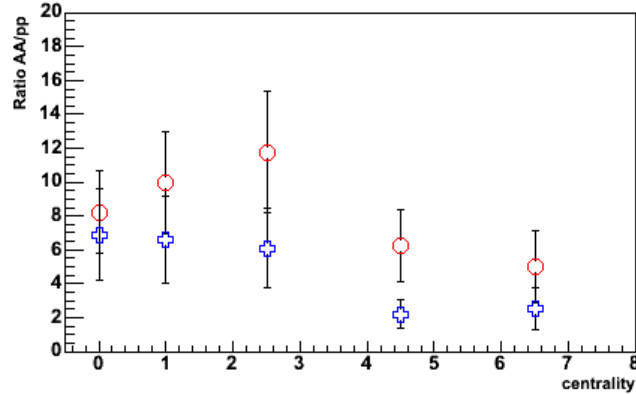


Figure 5.17: AA/pp ratio for $\lambda+h$ correlations for different centralities. ($1.5 \text{ GeV}/c < p_T^{asso}, p_T^{trig} < 3.0 \text{ GeV}/c$)

for both same side and back side. Second, same side and back side both increases but the asymmetry decreases. However, the second scenario does not seem to match the shape of DDF in the peripheral collisions since negative dips of the DDF should increase for peripheral collisions due to the increases of the back side. It seems indicated a new mechanism other than jet fragmentation also making major contribution to the same side correlation in the intermediate p_T range.

5.4 $AuAu$ to pp ratio in central collisions

For Jet correlation at a fixed collision energy, the multiplicity within the jet cone should be constant, independent of the collision system. Thus, one would expect the same side associated particle yield per trigger should be the same in AA and pp collisions. From the previous section, we have learned that for the intermediate p_T

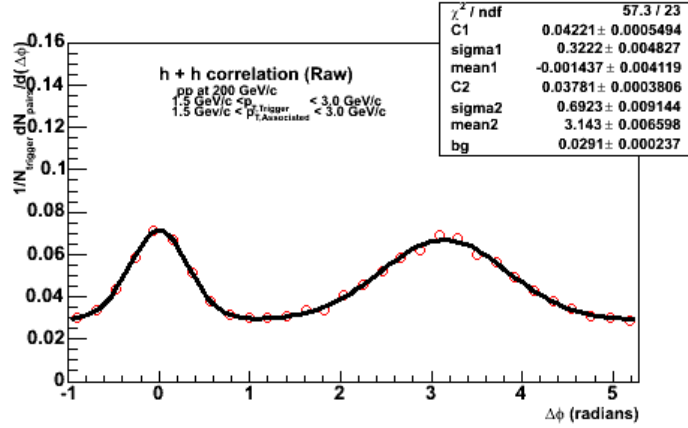


Figure 5.18: $h + h$ correlations for pp collisions $1.5 \text{ GeV}/c < p_T^{asso}, p_T^{trig} < 3.0 \text{ GeV}/c$

range, the same side correlations show a large $AuAu$ to pp ratio for central collisions. Figure 5.17 shows the AA/pp ratio of Λ and charged hadron correlations for different centralities. Despite the large error bars, the ratio approaches six in the central collisions. Such effect does not only exist for the Λ -triggered correlations, all other particle species show similar effects. Figure 5.18 and 5.9(top left panel) show correlations with charged hadrons as leading particles for $AuAu$ and pp . It is apparent that the amplitude of the same side in $AuAu$ (~ 0.2)central is several times larger than pp (~ 0.04). In the following I will discuss different possible scenarios that could cause such an effect.

- Scenario 1: **Medium modification of the fragmentation function**

This can be understood as a quenching effect on the same side correlations. Generally high p_T trigger particles are created from surface emission. However some could also be created from some distance inside the medium therefore

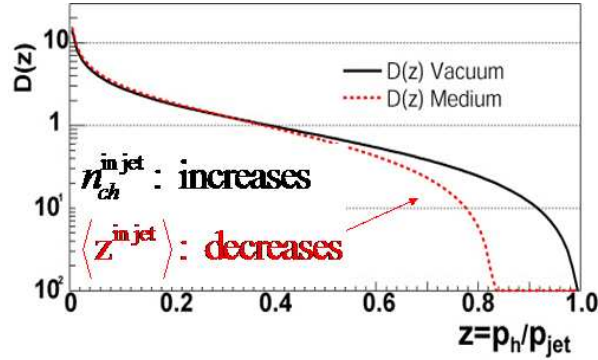


Figure 5.19: Theoretical calculation (by Gyulassy) of the modification of the fragmentation function inside the medium.

experience quenching effects. Figure 5.19 shows a theoretical calculation of the medium modified fragmentation function $D(Z)$ [44]. We can see that due to the effect of the medium, $D(Z)$ becomes more and more softer. Particles with a high fractional momentum (Z) are quenched, i.e. they lose energy and part of this energy materializes as additional low (Z) particles. The integral of both curves is the same. Compared to pp , because the overall production of high p_T trigger particles is reduced, we obtain a larger same side yield which can be expressed as the ratio of associated particles to the trigger particles. This argument explains the large AA/pp ratio and associated particle distribution within the fragmentation context. More lower p_T particles are created by collinear gluon radiation to compensate the quenched energy and momentum. Other arguments such as the "trigger bias" effect of di-hadron production [43] are based on the similar effects. However this model has difficulty to explain trigger p_T scaling of the same side yield. ³

³see chapter 7 for details

- **Scenario 2: Classic Thermal Quark Recombination**

Measurements of constituent quark scaling of the elliptic flow v_2 [ref 1,2] for $AuAu$ collisions suggest a different hadron production mechanism – quark recombination. For the intermediate p_T range, quark recombination is assumed to surpass the hard processes and create intermediate p_T particles more efficiently (see Figure ??).

However if the quarks are from the bulk with random orientation, it should not contribute to the same side correlation due to its randomness. In fact the over produced trigger particle ,if they are random, will dilute the correlation function since the correlation function is normalized by the trigger particle multiplicity. However recently [45] [12] a new parton recombination model developed by Rudolph Hwa et. al. seems solving this difficulty by allowing the thermal parton recombine with the shower parton in at intermediate p_T . We will discuss this in details in chapter 7.

- **Scenario 3: Medium induced gluon radiation and sideways flow effect**

In central $AuAu$ collisions, due to the presence of the medium, the enhanced gluon radiation could increase the same side yield ($D(Z)$) increased in the low Z region in Figure5.19). Could this be causing the large of AA/pp ratio? Further more theorist predicted that medium effects such as direct flow [46] could also affect the shape of the jet cone. However it is hard to believe that these could be causing the large AA/pp ratio due to energy and momentum conservation. In order to generate a large AA/pp , additional energy MUST be added into the jet cone. Where did these energy coming from? This point will also be addressed in chapter 7.

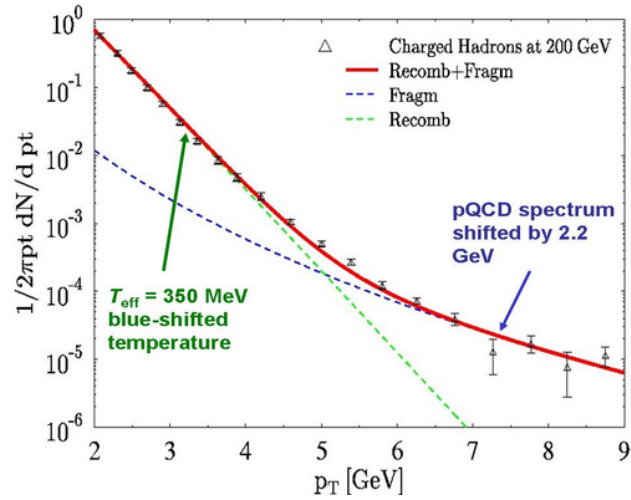


Figure 5.20: Charged hadron production(PHENIX) compared to model calculations. In the intermediate p_T range, recombination dominates hadron production.

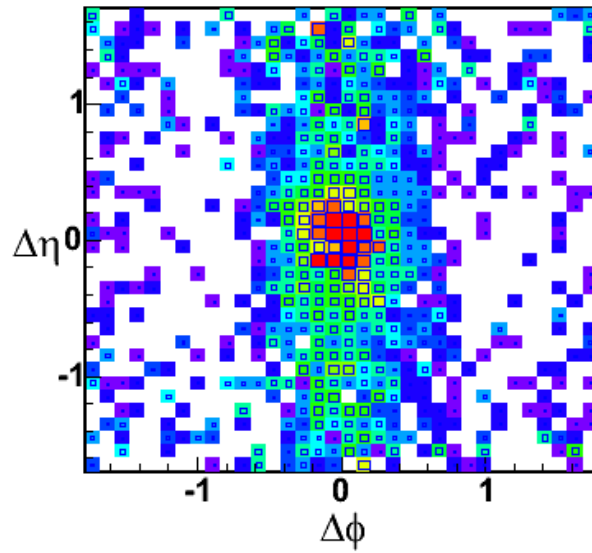


Figure 5.21: 2D jet correlations for $AuAu$ collisions. A very obvious spread out of the correlation in $\Delta\eta$ on same side($\Delta\phi \sim 0$) can be seen (D. Majestro[47])

- Scenario 4: **Dynamic effects of Nuclear collisions**

2D correlation studies in STAR using charged hadrons [25] show an elongation of jet correlations in $\Delta\eta$ for central $AuAu$ collisions (see Figure. 5.21) compared to dAu (Figure ??). Such an effect can be explained as the shifting of the center of mass of hard scattering partons off the lab frame. Because of the high collision energy, small fraction of difference in longitudinal momentum of the two initial incoming partons can cause the center of mass frame shifted in η . Statistically, the correlation measured distribution of the shift. However the integrated same side yield for associated particles per trigger should remain unchanged, since this effect should not change the multiplicity within the same side jet cone. In order to produce the large multiplicity in AuAu collisions, a different (other than jet fragmentation) mechanism is necessary to "inject" more energy into the jet cone. Radial Flow has been suggested by Sergei Voloshin et al. to explain the enhanced correlation spread out in $\Delta\eta$ [48] [49] Similar to the elliptic flow, radial flow is generated by the gradient difference of radial pressure. In a simple minded picture such radial pressure difference can be generated by the radial distribution of the initial collision particle densities. For an azimuthal isentropic particle production in pp, boosting effects of the radial flow can cause the isentropic particle production correlated in same side in $\Delta\phi$ (see Figure 5.22) in the lab frame. Longitudinal coherent radial flow will cause the correlation in $\Delta\eta$. However for high p_T particles, to form such a boost the transverse momentum kick from a large radial expansion has to be significant which will require a large gradient in the pressure. It is still not clear if such a large pressure gradient can be formed stably along different 2 unit of

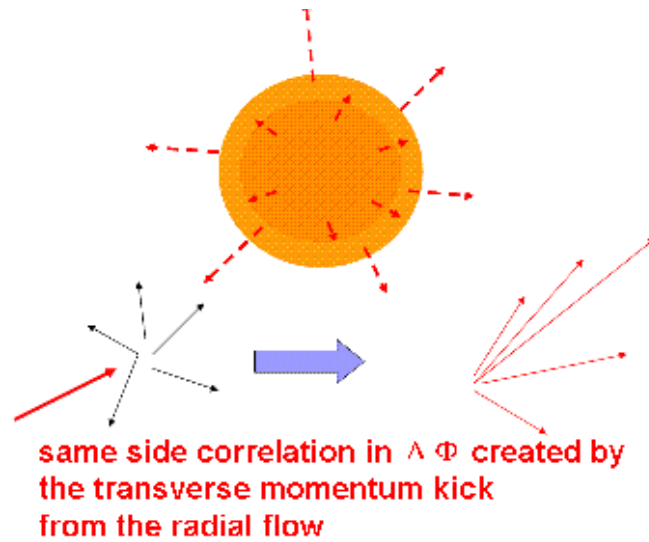


Figure 5.22: Jet-like same side correlation introduced by the the transverse momentum kick.

rapidity since in general thermalization will destroy the long range correlation in η . On the other hand, the same boosting effect could be also generated through the multiple collisions. The nucleon could receive a transverse momentum kick from these initial collisions. The final hard collision is then boosted in transverse direction by the initial kicks and then forms a correlated azimuthal cone. The $\Delta\eta$ spread could be due to the shift of the center of mass to the lab frame longitudinally.

As we can see, for *AuAu* collisions, The system itself will be complicated. What we identified as jet-correlations might incorporate other feature that can be modified in presence of the medium. In addition, hadron production mechanism itself could be different. In chapter 7 I will further discuss this topic in the context of a shower

parton recombination model.

Chapter 6

Back side correlations in central $AuAu$ collisions

In $AuAu$ collisions, back to back correlations carry information about the medium since they need to travel a long distance within the medium and therefore experience more interactions. In central $AuAu$ collisions, high p_T correlations on the back side are quenched, however for at low p_T , a significant amount of the back side associated yield has been recovered using an over-broadened distribution. The origin of all these associated particles is still unclear. Whether they are the remnants of the fragmentation of the quenched parton[46], or some exotic feature,like Sonic Mach wave[50], or just simply due to the conservation of momentum needs to be interpreted. In this chapter, we are going to study the back side jet correlation in central $AuAu$ collisions using the concept of momentum conservation.

6.1 Introduction

Momentum conservation in heavy ion physics can introduced many particle correlations in transverse momentum space. Such kind of correlations were first discussed

in detail by Borghini et al [28] for the correction of measurements for elliptic flow in two particle correlations. The details of particle correlations from momentum conservation are described in Appendix B. The correlation described by Equation B.0.7 should exist for all two particle azimuthal correlations including the high p_T trigger jet correlations. Correlation from momentum conservation in two particle correlations yields a first order harmonic with negative sign. In jet azimuthal correlations it shows a bump on the back side of the jet to balance the momentum of the trigger. One of the interesting features of such a correlation is that it provides us with information about the number of particles necessary to conserve the momentum. In the following section of this chapter, I will study the momentum conservation term for two particle jet azimuthal correlation in detail. I will also try to retrieve N .

6.2 Back side fit for jet correlations based on momentum balance

In Figure 6.1 I show the back side fit using momentum conservation for trigger particles in different p_T ranges for the most central $AuAu$ collisions. We notice that such a term is negative in magnitude which is in agreement with our derivation in the last chapter. The term is also very small since for central collisions it is suppressed by the $1/N$ factor from the large total multiplicities. Figure 6.2 shows the magnitude of the momentum conservation term as a function of trigger p_T . The different lines show different calculations based on Equation B.0.7 for different N . In our calculations, we use the mean transverse momentum from the single particle

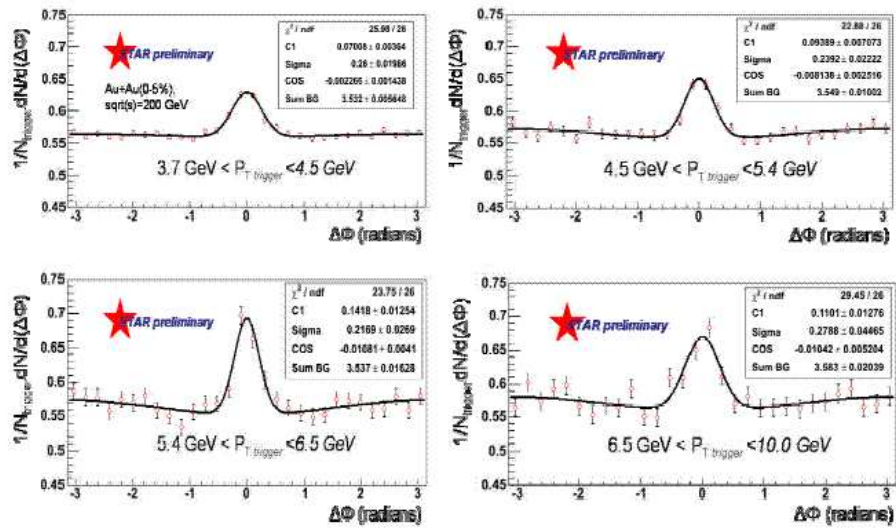


Figure 6.1: Momentum conservation fit for $h+h$ correlations for different trigger p_T ranges in central (5%) AuAu Collisions. The cut for associated particles was chosen as $2.5 \text{ GeV}/c < p_T^{\text{asso}} < 3.7 \text{ GeV}/c$ to reduced the uncorrelated background. Opposite to the leading trigger particle, the small wide rise on the back side are fitted with momentum conservation term.

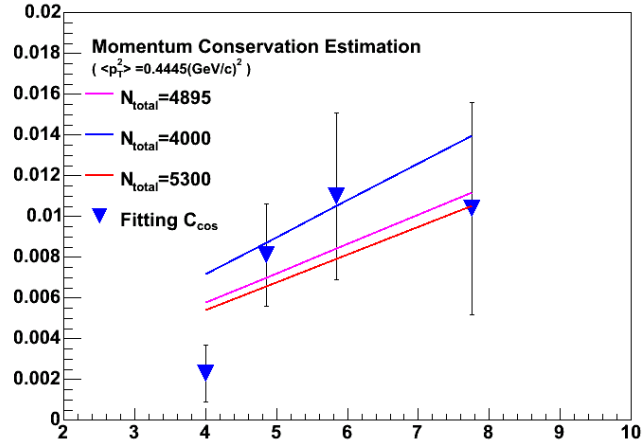


Figure 6.2: Magnitude of the fitted cosine function for $h + h$ correlations for different trigger p_T ranges in central (5%) $AuAu$ Collisions. The cut for associated particles was chosen as $2.5 \text{ GeV}/c < p_T^{\text{asso}} < 3.7 \text{ GeV}/c$.

spectra for p_{T1} and p_{T2} and $\langle p_T^2 \rangle$ was extrapolated from the power law fit of the unidentified charged hadron p_T spectra. We noticed that within the error bar, correlation term is consistent with a large momentum balancing volume ($\sim 10^3$ particles.) The total number of particles required to conserve the momentum is in agreement with the total multiplicity in $AuAu$ central collisions, which would mean that the energy loss thermalized with the bulk matter. This effect can also be deduced from the mean p_T of associated particles within the back side jet cone[25]. Figure 6.3 shows similar results at a lower p_T range.

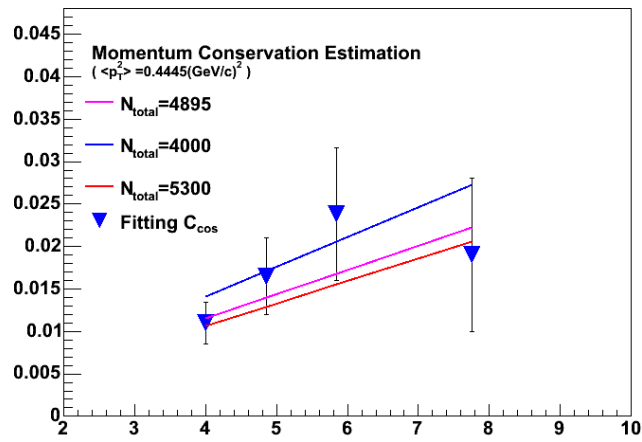


Figure 6.3: Magnitude of the fitted cosine function for $h + h$ correlations for different trigger p_T ranges in central (5%) $AuAu$ Collisions. The cut for associated particles was chosen as $2.0 \text{ GeV}/c < p_T^{\text{asso}} < 2.5 \text{ GeV}/c$.

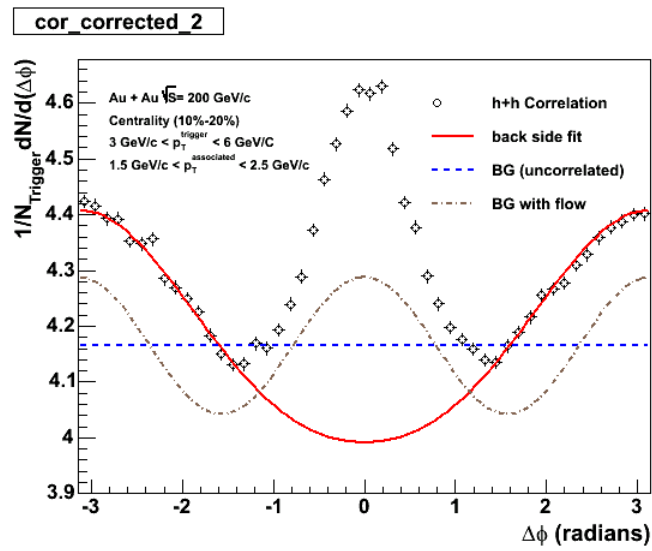


Figure 6.4: Sample of correlations of charged hadrons with $3 \text{ GeV}/c < p_T^{\text{trig}} < 6 \text{ GeV}/c$ and $1.5 \text{ GeV}/c < p_T^{\text{asso}} < 2.5 \text{ GeV}/c$. Dashed line are uncorrelated background calculated by convolution of the inclusive single particle spectrum.

6.3 Centrality dependence

In order to learn more about the correlations of momentum conservation, we are trying to fit the back side correlations for different centralities to extract the momentum conservation cosine term. For mid central collisions, effects of elliptic flow are significant, I use free parameters to characterized the contribution from the elliptic flow and uncorrelated background. I also exclude the same side correlation to avoid unnecessary complexities. The trigger particle p_T range is set to be between $3 \text{ GeV}/c$ and $6 \text{ GeV}/c$. The p_T range for the associated particle is set to be between $1.5 \text{ GeV}/c$ and $3.0 \text{ GeV}/c$. Figure 6.4 illustrates the the components of our fit which including inclusive background and flow. Figure 6.7 shows the correlations for all centralities and Figure 6.5 and 6.6 show the correlation samples for different centralities including the fit function.

From the fit three parameters can be retrieved, the magnitude of the uncorrelated background, the effective v_2 and the magnitude of the momentum conservation term. In the following section I will compare them with calculations.

6.4 Components of the back side correlation in central $Au + Au$ collisions.

Figure 6.8 shows the comparison between the uncorrelated background retrieved from the fit with the calculation from convoluting the inclusive single particle spectra. Figure 6.9 and 6.10 shows the actual difference and percentage difference between the two curve. The difference seems quite constant, with a slightly larger difference in peripheral bins. Despite the large statistical error, there is still a small but finite

cor_corrected_0

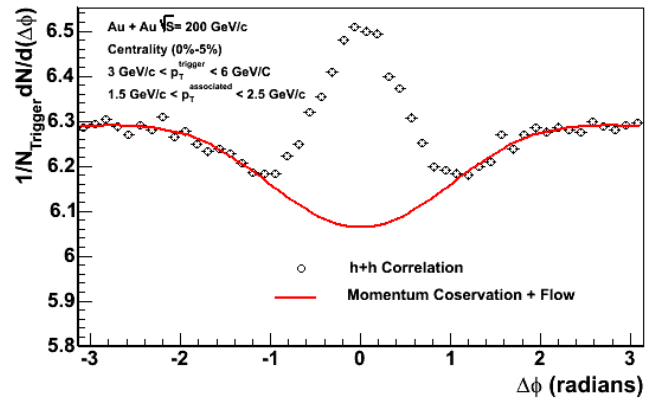


Figure 6.5: Correlation of charged hadrons with $3 \text{ GeV}/c < p_T^{\text{trig}} < 6 \text{ GeV}/c$ and $1.5 \text{ GeV}/c < p_T^{\text{asso}} < 2.5 \text{ GeV}/c$ in most central bin. Due to small effect of elliptic flow, background (solid red line) only show a shape of cosine.

cor_corrected_5

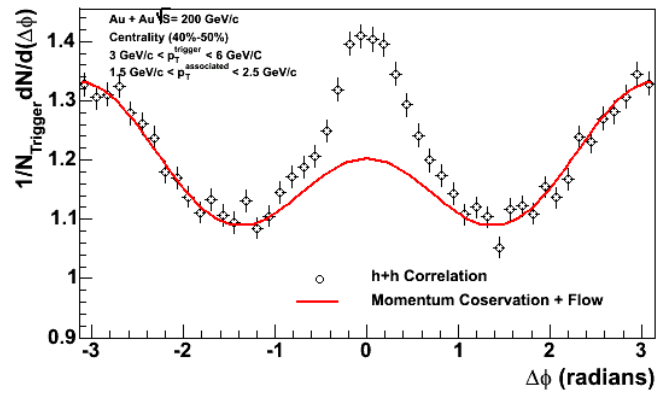


Figure 6.6: Correlation of charged hadrons with $3\text{GeV}/c < p_T^{\text{trig}} < 6\text{GeV}/c$ and $1.5\text{GeV}/c < p_T^{\text{asso}} < 2.5\text{GeV}/c$ in mid central bin. Large effects from elliptic flow change the shape of the background.

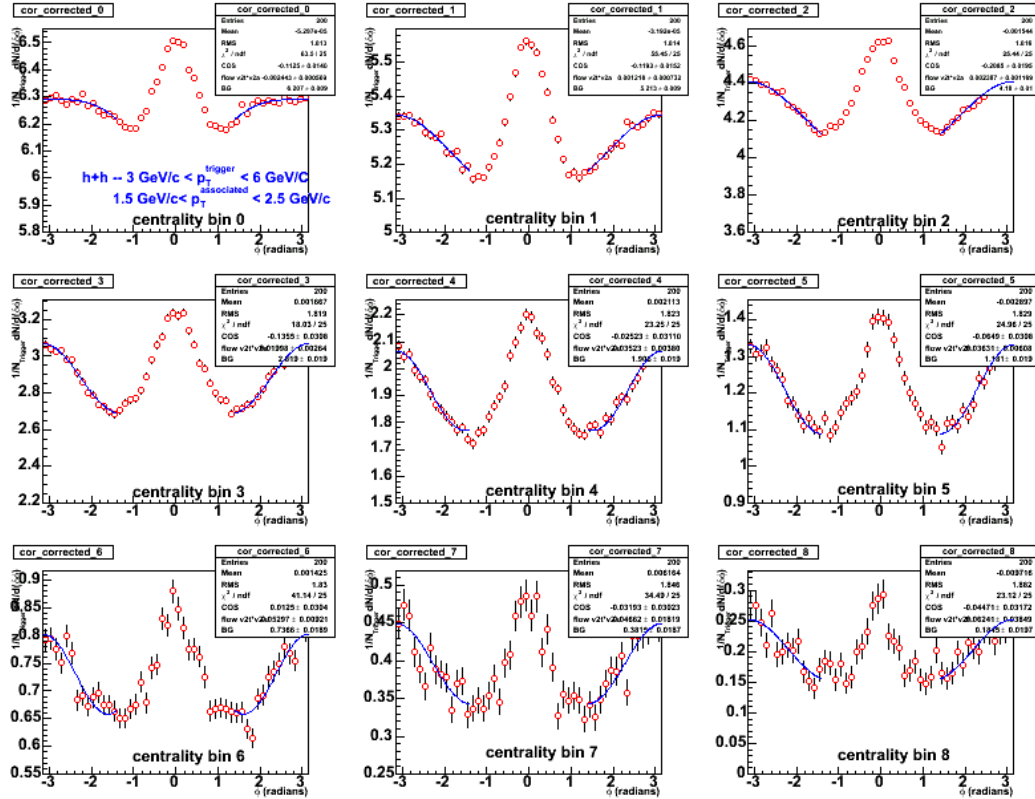


Figure 6.7: Correlations of charged hadrons with $3\text{GeV}/c < p_T^{\text{trig}} < 6\text{GeV}/c$ and $1.5\text{GeV}/c < p_T^{\text{asso}} < 2.5\text{GeV}/c$ for different centralities. Only back side of correlations are fitted to extract the component of flow, uncorrelated background and momentum conservation term (blue lines).

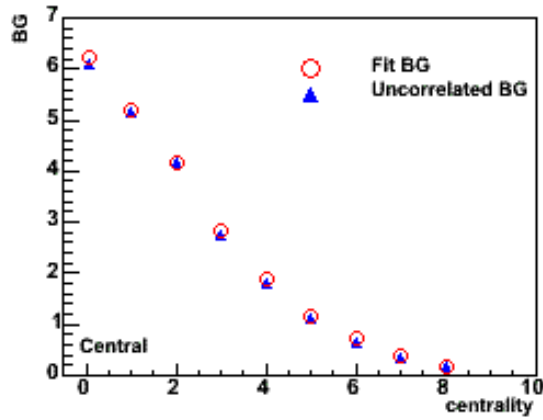


Figure 6.8: Fitted background compare to the uncorrelated background for different centralities

difference between the fitted and the calculated background.

The other component is the elliptic flow. For two particle correlations we have retrieved the effective flow component v_2^{eff} . Elliptic flow of unidentified charged hadrons has been measured independently by using the reaction plane method and the four particle cumulant method[41]. Figure 6.11 shows a comparison of the effective v_2 from the different methods.

The difference of the effective v_2 between reaction plane method and the 4-particle accumulant method have been discussed in detail previously [41]. Since the jet-like correlations can affect the measurement of v_2 in the reaction plane method (two particle correlation method), the v_2 deduced from this method is usually larger than the actual value especially in the peripheral collisions. On the other hand, the 4-particle accumulant method includes the corrections of non-flow effects and is usually more accurate than the two particle correlation method. It is suggested that the real elliptic flow value v_2 should lie between these two type of measurements since

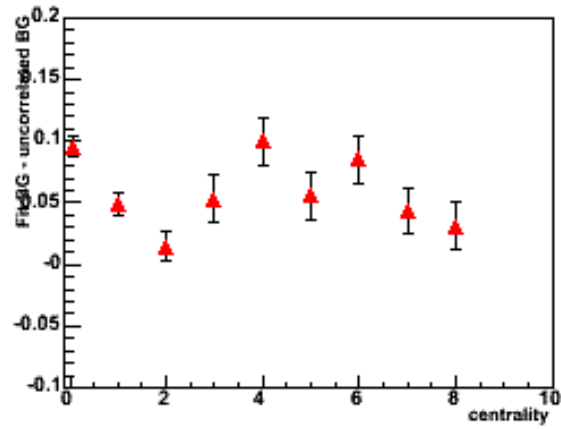


Figure 6.9: Difference between fitted background and calculated background

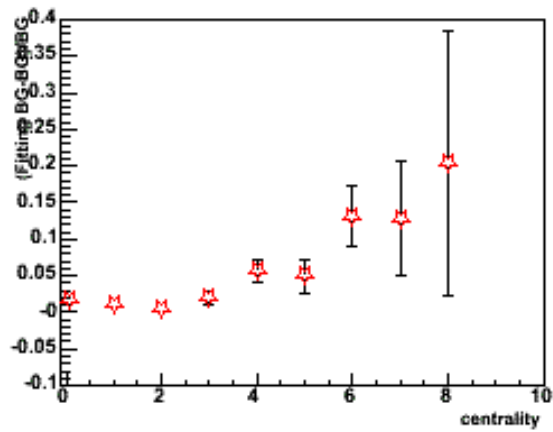


Figure 6.10: Percentage difference between fitted background and calculated background

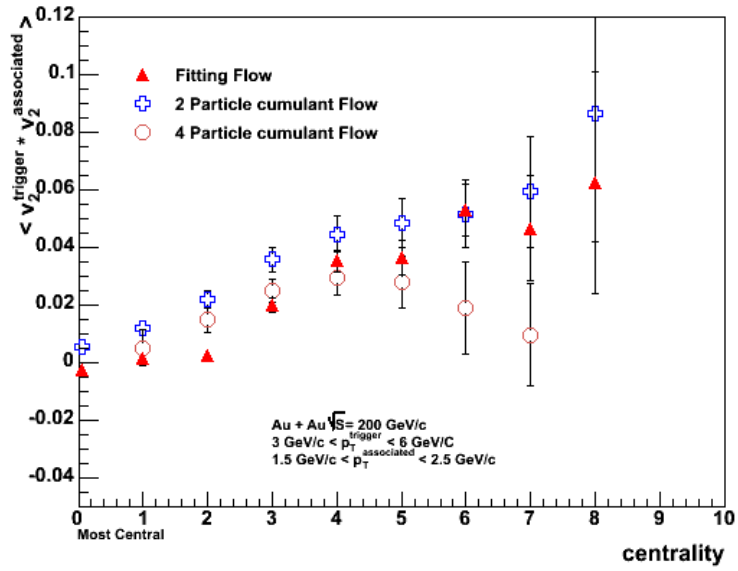


Figure 6.11: Comparison of $v_2^{\text{effective}}$ from the fit parameters and calculations from 2-particle and 4-particle cumulant methods.

4-particle could over-corrected the non-flow contribution(see details in [19]). The effective v_2 from our fits seems to follow the trends of two-particle v_2 except for the central collisions. This might be due to the effects from the correlation of momentum conservation. Since in our fit, the auto correlation from momentum conservation was corrected for central collisions, the effective v_2 for two particles correlations are reduced. Since the 4-particle cumulant method fails to measure the flow in the most central $AuAu$ collisions, we can not calculate the effective v_2 from 4-particle cumulant method in the most central bin. It is also necessary to point out that two particle correlations (same particle at same/different p_T range or different particles) are very sensitive to the v_2 . All the existing measurement of v_2 have been conducted on the same particle at the same p_T range. Correlations of same particles at different p_T range or different particles can work as a good cross check for v_2 measurements.

In Figure 6.12 I show the retrieved magnitude of the momentum conservation term compared to calculations based on mid rapidity multiplicity (dN/dy) scaling for different centralities. As one can see, the parameters been retrieved from the fit are consistent with momentum balance over many particles in central collisions [51]. The estimated total multiplicity of the central $AuAu$ at 200 GeV/c is roughly around several 5000, including charged neutral particles. Since the remnants of the away side jet correlation has a broad distribution, its contribution will result in a larger amplitude in cosine term therefore a smaller N . For central collisions in $AuAu$, the momentum balance contribution is small but finite. Since the jet correlation on the away side is also small, the correction due to momentum conservation can be important when measuring the associated particle yields per trigger. However technically, because the

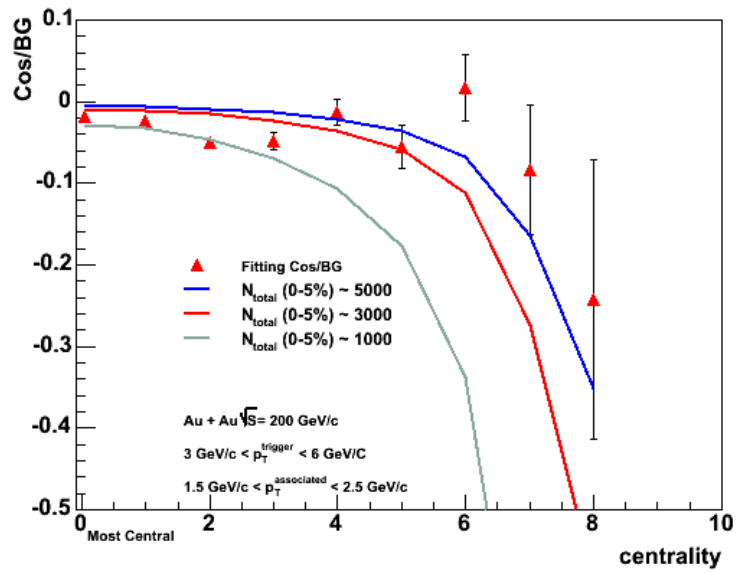


Figure 6.12: Correlation from the momentum conservation as the function of collisions centralities in $AuAu$ at $200 \text{ GeV}/c$.

wide distribution of away side jet signal, the direct separation of jet signal and momentum conservation is not trivial. One approach would be to treat the momentum conservation term as a common background and estimated its magnitude from the total multiplicity of events [25][51].

6.5 Discussion

The away side distribution of the jet shows a broad shape in central $AuAu$ collisions which is in agreement with a cosine distribution. One question one may ask is how is the lost energy redistributed over the medium. This question is related to p_T fluctuations in the medium caused the jet quenching. Generally one can treat the medium as the particles in a ground state with average momentum p_T . The redistribution of absorbed energy from the quenched jet introduces an addition transverse energy and therefore a p_T fluctuation. If the lost energy is redistributed over many particles the fluctuation should be much different(smaller) than when redistributed among a small amount of particles. In a very naive model, we can assume an original system of n particles with transverse momentum p_T^{ori} , which can be described as:

$$\{p_T^{ori}\}, \quad \langle p_T \rangle = p_0, \quad \langle p_T^2 \rangle = p_1^2 \quad (6.5.1)$$

After absorbing the energy loss ε_T a subset of m particles become more energetic. Let's assume the energy is evenly distributed over these particle which leads to

$$\begin{aligned} \{p_T^{new}\} &= \{p_T^{ori}\} \cup \{p_T^{excited}\} \\ p_T^{excited} &= p_T^{ori} + \frac{\varepsilon}{\alpha}, \quad \alpha \equiv \frac{m}{n-m} \end{aligned} \quad (6.5.2)$$

from which one can easily deduce the mean p_T of the new system ,which is only affected by the fraction of the number of particles n and the total deposited transverse energy ε and is independent of α .

$$\langle p_T^{new} \rangle = p_0 + \frac{\varepsilon}{n}; \quad (6.5.3)$$

The statistical fluctuation of p_T can then be calculated for the new system.

$$\begin{aligned} \langle (\Delta p_T^{new})^2 \rangle &= \frac{1}{n} \langle (n-m) \langle (p_T^{ori} - p_0 - \frac{\varepsilon}{n})^2 \rangle + m \langle (p_T^{ori} + \frac{\varepsilon}{m} - p_0 - \frac{\varepsilon}{n})^2 \rangle \rangle \\ &\quad \text{using } \alpha = \frac{m}{n-m}; \\ LFS &= \frac{1}{1+\alpha} \langle (p_T^{ori} - p_0)^2 \rangle (1+\alpha) + \frac{\varepsilon^2}{(1+\alpha)\alpha} \\ &= p_1^2 + \frac{\varepsilon^2}{(1+\alpha)^2\alpha} \end{aligned} \quad (6.5.4)$$

From Equation 6.5.4 one can then obtain a relation between α and the statistical fluctuation of the old and new system as,

$$\alpha^{-1} = \frac{\langle (\Delta p_T^{new})^2 \rangle - \langle (\Delta p_T^{ori})^2 \rangle}{(\langle p_T^{new} \rangle - \langle p_T^{ori} \rangle)^2} \quad (6.5.5)$$

This result is generally true for all binary energy system. Although it might be far off from the reality, it can be used as a first approximation to study the excited state of the medium. We can choose the back side medium in the presence of jet like particles, and compare to the inclusive background in the absence of the jet like particles. The measurement of α will then provide information about the scope of the redistribution of the absorbed energy.

Chapter 7

p_T dependence of correlation

In this chapter I will show the dependence of the correlation on the transverse momentum p_T of the trigger and associated particles in $AuAu$ collisions. Since different production in each processes have very different p_T dependence, this study will provide criteria to distinguish between different models. It will help us to understand the jet and hadronization processes in $AuAu$ collision not only macroscopically but also microscopically. Such an understanding will be very helpful in gaining a better picture of particle production in relativistic heavy ion physics.

7.1 Correlation production mechanism: Fragmentation or Recombination ?

The hadron production mechanism is one of the most profound phenomenons. In central heavy ion collisions, it is assumed that different hadron production mechanisms dominate different p_T ranges. In the lower p_T range, Statistical Models seem to working pretty well to explain the particle ratios by using a single freeze out temperature [52][47]. Hydrodynamics give a good description for the single particle spectra. At

intermediate p_T (2 - 5 GeV/c) the hydro models begins to break down. In this range a scenario in which hadrons form instantly through recombination of the constituent quarks seems to work well. At even higher p_T , where pQCD is applicable, hadrons are produced via fragmentation of a color string. In general, partons from hard scattering carry significant amount of transverse energy. Due to confinement, the field is limited to color flux tube, i.e. a string. Hadrons will be produced via the gluon radiation if the string is stretched. In the presence of a medium, the interaction between the parton with the medium causes the quenching effect. The experimental measurement of R_{AA} in central $AuAu$ collisions confirms such an effect. At the same time it has been found that baryons and mesons exhibit a very different amount of quenching in the intermediate p_T range. This effect indicates the transition to quark recombination or quark coalescence. Within the context of a recombination model, the baryon and meson difference is caused by the difference of the number of constituent quark. One of the most convincing applications of the coalescence picture is the constituent quark scaling of the elliptic flow coefficient v_2 [16][53]. This indicates that at intermediate p_T ¹ recombination seems to dominate the hadron production [54][55]. Naturally one may ask the question, how will this affect the correlation production? In a thermal recombination picture randomly produced hadrons with no partners should not contribute to the azimuthal correlations. However the recently developed recombination via shower parton and thermal parton will surprisingly amplify the correlation at intermediate p_T . Shower partons are originated from the jet fragmentation processes and therefore are correlated. In the model, they are allowed to recombine with thermal partons to form hadrons. The produced hadrons are correlated due to the correlation of the

¹The definition of intermediate p_T is not clear yet. Most people agree that between 1.5-5 GeV/c are considered the boundary between "soft" and "hard".

original shower partons. Contributions of the thermal partons increases total energy inside the jet cone. This model might give us a possibility to resolve the large AA/pp ratio in the correlation yield in the intermediate p_T range (Figure 5.17). In Appendix C I describes the basic principles of the shower parton recombination model. In the following section I will present the comparison of our data and the calculation from the model[38][45][56].

7.2 Associate p_T distribution

From correlation functions we can retrieve the associated particle p_T distribution for a fixed trigger p_T range. In the context of fragmentation, such a dependence is corresponding to the fragmentation process and its medium modification. In Figure 7.1 and I show the associated particle spectra for different trigger particle species with a fixed trigger p_T range (3 to 6 GeV/c) in central $AuAu$ collisions. The difference between different trigger particle species is not significant compared to the error bar except maybe for the first few points between 1.0 GeV/c to 1.5 GeV/c . The points are fitted with a thermal exponential distribution (blue dashed line). The lower points are the reference pp data using the same cut. There are several facts we can learn from this plot. First, we again observe a large AA/pp ratio. This seems always be true for the intermediate p_T range in central $AuAu$ collisions independent of trigger particle species. Second, we have found that the same side p_T spectra in central $AuAu$ collisions are softened compared to pp measurements. This also indicates that an additional softer component contributes to the correlated hadron production process which, in the context of the shower parton recombination model, can be related to the thermal parton contribution. Figure 7.2 shows the p_T spectra for the same side

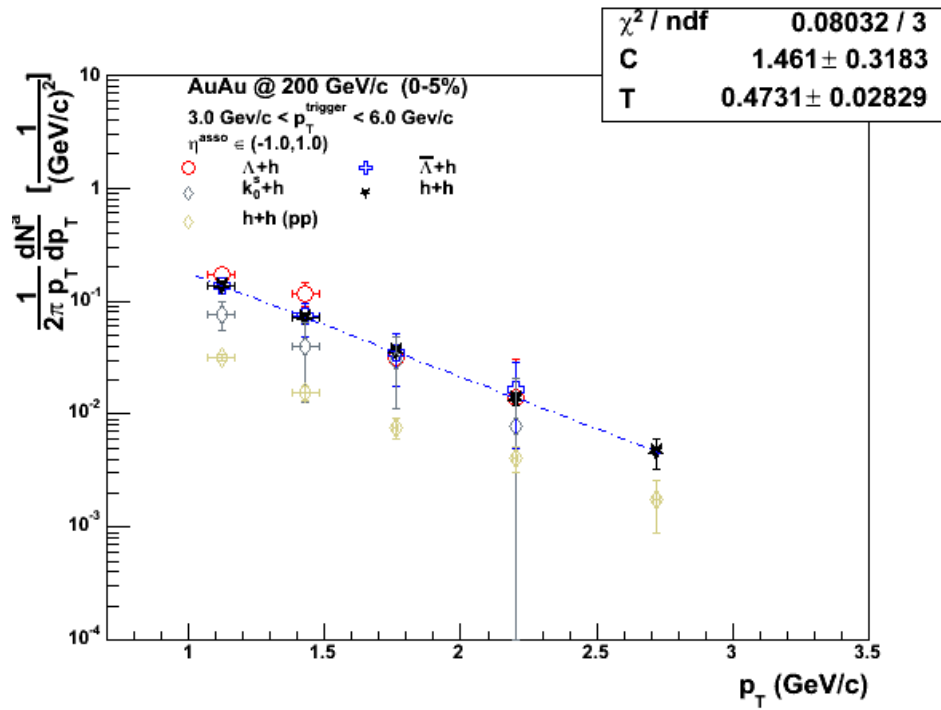


Figure 7.1: Spectra of same side associated particle per trigger particle at $3 \text{ GeV}/c < p_T^{\text{trig}} < 6 \text{ GeV}/c$ in central (0-5%) *AuAu* collisions. Acceptance cuts are between ± 1 for both trigger and associated particles.

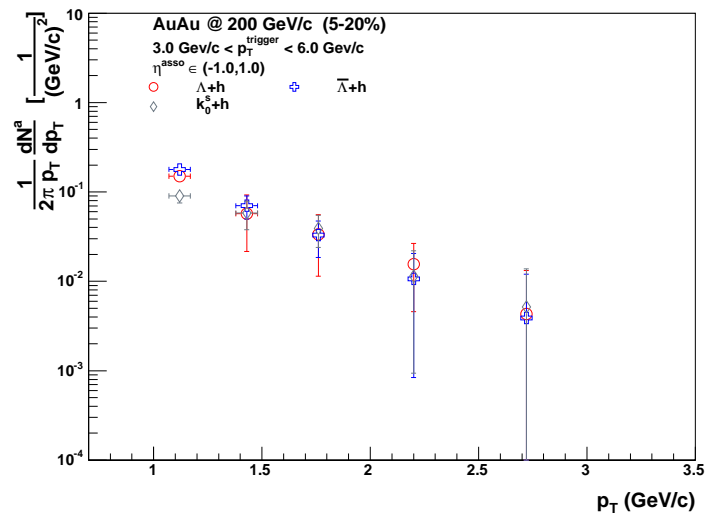


Figure 7.2: Spectra of same side associated particle in mid central (5-20%) *AuAu* collisions.

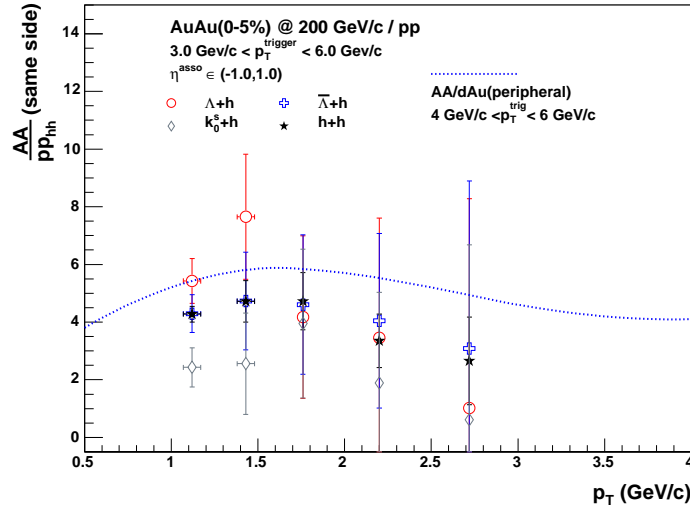


Figure 7.3: AA/pp ratio for different trigger particle species as the function of associated particle p_T in central $AuAu$ collisions. The large AA/pp ratio in the range between 1.0 2.5 GeV/c shows other hadron production mechanism in addition to the jet fragmentation and medium modification.

associated particle in mid central collisions. Figure 7.3 shows the AA/pp ratio for different particle species compared to the theoretical calculation of shower parton recombination model by R. Hwa. and C.B. Yang[12][57]. Despite the large error bar, the AA/pp ratio peaks around 1.5 GeV/c and then drop off at higher p_T . This can be understood by turning off of the thermal-shower recombination term (TS) in Equation C.0.5. Only shower-shower recombination (SS) is possible at high p_T because of the thermal parton distribution drops off at high p_T . Figure 7.4 shows the AA/pp ratio of the same side associated particle yield for different centralities As one can see, the ratios approach unity towards peripheral collisions and towards high p_T .

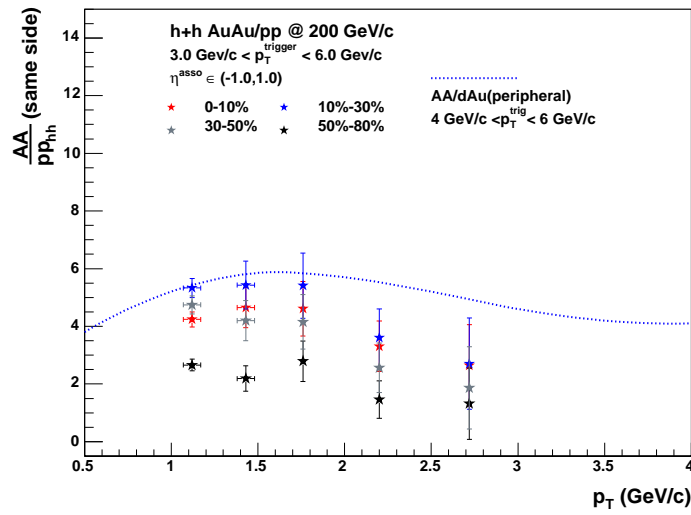


Figure 7.4: AA/pp ratio for unidentified charged hadrons as the function of associated particle p_T for different collision centralities. The AA/pp ratio approach to unity from central to peripheral and also from low p_T to high p_T .

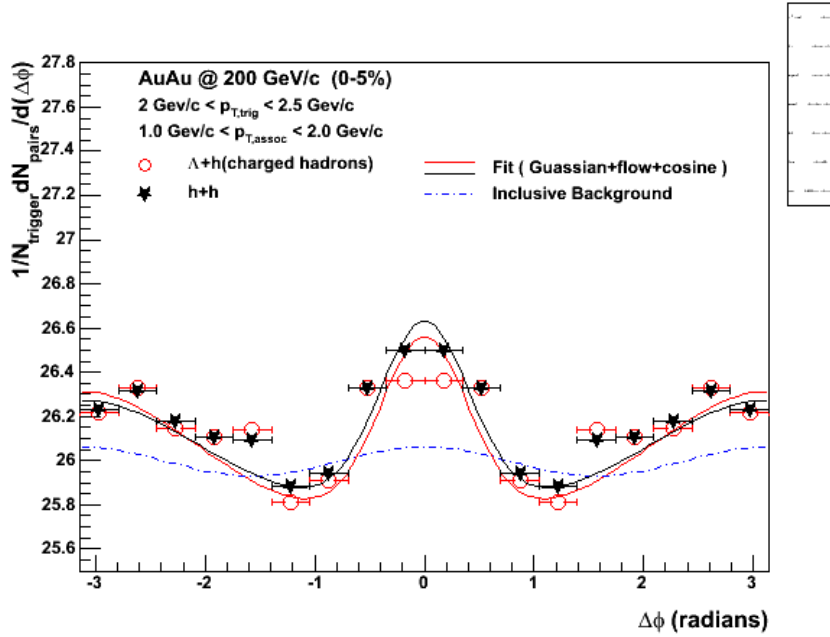


Figure 7.5: Sample correlation function for trigger p_T dependence studies. Blue dashed line show the calculated inclusive background. At this p_T range same side yield of hh seems a little bit larger than (if not equal to) $\Lambda + h$

7.3 Trigger p_T distribution

In our definition of the correlation function, the trigger particle is used to identify the jet production. The trigger p_T dependence of the correlation yield should also provide us with information about the particle production mechanism in a certain p_T range. The trigger p_T dependence for different particle species should provide additional information about the correlated di-hadron production in the intermediate p_T range. I have chosen the most central bin in $AuAu$ for this study to minimize the effect of elliptic flow. Figures 7.5 and 7.6 show the sample correlations for two different trigger p_T bins for different particle species. In both plots the dashed lines represent

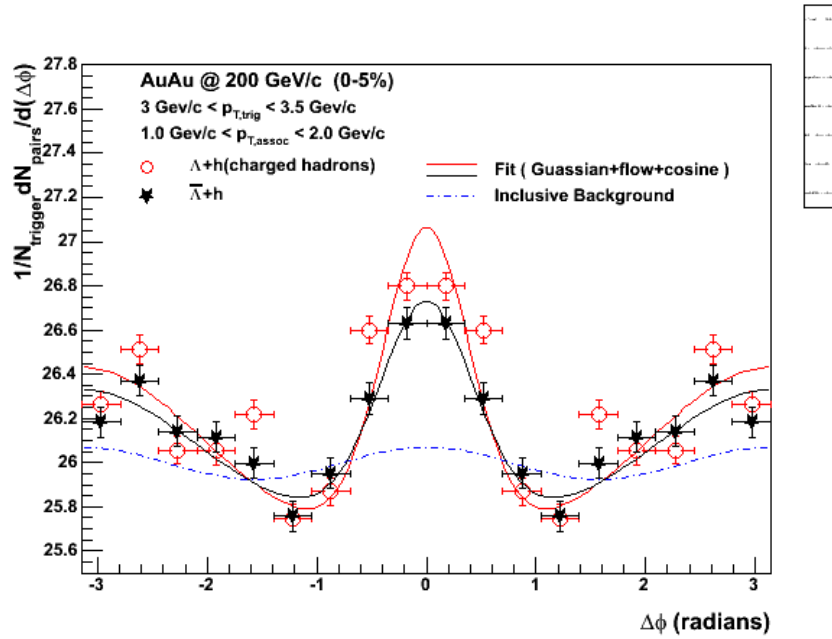


Figure 7.6: Sample correlation function at relative higher p_T . Raw correlation function of Λ trigger with charged hadrons seems have a larger amplitude on the same side compared to the $\bar{\Lambda}$ trigger. However such difference could be due to uncertainty of the systematics.

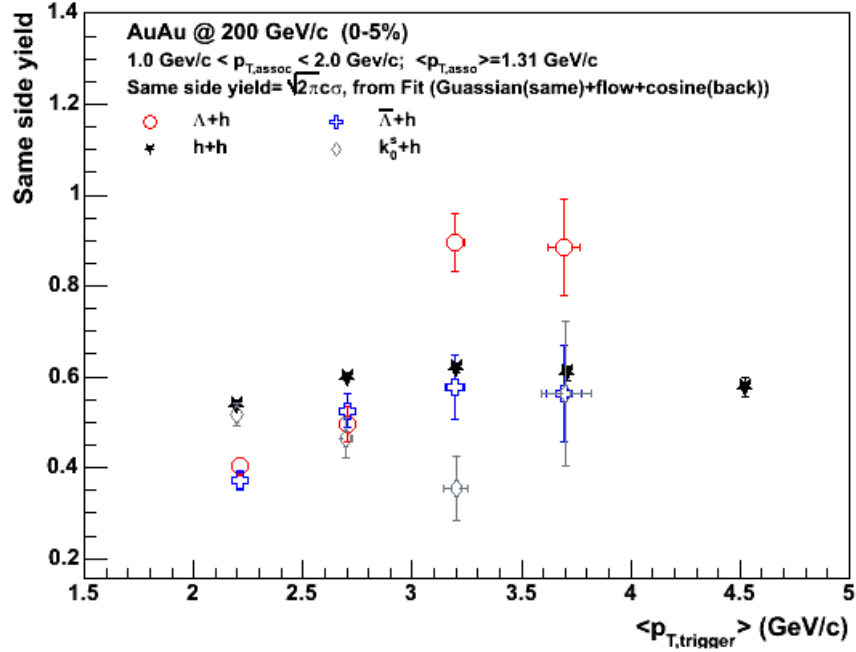


Figure 7.7: Same side yield as the function of trigger particle p_T for different particle species for a fix phase space for the associated particle. ($1.0 \text{ GeV}/c < p_T^{asso} < 2.0 \text{ GeV}/c$) The number of associated particles are retrieved from the correlation function by using the fitting method on the same side.

the uncorrelated background calculated from the convolution of the single particle inclusive spectra. The correlations were then fitted with a Gaussian on the same side. In order to retrieve the yield, I am using two independent methods, one uses the fit, the other counts simply the bin content over the inclusive background(modulated by flow). Results from both methods are listed in Figure 7.7 and 7.8.

Based on our measurements, different trigger particle species show a different associated yield as a function of the trigger p_T , which indicates a possible baryon and meson difference and particle/anti-particle difference. Here i am only listing

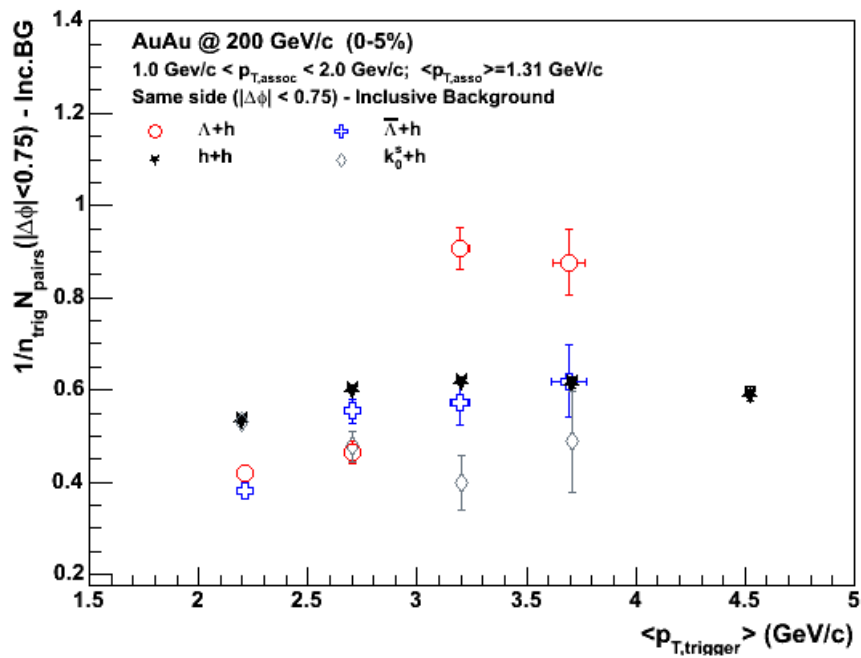


Figure 7.8: Same side yield as the function of trigger particle p_T for different particle species for a fix phase space for the associated particle. ($1.0 \text{ GeV}/c < p_T^{asso} < 2.0 \text{ GeV}/c$) The number of associated particles are retrieved direct subtraction of the calculated inclusive background.

the statistics errors. The systematic errors are discussed in the following section. For charged hadrons the same side yield shows a mild increase followed by a mild decrease as the trigger p_T increase. This seems to indicate a saturation effect due to the limitation of the total energy of the shower, which will be discussed in section 7.5.

7.4 Studies on the systematic uncertainty

The error bars shown in the previous plots are statistical only. Additional errors need to be considered regarding the systematics of our analysis. In this section I will give a brief discussion of the systematics that will affect our measurements.

7.4.1 Uncorrelated background

The main source of the systematic uncertainty is due to the uncertainty of the magnitude of the uncorrelated background. Since I am using the calculated uncorrelated background from the convolution of the single particle distributions, the uncertainty of our calculation relies on the accuracy of our measurement of the single particle distributions, in particular the fluctuation in the multiplicity for different centrality bins can cause a trigger bias. It has been found that high p_T trigger particles are more likely to be found in central events with high multiplicity. However the fluctuations in central collisions are not significant as is shown in Table 7.1. In my analysis, I am using the difference of the fitted background and the calculation as the systematic error, which should be considered the upper limit of systematic uncertainty. For the

p_T^{trig} (GeV/c)	BG^{inclu}	Stat. Error (%)	Sys. Error (%)	contribution to yield
2.0-2.5	25.9969	0.00079 (0.01%)	0.04(0.015%)	13%
2.5-3.0	25.997	0.002(0.01%)	0.041(0.015%)	12%
3.0-3.5	25.997	0.005(0.01%)	0.059(0.022%)	10%
3.5-10.0	25.997	0.0056(0.01%)	0.061(0.022%)	11%

Table 7.1: Systematic Error for uncorrelated background. The p_T range for the associated particles are between 1.0 GeV/c and 2.0 GeV/c. ($\eta^{asso} \in (-1.0, 1.0)$).

most central collisions such uncertainty are less than .5%. However because the magnitude of the background is much larger than jet-like correlations, the effect on the same side yield is about 11% as shown in Table7.1.

7.4.2 Leading particle bias

Another effect in our measurements is the leading particle bias. An event could contain a second high p_T particle which exceed the transverse momentum of the trigger particle. However such an effect is usually negligible due to its low probability. Figure ?? show the comparison of the correlations before and after the correction for $bar\Lambda$ trigger. The estimated systematic error is less than 1.4%.

7.4.3 Elliptic flow

The uncertainty in the elliptic flow contribution is due to the error on the measured v_2 . When calculating the yield, the magnitude of the elliptic flow v_2 can affect both same side and back side yields since it peaks also at 0 and π . The uncertainty of v_2 is taken from the systematic errors in the published STAR v_2 analysis. In central AuAu collisions, this uncertainty is minimal due to the small value of v_2 . The total systematics of v_2 are about 2–3%. In table 7.2 we have listed the estimated systematic

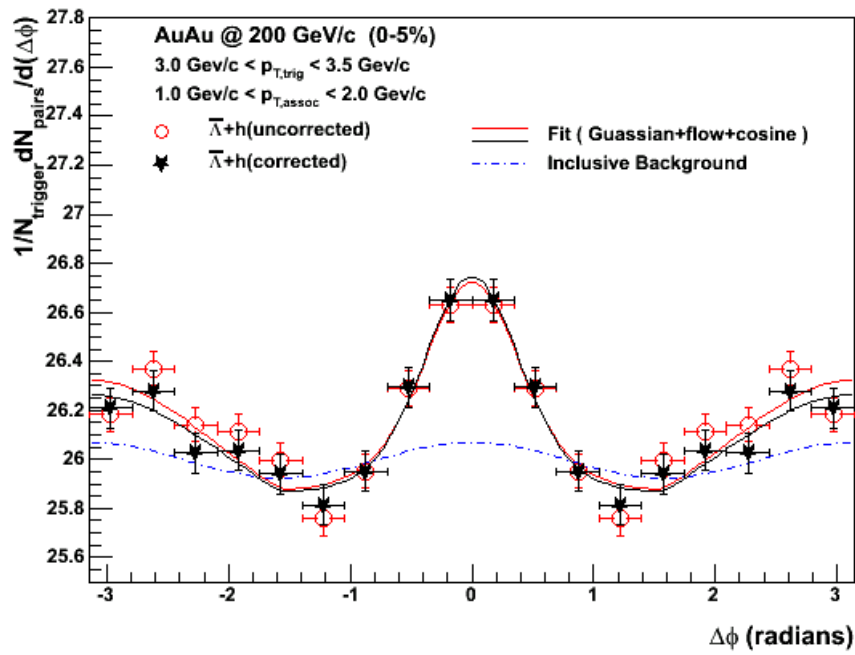


Figure 7.9: Leading particle trigger bias comparison. Before and after correction.

p_T^{trig} (GeV/c)	$v_2^{eff} = \langle v_2^{trig} * v_2^{asso} \rangle$	Error (%)	contribution to yield
2.0-2.5	0.001255	0.00031 (24%)	2.6%
2.5-3.0	0.001401	0.000531(38%)	2.3%
3.0-3.5	0.001402	0.00092(65%)	2.1%
3.5-10.0	0.00145	0.0009(65%)	2.3%

Table 7.2: Systematic Error from elliptic flow in central AuAu collisions.

errors from v_2 for different trigger p_T . For peripheral collisions the uncertainty of the flow component v_2 is smaller however the magnitude of v_2 is larger which makes the effect of the flow more pronounced.

7.4.4 Systematics in yield retrieval

An additional systematic uncertainty might coming from the methods that are used to retrieve the same side yield. We compare the difference between the two independent methods(bin counting and fit) and using their difference to construct a systematic error. For the four trigger p_T bins the corresponding errors are a few percent. For the $\Lambda + h$ correlations they are 3.5%, 3.2%,0.9%, 1.1% for the p_T ranges (2.0, 2.5), (2.5, 3.0), (3.0, 3.5), (3.5, 10.0) respectively.

As discussed previously the misidentified V_0 s can also add to the systematic error. However due to the large S/B ratio in our mass reconstruction such contributions are negligible.

7.5 Discussions

In this chapter, we have shown the p_T dependence of the jet-like correlation yield. In the intermediate p_T range, the same side correlation for central $AuAu$ collisions show a much larger amplitude than pp independent of the trigger particle species. A

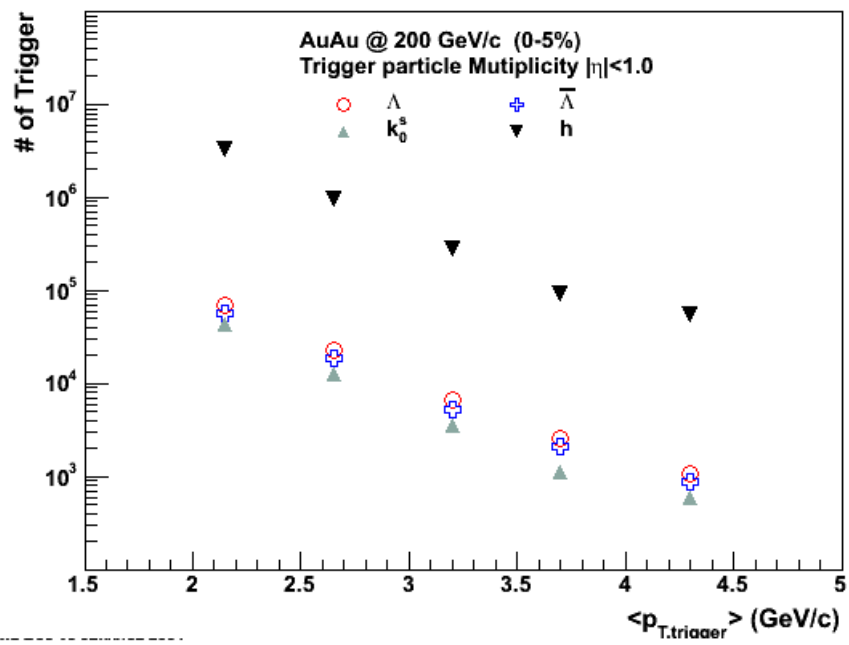


Figure 7.10: Trigger particle numbers for our analysis. It seems that the difference in the same side correlation yield is not due to the abnormal distribution of the trigger particle

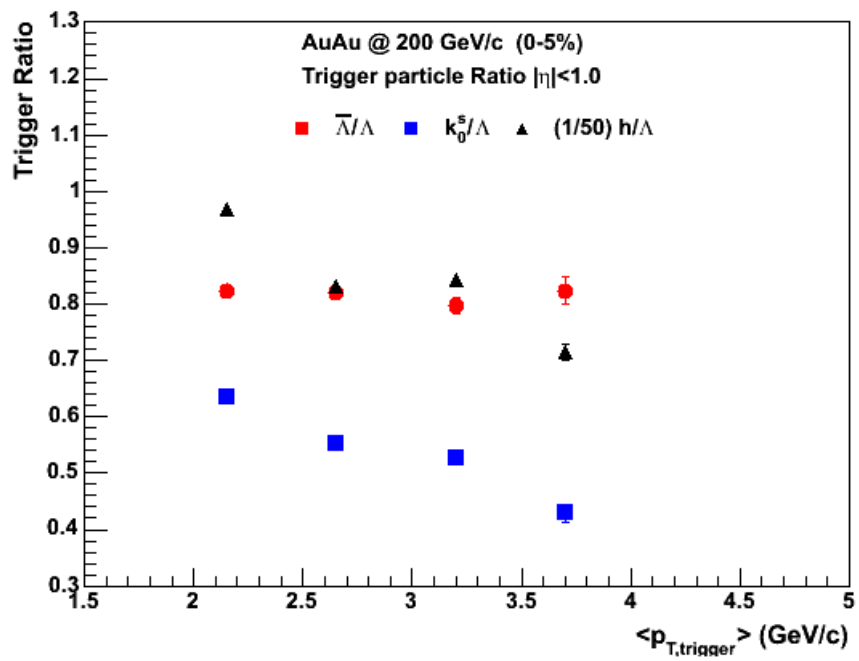


Figure 7.11: Particle ratio between different triggers. No abnormality has been found could cause the difference in same side yield.

shower parton recombination model seems to provide a possible scenario. Based on this model, the thermal soup (or fireball) could work as an amplifier for the traversing jet. Additional energy and particles are deposited into the jet cone via recombination during the hadronization processes. On the other hand without the medium, all the energy has to come from the initial parton. This scenario provides an answer to the large AA/pp ratio at intermediate p_T range. At high p_T , contributions are dominated by the shower-parton recombination (SS term) only, therefore the ratio approaches unity. The trigger particle p_T dependence shows distinct differences between different particle species. This could have many reasons. As discussed in chapter one, the fragmentation processes themselves could be different for different partons. Such effects are usually small in pp. In *AuAu* collisions, the large AA/pp ratio shows that the medium amplifies the fragmentation process though from our data I feel confident to say that the correlation at intermediate p_T can not be described by jet fragmentation and its modification alone. It is in agreement with a shower parton recombination model. Other nuclear dynamic effects (such as radial flow and multiple nucleon collisions) have to be excluded to confirm such a picture.

Chapter 8

Summary

In this work, I have studied the two particle correlations using different identified trigger particles at intermediate p_T in $AuAu$ and pp collisions. I can draw the following conclusions.

- The over broadening of the back side correlation shows the quenching effect in central $AuAu$ collisions. This is in agreement with previous measurements with unidentified charged hadron correlations at high p_T .
- Large AA/pp ratios of the same side correlation yields are not due to the "trigger bias" effects. However they are in agreement with a shower parton recombination picture.
- Different trigger p_T dependencies for different particle species are measured in central $AuAu$ collisions. The trigger particle effects could be due to the applied effects of the gluon quark jet difference or other medium induced effects. As discussed in chapter 7. Many reasons contribute to the trigger particle dependencies.

One of reason of such difference could be related quark-gluon jet differences. It has been measured that the gluon and quark jets have very different distribution due to their color formation factor. Hadrons produced via gluon jet fragmentation trends to have lower energy and higher multiplicity compared to quark jet. This difference could contribute to the correlation measurements if the trigger particle selection has a gluon or quark jet "bias".

Another reason that could contribute the trigger particle dependencies could be related the particle-anti particle difference. Finite baryon density could also affect the correlation. Comparing Λ and $\bar{\Lambda}$ triggered correlations. Leading particles at high p_T range are formed through shower-parton recombination (SSS). The remnant fragments of the jet are anti-quark favored(in case of $\bar{\Lambda}$ it will be quark favored). To form energetic associated mesons, it is easier for the anti-quark fragments compared to the quark fragments since it is easier to pick up energetic quarks than anti-quarks. This could be the one of the possible scenarios to explain the difference between Λ and $\bar{\Lambda}$ at high p_T .

In addition, the baryon and meson difference could also contribute to the different trigger dependencies. Although the centrality dependence measurement shows only a weak difference between meson and baryon triggered correlations(in our case the Λ and the K_0^S), in central collisions, both their magnitude and their p_T dependence are significantly different. We have not find an obvious constituent quark scaling. However, this could be due to the complex nature of correlation at this p_T range.

In the future, with more statistics available, identified particle correlation studies will be very important. Three particle correlations can help us learn more about

detail features of the correlation such as opening angles (both same side and away side) and fluctuations of associated particles within the jet cone. Such information will provide important leads to our understanding of hadronization processes. In addition, correlation with identified trigger and associated particles will also let us probe microscopically into the details (flavor) of hadronization processes.

Appendix A

j_T and k_T related to jet correlation

Here in this Appendix, I will describe j_T and k_T and their relations with jet/di-jet correlations from experiment point of view.

In a parton model (PM), with so-called collinear approximation [58], all partons are assumed only carrying longitudinal momenta. The cross sections of QCD subprocess are calculated usually in the leading order (LO), as well as in the next to leading order(NLO). The transverse momentum of the incident partons are neglected. This allows to describe quite reasonably the experiment data on the cross sections and single hadron productions. However it can not reproduce the azimuthal correlation of jet, which depends on the transverse momentum of incident partons. An usual treatment is to introduce a random transverse momentum kick k_T , which in general follows a exponential distribution[58][59]. This allows to describe quantitatively the two-particle correlations.

In a similar way, j_T was introduced to characterize the transverse momentum(with respect to the jet axis) distribution within the jet cone (see FigureA.1). It represents the transverse cone size of the hadronic shower along the jet. On the other hand

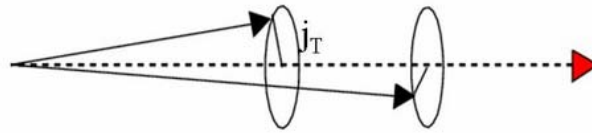


Figure A.1: j_T represents the transverse cone size of the hadronic shower with respect to the jet axis

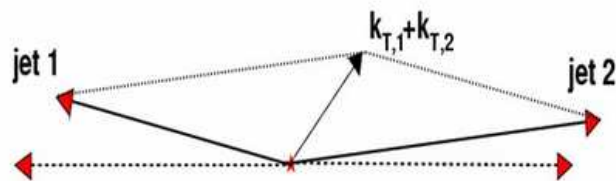


Figure A.2: k_T represents the transverse momentum differences between two jet axis in a di-jet, which is equal to the total transverse momentum of the two incident partons.

k_T represents the total transverse momentum difference(with respect to the collision axis) between the two jets (see Figure A.2), which incorporates the initial transverse momentum difference of incident partons.

In pp collisions, the width of the same side peak of di-hadron jet correlations is related to j_T and the width of the back side is related to the convoluted effect between j_T and k_T . The relations between them are described in Equation A.0.1. This explains the reason why we always measured a larger back side width in pp collisions.

$$\langle |j_{\perp,y}| \rangle = \langle p_{\perp} \rangle \sin \frac{\sigma_{Same}}{\sqrt{\pi}} \quad \langle |k_{T,y}| \rangle \approx \langle p_T \rangle \sqrt{\sigma_{Back}^2 - \sigma_{Same}^2} \quad (\text{A.0.1})$$

In dAu, AuAu collisions, the scenario becomes more complicate. One of the approach is to assume the back side incorporates "additive" medium modification effects while the same side remain unchanged[60].

$$\begin{aligned} \langle k_T^2 \rangle_{dAu} &= \langle k_T^2 \rangle_{pp} + \langle k_T^2 \rangle_{coldnucl, Initialstates} \\ \langle k_T^2 \rangle_{AuAu} &= \langle k_T^2 \rangle_{pp} + \langle k_T^2 \rangle_{coldnucl, IS} + \langle k_T^2 \rangle_{QGP, finalstate} \end{aligned} \quad (\text{A.0.2})$$

Using Equation A.0.1 and A.0.2, one can retrieve different k_T effect induced by different medium from the correlation measurements.

Appendix B

Momentum conservation in azimuthal correlations

Generally, for a system of N uncorrelated particles with momenta p_1, p_2, \dots, p_N , with their components in the transverse direction as $p_{T1}, p_{T2}, \dots, p_{TN}$, from conservation of momentum we have $\sum_{i=1}^N p_i = \text{Const.}$. Since we are only interested in azimuthal correlation which relate to the momentum conservation in the transverse plane, the condition is described as following,

$$\sum_{i=1}^N p_T^N = 0. \quad (\text{B.0.1})$$

For any sub group of k particles, the probability distribution of the momentum p_1, p_2, \dots, p_k can be expressed in terms of product of the single particle distributions.

$$f_c(p_1, p_2, \dots, p_k) \equiv \frac{\left(\prod_{i=1}^k f(p_i) \right) \int \delta^2(\sum_{i=1}^N p_T^N) \prod_{j=k+1}^N (f(p_j) d^3 p_j)}{\int \delta^2(\sum_{i=1}^N p_T^N) \prod_{n=1}^N (f(p_n) d^3 p_n)} \quad (\text{B.0.2})$$

Where the $f(p)$ denotes the normalized single particle momentum distribution. In order to calculate f_c we use the following approximation. Let $P_T = \sum_{i=1}^M p_{Ti}$. When M is large, according to the central limit theorem we would expect a Gaussian

distribution as follows:

$$\begin{aligned}
F_M(P_T) &\equiv \int \delta^2(-P_T + \sum_{i=1}^M p_{Ti}) \prod_{j=1}^M (f(p_j) d^3 p_j) \\
&= \frac{1}{\pi \sigma^2} \exp\left(-\frac{P_T^2}{\sigma^2}\right)
\end{aligned} \tag{B.0.3}$$

where

$$\sigma^2 = \langle P_T^2 \rangle = M \langle p_T^2 \rangle$$

By applying Equation ?? to 3.6.5, we can get the distribution f_c for k particles,

$$\begin{aligned}
f_c(p_1, \dots, p_k) &= \left(\prod_{i=1}^k f(p_i) \right) \frac{F_{N-k}(-\sum_{i=1}^k p_i)}{F_N(0)} \\
&= \left(\prod_{i=1}^k f(p_i) \right) \frac{N}{N-k} \exp\left(\frac{-(\sum_{i=1}^k p_i)^2}{(N-k) \langle p_T^2 \rangle}\right)
\end{aligned} \tag{B.0.4}$$

Equation B.0.4 gives the general contribution to correlations from conservation of momentum. For two particle azimuthal correlation, we have,

$$f_c(p_1, p_2) = f(p_1)f(p_2) \frac{N}{N-2} \exp\left(\frac{(p_{T1} + p_{T2})^2}{(N-k) \langle p_T^2 \rangle}\right) \tag{B.0.5}$$

by assuming $N \gg 1$ with Taylor expansion to the leading order of $1/N$ we have,

$$\begin{aligned}
f_c(p_1, p_2) &= f(p_1)f(p_2) \frac{N}{N-2} \exp\left(\frac{(p_{T1} + p_{T2})^2}{(N-2) \langle p_T^2 \rangle}\right) \\
&= f(p_1)f(p_2) \left(1 + \frac{2}{N} - \frac{(p_{T1} + p_{T2})^2}{N \langle p_T^2 \rangle} + O\left(\frac{1}{N^2}\right)\right)
\end{aligned} \tag{B.0.6}$$

and, we obtain the azimuthal correlation of momentum conservation as follows,

$$\begin{aligned}
C^\Sigma(p_1, p_2) &\equiv \frac{f_c(p_1, p_2)}{f(p_1)f(p_2)} - 1 \\
&= -\frac{2p_{T1} \cdot p_{T2}}{N \langle p_T^2 \rangle} \\
&= -\frac{2|p_{T1}||p_{T2}|\cos(\Delta\phi)}{N \langle p_T^2 \rangle}
\end{aligned} \tag{B.0.7}$$

Equation B.0.7 gives us the general two particle azimuthal correlation from the momentum conservation.

Appendix C

Correlation production from shower parton recombination model

Quark recombination by itself should not generate correlations between hadrons in final state due to the thermal nature of the participating partons. But if one of the sources of partons carries a correlation, such correlation will be carried over to the final state hadrons even when these partons recombine with other thermal partons. Figure C.1 shows the hadron production via recombination of partons from showers (dashed) and a thermal distribution(dot)(Shower partons are the originated from the jet fragmentation processes.). Jet originated correlations of the original shower partons are passed over to the hadrons of the final state. In Rudolph C. Hwa and C.B. Yang's recently developed model the correlated di-hadron production can be calculated based on an initial shower parton distribution and a thermal parton distribution.

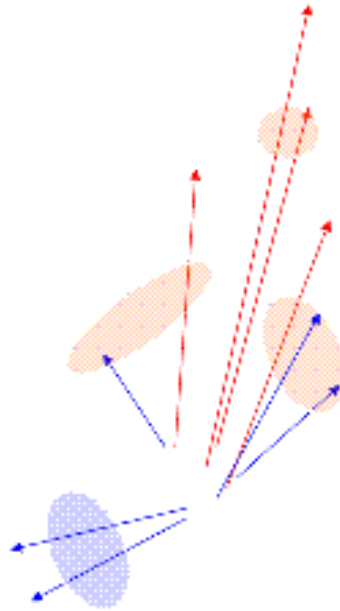


Figure C.1: Hadron produced via recombination of shower partons(red) and thermal partons(blue). Correlation of original shower partons will create the jet-like correlation between their final state hadrons

The detail of the calculation techniques are explained in detail in their papers [56][45]. Here I will give a brief introduction of their general idea. Fig C.2 shows the initial parton distribution function for shower parton(S) and thermal parton(T). The initial shower parton distribution(**SPD**) originates from a jet fragmentation processes. In general **SPD** can be represented by the following.

$$S(q) = \xi \sum_i \int dk k f_i(k) S_i^j(q_1/k) \quad (\text{C.0.1})$$

In Equation C.0.1 the shower parton distribution is represented by the convolution of the initial hard scattering parton distribution $f_i(k)$ and the flavor and momentum dependent jet fragmentation function $S_i^j(q_1/k)$. For the thermal partons a common thermal distribution is applied with parameters C and T fitted to the low p_T spectra.

$$T(q_1) = q_1 \frac{dN_q^T}{dq_1} = C q_1 \exp(-q_1/T) \quad (\text{C.0.2})$$

For single particle production such as the trigger particles, the recombination formalism to calculate the 1D transverse momentum distribution of a meson is shown here.

$$q_0 \frac{dN_M}{dp} = \int \frac{dq_1}{q_1} \frac{dq_2}{q_2} F_{qq'}(q_1, q_2) R_M(q_1, q_2, p) \quad (\text{C.0.3})$$

where $R_M(q_1, q_2, p)$ is the standard Winger function for recombination and F is the joint distribution of q and q' . We can represent the production of the trigger particles as the sum of all the possible combinations of T and S . For example for a meson trigger particle the joint distribution function can be written as:

$$F = TT + TS + SS \quad (\text{C.0.4})$$

The intermediate p_T region should be dominated by the TS and SS terms whereas the contribution of TT should negligible simply due to the limited p_T range of the

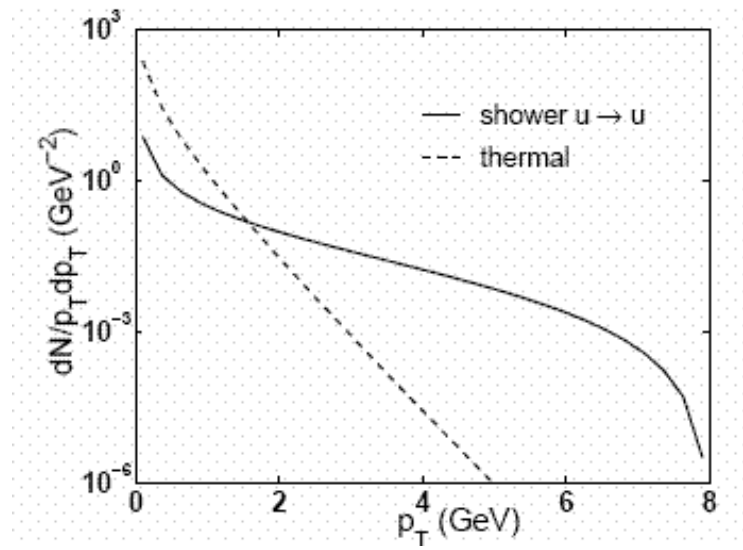


Figure C.2: Shower parton distribution of $u \rightarrow u$ and thermal parton distribution as the functions of transverse momentum in Hwa and Yang's recombination model. This distributions are used to calculation the final state correlations of the di-hadron production.

thermal distribution. For correlated two meson production, the joint distribution function F^2 of can be represented as,

$$F^2 = (TS + SS)(TS + SS) = TSTS + TSSS + SSSS \quad (\text{C.0.5})$$

In equation C.0.5 the term $SSSS$ represents the di-hadron production only from the shower parton recombination, which is related to the original fragmentation process. Other terms such as $TSTS$ and $TSSS$ all include contribution from the thermal source. In general the recombination from the thermal source provide additional energy into the jet cone compared to the pure fragmentation process in the vacuum. This feature provides an explanation for the enhanced same side yield in central AA collisions compared to pp .

Since this formalism is for meson productions(i.e. a two quark system), for baryons (i.e. a three quark system) one needs to apply the three quark joint distribution function instead. In addition, the flavor dependence should also be considered which creates more combination terms. The general algorithm can be applied to any particle species. From Equation C.0.3 one can calculate many different features of the correlation function, including the baryon and meson effect, constituent quark scaling, trigger and associated p_T dependencies etc. As we can see some of these features are related to the joint distribution function, some of them are related to the recombination function or both.

Bibliography

- [1] J. Engels. The phase transition to the quark - gluon plasma from lattice qcd. In *Penisola 1989, Proceedings, The nuclear equation of state* 17-35.
- [2] Carleton DeTar. Quark - gluon plasma in numerical simulations of lattice qcd. 1995.
- [3] Xin Nian Wang. Probe initial parton density and formation time via jet quenching. *Nucl. Phys.*, A715:775–778, 2003.
- [4] Xin Nian Wang. Effect of jet quenching on high $p(t)$ hadron spectra in high-energy nuclear collisions. *Phys. Rev.*, C58:2321, 1998.
- [5] Miklos Gyulassy and Michael Plumer. Jet quenching as a probe of dense matter. *Nucl. Phys.*, A527:641–644, 1991.
- [6] Cheuk-yin Wang. Introduction to high-energy heavy-ion collisions.
- [7] L. Frankfurt, M. Strikman, and M. Zhalov. Predictions of the generalized glauber model for the coherent rho production at rhic and the star data. *Phys. Rev.*, C67:034901, 2003.
- [8] B. R. Webber. Fragmentation and hadronization. *Int. J. Mod. Phys.*, A15S1:577–606, 2000.
- [9] John C. Collins, Davison E. Soper, and George Sterman. Factorization of hard processes in qcd. *Adv. Ser. Direct. High Energy Phys.*, 5:1–91, 1988.

- [10] G. Marchesini et al. Herwig version 5.9: A monte carlo event generator. 1996.
- [11] Xin Nian Wang. Discovery of jet quenching and beyond. *Nucl. Phys.*, A750:98–120, 2005.
- [12] Rudolph C. Hwa and Zhiguang Tan. Parton and hadron correlations in jets. 2005.
- [13] R. J. Fries, B. Muller, C. Nonaka, and S. A. Bass. Hadron production in heavy ion collisions: Fragmentation and recombination from a dense parton phase. *Phys. Rev.*, C68:044902, 2003.
- [14] C. Adler et al. Centrality dependence of high $p(t)$ hadron suppression in au + au collisions at $s(nn)^{**}(1/2) = 130$ -gev. *Phys. Rev. Lett.*, 89:202301, 2002.
- [15] Miklos Gyulassy and Michael Plumer. Jet quenching in dense matter. *Phys. Lett.*, B243:432–438, 1990.
- [16] J. Adams et al. Particle dependence of azimuthal anisotropy and nuclear modification of particle production at moderate $p(t)$ in au + au collisions at $s(nn)^{**}(1/2) = 200$ -gev. *Phys. Rev. Lett.*, 92:052302, 2004.
- [17] C. Adler et al. Disappearance of back-to-back high p_T hadron correlations in central au + au collisions at $\sqrt{S_{nn}} = 200$ gev/c. *Phys. Rev. Lett.*, 90:082302, 2003.
- [18] J. Adams et al. Evidence from $d + au$ measurements for final-state suppression of high p_T hadrons in au + au collisions at rhic. *Phys. Rev. Lett.*, 91:072304, 2003.
- [19] J. Adams et al. Azimuthal anisotropy and correlations at large transverse momenta in p + p and au + au collisions at $s(nn)^{**}(1/2) = 200$ -gev. *Phys. Rev. Lett.*, 93:252301, 2004.
- [20] K. Ackerstaff et al. Production of $k_0(s)$ and lambda in quark and gluon jets from z_0 decay. *Eur. Phys. J.*, C8:241–254, 1999.

- [21] K. H. Ackermann et al. Star detector overview. *Nucl. Instrum. Meth.*, A499:624–632, 2003.
- [22] K. Adcox et al. Phenix detector overview. *Nucl. Instrum. Meth.*, A499:469–479, 2003.
- [23] B. B. Back et al. The phobos detector at rhic. *Nucl. Instrum. Meth.*, A499:603–623, 2003.
- [24] K. H. Ackermann et al. Elliptic flow in au + au collisions at $s(n n)^{1/2} = 130$ - gev. *Phys. Rev. Lett.*, 86:402–407, 2001.
- [25] J. Adams et al. Distributions of charged hadrons associated with high transverse momentum particles in p p and au + au collisions at $s(nn)^{1/2} = 200$ -gev. 2005.
- [26] J. Adams et al. Transverse momentum correlations and minijet dissipation in au au collisions at $s(nn)^{1/2} = 130$ -gev. 2004.
- [27] S. S. Adler et al. Jet structure of baryon excess in au + au collisions at $s(nn)^{1/2} = 200$ -gev. 2004.
- [28] Nicolas Borghini, Phuong Mai Dinh, and Jean-Yves Ollitrault. Are flow measurements at sps reliable? *Phys. Rev.*, C62:034902, 2000.
- [29] M. Anderson et al. The star time projection chamber: A unique tool for studying high multiplicity events at rhic. *Nucl. Instrum. Meth.*, A499:659–678, 2003.
- [30] J. Adams et al. Identified particle distributions in p p and au + au collisions at $s^{1/2} = 200$ -gev. *Phys. Rev. Lett.*, 92:112301, 2004.
- [31] C. Adler et al. Mid-rapidity anti-proton to proton ratio from au + au collisions at $s(n n)^{1/2} = 130$ -gev. *Phys. Rev. Lett.*, 86:4778–4782, 2001.

- [32] J. Adams et al. Rapidity and centrality dependence of proton and anti- proton production from au-197 + au-197 collisions at $s(\text{nn})^{**}(1/2) = 130\text{-gev}$. *Phys. Rev.*, C70:041901, 2004.
- [33] C. Adler et al. Kaon production and kaon to pion ratio in au + au collisions at $s(\text{nn})^{**}(1/2) = 130\text{-gev}$. *Phys. Lett.*, B595:143–150, 2004.
- [34] Xin-Nian Wang and Miklos Gyulassy. Gluon shadowing and jet quenching in a + a collisions at $s^{**}(1/2) = 200\text{-gev}$. *Phys. Rev. Lett.*, 68:1480–1483, 1992.
- [35] Xin-Nian Wang and Miklos Gyulassy. Gluon shadowing and jet quenching in relativistic heavy ion collisions. *Nucl. Phys.*, A544:559–564, 1992.
- [36] J. Adams et al. Transverse momentum and collision energy dependence of high $p(t)$ hadron suppression in au + au collisions at ultrarelativistic energies. *Phys. Rev. Lett.*, 91:172302, 2003.
- [37] S. S. Adler et al. Scaling properties of proton and anti-proton production in $s(\text{nn})^{**}(1/2) = 200\text{-gev}$ au + au collisions. *Phys. Rev. Lett.*, 91:172301, 2003.
- [38] Rudolph C. Hwa and C. B. Yang. Recombination model for fragmentation: Parton shower distributions. *Phys. Rev.*, C70:024904, 2004.
- [39] Frank E. Close, Jian-wei Qiu, and R. G. Roberts. Qcd parton recombination and applications to nuclear structure functions. *Phys. Rev.*, D40:2820, 1989.
- [40] C. Adler et al. Elliptic flow from two- and four-particle correlations in au + au collisions at $s(\text{nn})^{**}(1/2) = 130\text{-gev}$. *Phys. Rev.*, C66:034904, 2002.
- [41] J. Adams et al. Azimuthal anisotropy at rhic: The first and fourth harmonics. *Phys. Rev. Lett.*, 92:062301, 2004.
- [42] A. Majumder. Dihadron fragmentation: In vacuum and in matter. 2005.

- [43] A. Majumder and Xin-Nian Wang. The dihadron fragmentation function and its evolution. *Phys. Rev.*, D70:014007, 2004.
- [44] Miklos Gyulassy, Ivan Vitev, Xin-Nian Wang, and Ben-Wei Zhang. Jet quenching and radiative energy loss in dense nuclear matter. 2003.
- [45] Rudolph C. Hwa and C. B. Yang. Dihadron correlation in jets produced in heavy-ion collisions. *Phys. Rev.*, C70:054902, 2004.
- [46] Nestor Armesto. Flow effects on jet profiles and multiplicities. 2005.
- [47] Daniel Magestro. Evidence for chemical equilibration at rhic. *J. Phys.*, G28:1745–1752, 2002.
- [48] P. Huovinen, P. F. Kolb, Ulrich W. Heinz, P. V. Ruuskanen, and S. A. Voloshin. Radial and elliptic flow at rhic: Further predictions. *Phys. Lett.*, B503:58–64, 2001.
- [49] Sergei A. Voloshin. Transverse radial expansion and directed flow. *Phys. Rev.*, C55:1630–1632, 1997.
- [50] A. K. Chaudhuri. Effect of jet quenching on the hydrodynamical evolution of qgp. 2005.
- [51] Nicolas Borghini. Multiparticle correlations from momentum conservation. *Eur. Phys. J.*, C30:381–385, 2003.
- [52] P. Braun-Munzinger, D. Magestro, K. Redlich, and J. Stachel. Hadron production in au au collisions at rhic. *Phys. Lett.*, B518:41–46, 2001.
- [53] Denes Molnar and Sergei A. Voloshin. Elliptic flow at large transverse momenta from quark coalescence. *Phys. Rev. Lett.*, 91:092301, 2003.
- [54] B. Muller, R. J. Fries, and S. A. Bass. Thermal recombination: Beyond the valence quark approximation. 2005.

- [55] K. P. Das and Rudolph C. Hwa. Quark - anti-quark recombination in the fragmentation region. *Phys. Lett.*, B68:459, 1977.
- [56] Rudolph C. Hwa and C. B. Yang. Final-state interaction as the origin of the Cronin effect. *Phys. Rev. Lett.*, 93:082302, 2004.
- [57] Z. G. Tan and C. B. Yang. Evolution of shower parton distributions in a jet from quark recombination model. 2005.
- [58] John C. Collins and Davison E. Soper. Back-to-back jets: Fourier transform from b to k- transverse. *Nucl. Phys.*, B197:446, 1982.
- [59] Yu. M. Shabelski. The role of incident parton transverse momenta in heavy quark hadroproduction. 1998.
- [60] Jiang-yong Jia. Probing jet properties via two particle correlation method. *J. Phys.*, G31:S521–S532, 2005.